

See discussions, stats, and author profiles for this publication at: <https://www.researchgate.net/publication/7172279>

# Photoemission from Liquid Aqueous Solutions

ARTICLE *in* CHEMICAL REVIEWS · MAY 2006

Impact Factor: 46.57 · DOI: 10.1021/cr040381p · Source: PubMed

---

CITATIONS

222

---

READS

47

2 AUTHORS, INCLUDING:



Manfred Faubel

Max Planck Institute for Dynamics and Self-O...

107 PUBLICATIONS 3,202 CITATIONS

SEE PROFILE

# Photoemission from Liquid Aqueous Solutions

Bernd Winter\*

Max-Born-Institut für Nichtlineare Optik und Kurzzeitspektroskopie, Max-Born-Strasse 2A, D-12489 Berlin, Germany

Manfred Faubel\*

Max-Planck-Institut für Dynamik und Selbstorganisation, Bunsenstrasse 10, D-37073 Göttingen, Germany

Received August 9, 2005

## Contents

1. Introduction	1176
1.1. Some Basic Results	1177
1.2. Purpose of This Review	1179
1.3. Historical Survey of Liquid Photoemission	1179
2. Current Knowledge of Aqueous Solutions and the Liquid–Vapor Interface	1181
2.1. Liquid Water	1181
2.2. Aqueous Salt Solutions	1183
2.3. Liquid Surface Structure, Roughness, and Adsorption Profiles	1186
3. Photoemission from Highly Volatile Liquids	1188
3.1. Principles of Photoemission	1188
3.2. Photoemission Probing Depth: Low-Energy Electron Ranges in Liquid Matter	1191
4. Liquid Water in a Vacuum: The Liquid Microjet Technique	1193
4.1. Environmental Chamber or in Situ Approach	1193
4.2. Free Vacuum Surface of Micron-Sized Water Jets	1194
4.2.1. Area-Limited Free Liquid Surface	1194
4.2.2. Local Equilibrium at the Jet Surface	1195
4.2.3. Liquid-Jet Surface Potential	1195
5. Photoemission from the Liquid Microjet with Synchrotron Radiation	1196
5.1. Liquid Water	1196
5.1.1. Reference Energy and General Considerations	1196
5.1.2. Orbital Energies and Peak Broadening	1198
5.1.3. Relative Photoionization Cross Sections	1199
5.2. Aqueous Solutions: Electron Binding Energies and Structure	1200
5.2.1. Simple Alkali Halide Salts	1200
5.2.2. Surfactants	1204
6. Concluding Remarks	1207
7. Acknowledgment	1207
8. References	1207

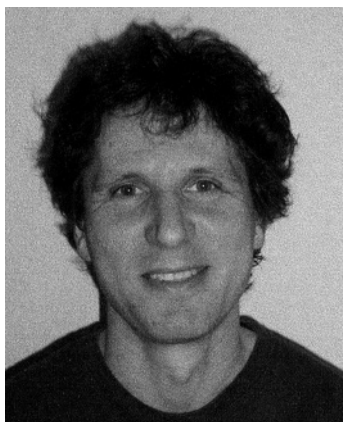
## 1. Introduction

The structure of liquid water, its role in the solvation of ionic and neutral species, and its effects on chemical reactions

have been the focus of research for over a century,<sup>1–12</sup> and yet the understanding of the structure of liquid water on the microscopic level is rudimentary. Knowledge of the molecular geometric and electronic structures of the ions and the solvent is a prerequisite to understanding the physical, chemical, and biological processes involving water. This includes the behavior of the ions both in the bulk solution and at the solution interface. Examples cover such diverse topics as the physics of confined water near biological surfaces<sup>13</sup> and chemical reactions involving halide ions at the surface of atmospheric aerosol particles.<sup>14–19,20</sup> In fact, surface solvation of halide ions by water molecules has been reported to be important in controlling the oxidant levels in the marine boundary layer of the atmosphere.<sup>17,21</sup> Moreover, the ready availability of mobile ions in the liquid is, perhaps, the most important single factor contributing to the specific and peculiar role of electrolyte liquids. Very small ion concentrations can induce major effects in electrolytes, as is exemplified by the pH value of neat water, which is induced by only one ion in  $10^8$ – $10^9$  neutral  $\text{H}_2\text{O}$  molecules.

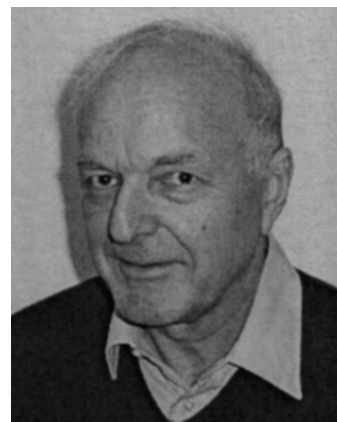
Many important questions concerning ion solvation are yet unanswered, such as: How are the ions distributed, and how do the water molecules rearrange in the solution interface? Are simple anions and cations separated at the interface? What are the conditions for the formation of an electric double layer? How are ions accommodated in the solvent network, and how long-range is their effect on the network, which relates to structure making and breaking?<sup>2,5</sup> Similarly, little is known about the change of water properties near hydrophobic surfaces, where the hydrogen bonding is considerably disrupted.<sup>13</sup> In fact, the seemingly basic question of whether simple ions—as opposed to hydrophobic interactions—can exist right at the solution surface is a current topic of intensive debate. This issue is related to the change of surface tension upon the addition of salt to liquid water, a fact reported almost 100 years ago<sup>1,22</sup> and still not yet fully understood. The reason for this lack of understanding is that such microscopic details are not contained within the classical thermodynamic description, and hence, with the arrival of modern experimental techniques and theory, the classical picture of ions being repelled from the solution surface is now being reevaluated. Recent sophisticated experiments and powerful numerical molecular dynamics simulation techniques, adapted for bulk liquids and clusters, have provided new microscopic insight into the solution interfacial structure.<sup>23–38</sup>

\* Address correspondence to either author. E-mail: bwinter@mbi-berlin.de (B.W.), mfaubel@gwdg.de (M.F.).



Bernd J. Winter was born in 1959 in Babelsberg, Germany, and grew up in West Berlin. He studied physics at the Free University Berlin and at Philipps University in Marburg. In 1985, he obtained his diploma for experimental work on optical properties of metal clusters at the Fritz Haber Institute (FHI) in Berlin under the late Prof. H. Gerischer. In the same group, he obtained his Ph.D. (Dr. rer. nat.) in 1988, with a thesis focusing on the Coulomb explosion of metal clusters. Bernd Winter spent the following two years (1989–1991) at Argonne National Laboratory (ANL) near Chicago, continuing his work with clusters, including chemical reactions and structure investigations under the direction of the late S. J. Riley. He then returned to Germany, where he spent the next three years in Garching (1991–1994) at the Max Planck Institute for Plasma Physics (IPP), joining the group of Prof. J. Küppers, where he developed an interest in the fundamental interactions of hydrocarbons adsorbed on single-crystal metals with atomic thermal hydrogen. Afterward, he returned to Berlin, where he is a staff research scientist at the Max Born Institute (MBI) for Nonlinear Optics and Short Pulse Spectroscopy, in the group of Prof. I. V. Hertel. He has been working on the combination of short pulse lasers with VUV synchrotron radiation pulses (at BESSY) for the study of dynamical processes in condensed matter. Systems have included fullerene thin films, adsorbed organic molecules (for light-emitting devices), and aqueous liquid solutions. His current research focuses on the electronic structure of the surface and bulk of liquid water; aqueous salt, acid, and base solutions; and lately biologically relevant aqueous molecules. Future developments include dynamical studies, implementing time-resolved photoemission from aqueous solutions using, for instance, femtosecond laser pulses.

How are the orbital energies of solvent water perturbed by hydrogen bonding, and what is the effect of ions on the electronic structure of water at a given concentration? Similarly, what is the electron binding energy of hydrated ions, and what is the detailed nature of the additional electronic states characteristic for the anion–solvate complex (known as charge-transfer-to-solvent, CTTS, states<sup>39,40</sup>)? Studying the dynamics of the formation of the solvated electron via these CTTS states is another area of current activity,<sup>41–46</sup> requiring the precise knowledge of the solution's electronic spectrum. It is surprising how poorly understood the electronic and structural details of the liquid aqueous surface are as compared to those of many solid surfaces. The reason behind this discrepancy might be the wealth of powerful, surface-science-dedicated techniques that cannot be readily applied to the high-vapor-pressure environment of liquids. For photoelectron spectroscopic techniques, the detection of photoemitted electrons and their kinetic energies, in a nonultrahigh-vacuum environment, is not straightforward. Furthermore, ultrahigh vacuum is a prerequisite to create clean and well-defined surfaces, and the base pressure should be on the order of  $10^{-10}$  mbar to maintain a clean surface for the period of data acquisition. At the *aqueous* interface, this requirement is obviously irrelevant; the liquid-water surface continuously fluctuates, and it is characterized by desorption and adsorption processes. This can consider-



Manfred Faubel obtained a degree in nuclear physics at the University of Mainz in 1969 and a Ph.D. (Dr. rer. nat.) at the University of Göttingen in 1976. Since 1973, he has been a research staff scientist at the former MPI für Strömungsforschung, working on crossed molecular beam scattering experiments for simple benchmark collision systems, which were also accessible for exact molecular scattering theory from first principles. These included thermal energy differential cross section measurements for vibrationally and rotationally inelastic collisions of  $\text{Li}^+\text{--H}_2$ ,  $\text{HeN}_2$ ,  $\text{He--CH}_4$ , and  $\text{Ar--O}_2$ , and the reaction  $\text{F--H}_2$ . In the 1980s, he began experiments on the exploration of the free vacuum surface of liquid water and of aqueous solutions. These had not yet been accessible for molecular beam techniques, for obvious reasons of the high vacuum pressure and an instant freezing of liquid water in a vacuum environment. It was shown that a liquid-water surface of a very fast-streaming thin liquid jet of approximately  $10\text{-}\mu\text{m}$  diameter could be sustained in high vacuum and presented a free molecular evaporation source for water vapor and for other highly volatile liquid solvents such as alcohol or acetic acid. Research on free aqueous microjet surfaces is currently continued by photoelectron spectroscopy of the molecular electronic structure of aqueous solutions with synchrotron soft X-ray radiation. In addition, vacuum microjets are exploited for laser-desorption mass spectrometry aimed at the quantitative composition of very large ions of biomolecules in aqueous solution and of the weakly bound charged peptide and protein complexes that they form in liquid aqueous solutions. Further interests are in the adaptation of short-pulse soft X-ray laser plasma sources for use in time-resolved photoelectron spectrometry of organic molecule reactions in liquid aqueous solutions.

ably complicate the interpretation of experimental data, and unless time-resolved measurements are performed, one usually obtains time-averaged information. Yet photoelectron spectroscopy, even for the study of liquids, including time-resolved pump–probe schemes, is a very versatile technique for the investigation of electronic structure. In combination with the wide tunability of polarized synchrotron radiation and with the appropriate choice of specific experimental parameters (detection angle, light polarization, photon energy, spin), photoemission (PE) can provide a wealth of microscopic information, including electron binding energies, crystal structures, surface states, adsorbate structures, and others. An important advantage of PE is its extreme surface sensitivity; for 30–100 eV photoelectrons, only the top two to three (water) layers are probed. In liquid PE, however, symmetry considerations associated with surface structural orientation play a minor role.

### 1.1. Some Basic Results

Current knowledge of the molecular structure of liquid water (and, to a lesser extent, of aqueous solutions) has been obtained by various methods, for example, X-ray<sup>47–50</sup> and neutron diffraction<sup>51–57</sup> experiments, as well as Raman and infrared (IR) spectroscopies.<sup>58–60</sup> The latter in particular consists of recent ultrafast studies of OH or OD vibrational

stretch dynamics, mostly in isotopic water mixtures.<sup>61–77</sup> Diffraction techniques can access the (averaged) local order around atoms in the liquid, even though the main objective of determining the three pair correlation functions ( $g_{OO}$ ,  $g_{OH}$ ,  $g_{HH}$ ) from the experimental diffraction patterns can be quite ambiguous. In fact, previously reported radial distribution functions differ considerably depending on the assumptions made in the analysis, such as the modifications of scattering factors. Hence, this experimental parameter, which is a crucial and desirable ingredient for simulations and theory of water, is not reliably known. However, in a recent study combining classical and ab initio simulations with better X-ray data (obtained by use of high-brilliance synchrotron radiation), many of the inconsistencies could be explained.<sup>49,50</sup> The use of computer simulation techniques to interpret neutron diffraction data for water was discussed by Soper;<sup>57</sup> more recently, he has also reported on the relative insensitivity of such diffraction methods for obtaining reliable water interaction potentials.<sup>78</sup>

Ultrafast infrared experiments that examine the OH (or OD) stretch in liquid water can be ideal for studying the hydrogen network dynamics, given that the frequency (shift) of the hydroxyl stretching vibration is sensitive to the distribution of hydrogen-bonded structures (strength, angles, and number of hydrogen bonds)<sup>65,77,79</sup> and to the intermolecular forces controlling the structural dynamics of pure liquid water<sup>65,77,79,80</sup> or of aqueous solutions.<sup>72–75</sup> In fact, various ultrafast (time-resolved) infrared methods, including vibrational echo techniques,<sup>61,62,65</sup> have been applied to extract the hydrogen-bond dynamics from the inhomogeneously broadened hydroxyl absorption. The experimental focus was primarily on the excited OH (OD) vibration population lifetime and on the spectral diffusion within the OH stretching band. Using dilute isotopic mixtures of HOD in D<sub>2</sub>O or H<sub>2</sub>O, it is possible to single out the role of the solvent effects;<sup>61–65,67–71</sup> most recently, the OH stretching vibrations could be observed also in pure H<sub>2</sub>O by infrared two-dimensional correlation spectroscopy.<sup>77</sup> In an earlier pump–probe study, the time resolution was insufficient to resolve the very fast vibrational energy-transfer component, which is much faster than in diluted D<sub>2</sub>O/H<sub>2</sub>O mixtures.<sup>81</sup> Finally, the very short lifetime of the OH *bending* vibration, measured in pure liquid H<sub>2</sub>O and in mixtures, was found to be determined by the coupling to the fluctuating hydrogen-bonded environment.<sup>76</sup>

To accurately interpret the IR spectra of a vibrational probe in different environments, various computational methods have been developed.<sup>71</sup> An important quantity in these spectroscopic calculations is the transition dipole moment of the OH or OD stretch, which strongly depends on the hydrogen-bond strength and thus on the instantaneous solvent environment. However, the interpretation of dynamics observed in IR experiments in terms of intermolecular structure is still a matter of debate.<sup>61,68,69,82</sup>

Recently, optical methods have also provided molecular-level insight into the *surface* of liquid water and aqueous solutions. Both the surface water orientation and the existence of ions in the aqueous solution interface have been inferred from vibrational sum frequency generation (VSFG) surface second-harmonic generation (SSHG).<sup>23–28</sup> The great advantage in using nonlinear optical techniques is their ultimate surface sensitivity, allowing sampling to be restricted to the surface region where isotropic symmetry is broken; in addition, these techniques can be readily performed at

ambient conditions. The first experiment to directly probe the orientation of surface water molecules was the benchmark IR–VIS SFG study on liquid water by Shen et al.<sup>83</sup> In a later X-ray absorption study,<sup>84</sup> supported by ab initio molecular dynamics simulations of the aqueous liquid–vapor interface,<sup>85</sup> the water surface structure was further detailed.

The *local electronic* structure of liquid water and aqueous solutions has been studied experimentally using near-edge X-ray absorption fine structure (NEXAFS), X-ray absorption (XAS), and X-ray emission (XES) spectroscopies and X-ray Raman scattering (XRS).<sup>84,86–92</sup> The methods are sensitive to the local water structure, such as chemical environment, bond lengths, and bond angles.<sup>93</sup> Specifically in XAS, which targets unoccupied states, the symmetry breaking resulting from electron density localization can be probed sensitively. Observed changes in the oxygen K-edge of water were thus attributed to the distortions (or breaking) of donor hydrogen bonds in liquid water (as well as in ice).<sup>86–88</sup>

Many theoretical models have been developed to describe water's properties. We can distinguish between continuum treatment and mixture (or shell) models, allowing for (clusters of) water molecules with broken hydrogen-bonding configurations. A representative selection of benchmark water models and ab initio simulation concepts can be found in a recent review on water structure.<sup>50</sup> Molecular dynamics (MD) simulations are unique techniques, in that they can provide a realistic picture of the geometric structure of liquid water. Different types of MD simulations can be categorized primarily by the interaction potentials used, ranging from force field to first-principles ab initio.<sup>94</sup> Ab initio MD simulations combine classical motion with density functional theory (DFT) computation of the electronic structure of the system at each time step. However, because of the enormous computer capacity required, their applicability limits the size and/or complexity and time scales of simulations of the systems investigated. In fact, simulations of bulk liquid water and small clusters based on first principles have provided detailed microscopic insight on hydrogen bonding. Analogous simulations for the water surface are at the limit of modern computation capacity,<sup>85</sup> because a considerable increase in the size of the simulated system is required to produce a stable interface. Recently, in just such a large-scale simulation, the existence of an acceptor-only surface species, in addition to the single donor moiety,<sup>83</sup> was identified, in agreement with XAS results.

Despite significant progress in the computation of the energies and structures of complex systems, the valence orbital structure of liquid water is not yet well described. Orbital energies in DFT generally underestimate ionization energies (which are differences between state energies),<sup>94</sup> because they are only a theoretical construct resulting from the Hartree–Fock approximation. Also, the energies strongly depend on the particular use of the exchange–correlation functional, and furthermore, the energies of DFT orbitals have a different meaning than the energies of Hartree–Fock orbitals. Experimental energies are usually in better agreement with Hartree–Fock-based methods.<sup>94</sup> Significant deficits of the currently employed DFT formalism in MD simulations employing the Carr–Parrinello technique were revealed by recent exact quantum approximations for the liquid-water potentials, using the second-order Møller–Plesset (MP2) approach as well as Hartree–Fock, extending to the second hydration shell.<sup>95</sup> In particular, the dynamics time scale for the formation and breaking of hydrogen bonds



in the DFT simulations is 1 order of magnitude slower than the experimentally observed lifetime of  $\sim 0.5$  ps.<sup>61,65</sup> In contrast, an MP2 treatment of the heterogeneous environment potential of liquid water<sup>95</sup> yields the lifetime almost correctly.

Force-field simulations are more practical and less expensive, and hence, they are more abundant when studying large complex systems, such as the interface of aqueous salt solutions. In particular, when using polarizable potentials for solvated simple ions, MD simulations have proven to be well suited for reproducing the distributions of ions near the aqueous solution interface.<sup>30–34,96</sup> MD simulations have predicted enhanced interfacial concentrations of the larger, more polarizable ions, such as iodide and bromide.<sup>30,33,96</sup> In contrast, the smaller fluoride anion is repelled from the surface. The results are consistent with asymmetric anion surface solvation inferred from some experimental cluster studies.<sup>97</sup> Clusters are considered good model systems for ion solvation,<sup>35–38,97–112</sup> yet experimental cluster studies are usually confined to containing either anions or cations at one time. Hence, certain aspects, such as double-layer formation or ion pairing, are difficult to access in cluster studies.

## 1.2. Purpose of This Review

The present review begins with an overview of previous and ongoing experimental developments in pursuit of PE spectra from highly volatile, usually nonaqueous solutions and the current understanding of liquid water and aqueous solutions on the microscopic level based on recent experimental and theoretical progress. The first aspect includes an introduction to the principles of photoelectron spectroscopy, with a focus on liquids. We then discuss the liquid microjet technique as used here and give a thorough account of the thermodynamic properties, including equilibrium considerations, of the jet surface. In reviewing photoemission, we describe the main features of the technique without giving much of the theoretical background, which can be found instead in the respective references.<sup>93,113,114</sup> The electron range is discussed in the context of the probing depth of the technique. Although the electron range in matter has been studied in great detail over the past several years,<sup>115</sup> there is still considerable controversy regarding the reliability of the experimental data, which depend sensitively on experimental conditions.<sup>116,117</sup> Especially for liquid water, no reliable data exist. The second part of the present article reviews the latest photoemission results, beginning with a summary of results for pure liquid water. The discussion focuses on gas-to-liquid peak shifts (orbital energy shifts), peak broadening, electron energy losses, and photoionization cross sections. This is followed by a presentation of photoemission results from aqueous solution systems thus far studied in our PE apparatus, using extreme ultraviolet (EUV) radiation. These are largely prototype alkali halide aqueous solutions, at salt concentrations considerably above the Debye–Hückel regime.<sup>5,7</sup> The obtained vertical ionization energies and vertical detachment energies of the aqueous ions are compared to predictions of different theoretical models, and the PE signal dependence on salt concentration is discussed in the context of the propensity for anions to exist at the surface. In addition, we present comparative PE measurements from surfactants (we have used hydrophobic tetrabutylammonium halide salts), which are useful in singling out surface vs bulk solvation.

## 1.3. Historical Survey of Liquid Photoemission

Pioneering photoemission (PE) experiments involving liquids, usually nonaqueous, were performed by K. Siegbahn and H. Siegbahn,<sup>118</sup> applying photoelectron spectroscopy for chemical analysis (ESCA; see section 3.1). These were the first experiments demonstrating the sensitivity of X-ray photoemission to the detection of intermolecular potentials and electronic reorganization in the liquid state and, in addition, showing the capability for investigating adsorption phenomena on liquid surfaces. Using Al  $K_{\alpha}$  radiation with  $h\nu = 1486.6$  keV and various experimental schemes for generating the liquid surface (see, e.g., an earlier review by Faubel<sup>119</sup>), PE spectra were obtained from pure solutions of methanol, ethanol, formamide, and glycol; from ionic electrolyte solutions, such as NaI, KI, and  $Mn(NO_3)_2$  in glycol;<sup>120</sup> and from very concentrated, 7 M, aqueous LiCl.<sup>121</sup> Under the given experimental conditions, liquids of sufficiently low vapor pressure had to be used; high-vapor-pressure liquids such as water salt brine or ethanol, which have low freezing points, were cooled to  $-40$  °C to reduce the vapor pressure below 1 mbar. These authors were the first to thoroughly introduce the concept of ESCA into the study of liquid-phase systems, including a broad discussion of various experimental aspects and a detailed consideration of the liquid-specific peak energy solvation shifts with respect to the gas phase. A detailed account of the liquid energy reference level, sample charging, and chemical shifts was presented,<sup>120</sup> and an interpretation of the measured electron binding energies of aqueous ions within a simple continuum model description was also given. In addition, the complementary character of valence and inner-shell PE, when applied to liquids, was addressed. Reference 121 focuses on the correlation of the liquid-to-vapor peak shift with molecular size and solvent polarizability. For the first time, the  $H_2O$  O1s binding energy of “liquid water” is reported (538.0 eV), obtained, however, for 7 M aqueous LiCl, as shown in Figure 1.

As a means to map ion surface concentration profiles, subsequent angle-resolved PE studies on tetra-*N*-alkylammonium halides in formamide<sup>122,123</sup> were aimed at determining the effect of the alkyl chain length and the size of the counteranion on the degree of surface segregation. In a related work by Eschen et al.<sup>124</sup> on tetrabutylammonium iodide in formamide, involving angle-resolved PE studies from a 5 mm diameter flat liquid surface, the segregated surface monolayer was found to be followed by a subsurface region where the salt was slightly depleted relative to the bulk concentration. The resulting concentration depth profile of 0.5 M tetrabutylammonium iodide (TBAI), inferred from C 1s signal evaluation, is shown in Figure 2. In another series of angle-resolved PE experiments, a number of tetrabutylammonium-based and fatty acid potassium salt surfactants, again in formamide solution, were studied, and the details of the electric double layer at the solution surface were found to depend strongly on the anion.<sup>125</sup> Beyond these two reports, we are aware of only one other group that has obtained photoemission spectra from liquid solutions. Ballard et al.<sup>126</sup> reported the HeI PE spectra of pure ethandiol and of a solution of tetrabutylammonium iodide and bromide in ethandiol. Their solutions were in the form of a liquid jet. The main conclusion from their work was that surface tension can be linked to the question of whether a given halide anion can exist at the solution surface; only if anions exist at the surface could the characteristic peaks be directly

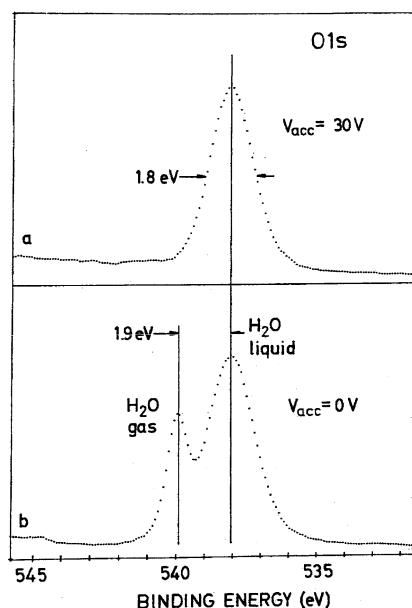


**Figure 1.** O 1s photoelectron spectra from high-concentration LiCl aqueous solution for Al  $K_{\alpha}$  excitation. Panel a was obtained by applying an electrostatic potential of 30 V over the sample compartment in order to diminish the gas-phase signal. In the absence of an acceleration voltage, the gas-phase and liquid-phase signals can be measured simultaneously; the O 1s electron binding energy in the liquid is shifted by 1.9 eV to lower energies as compared to the gas-phase value. Reprinted with permission from ref 121. Copyright 1986, Elsevier.

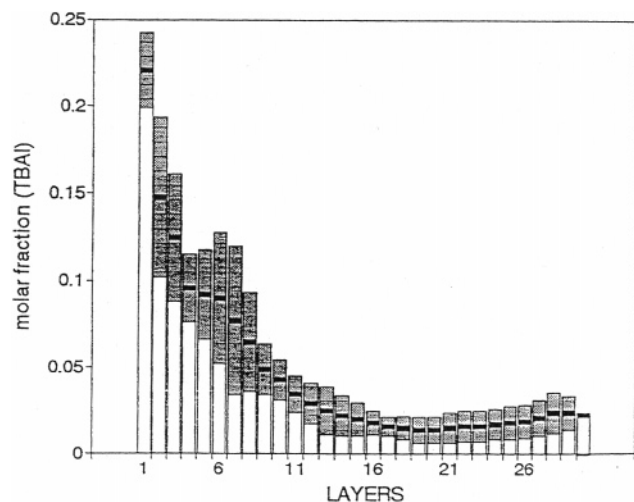


**Figure 2.** Concentration depth profile of 0.5 M tetrabutylammonium iodide (TBAI) in formamide obtained from C 1s signal evaluation in angle-resolved photoemission using synchrotron radiation. Salt concentration is expressed by the molar fraction, and the depth is given in units of layers. Each bar in the figure corresponds to a single molecular layer, which is assumed to be ca. 1.5 Å thick. Within a distance of about 12 Å from the surface, an enhanced salt concentration is observed, whereas at larger distance, between 20 and 40 Å, the salt is found to be slightly but significantly depleted relative to the bulk concentration. The shaded areas represent the standard deviation. Reprinted with permission from ref 124. Copyright 1995, American Institute of Physics.

observed in the HeI PE spectrum. Another work<sup>127</sup> discusses the relative PE signal obtained from adiponitrile, tris(dioxa-3,6-heptyl)amine, and mixtures of the two in terms of surface concentration, using Gibbs' adsorption equation.

The first extensive PE studies from liquid water and aqueous solutions were photoelectron appearance measure-

ments with tuneable vacuum UV light up to 10 eV, which, at that time, was the transmission limit of the windows used. Nearly 25 years ago, Delahay et al.<sup>128</sup> recorded the energy-integrated total electron yield (total photocurrent) from aqueous solutions, collecting photoemitted electrons with a Faraday cup placed above the liquid surface. This threshold method is useful in the determination of the highest occupied energy level, and hence, these early studies were the first to provide a spectroscopic value for the top of the conduction band of solutions of inorganic salts. Threshold energies were, in fact, reported for a large number of inorganic anions and for some cations, with ionization energies lower than that of liquid water; additionally, the value for the lowest ionization energy of liquid water, 10.06 eV, was reported for the first time<sup>128</sup> (see Figure 3). Similar threshold experiments

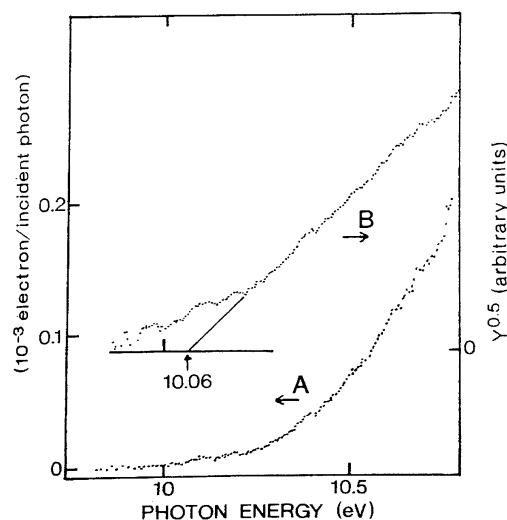


**Figure 3.** (A) Threshold photoemission spectrum of liquid water at 1.5 °C. (B) Threshold energy,  $E_t = 10.06$  eV, determined from a linear plot of the  $Y^{0.5}$  vs photon energy, where  $Y$  is the yield. Reprinted with permission from ref 128. Copyright 1981, Elsevier.

were later continued by Watanabe et al.,<sup>129</sup> then focusing on surface-active salts, e.g., tetrabutylammonium salts, in aqueous solution. The measured threshold energy for ionizing iodide in aqueous TBAI solution, shown in Figure 4, appears to depend strongly on concentration. This behavior was believed to reflect changes in the water coordination number.<sup>129</sup>

The first electron *energy-resolved* photoemission spectra of liquid water and low-concentration aqueous solutions were reported by Faubel using a novel liquid microjet technique, reviewed in ref 119. In these earlier studies, HeI radiation (21.218 eV) was used for photoexcitation, which was sufficient to quite accurately measure the  $1b_1$ ,  $3a_1$ , and  $1b_2$  valence orbital energies of liquid water, as well as the photodetachment energies of the aqueous halide anions.<sup>119</sup> In addition, valence-band PE spectra for a series of liquid alcohols, methanol, ethanol, propanol, and benzyl alcohol, with vapor pressures even higher than that of water, were reported for the first time.<sup>119,131,132</sup> Reviewed in the present article is the continuation of these studies: extending the number of aqueous systems and extending the photon energy to 120 eV using high-brilliance synchrotron radiation and having developed various technical aspects for the experiments when operated at the synchrotron beamline. The PE measurements from liquid water and from aqueous solutions reported here and in the earlier review by Faubel<sup>119</sup> are the only reported data of this type, except for the aforementioned

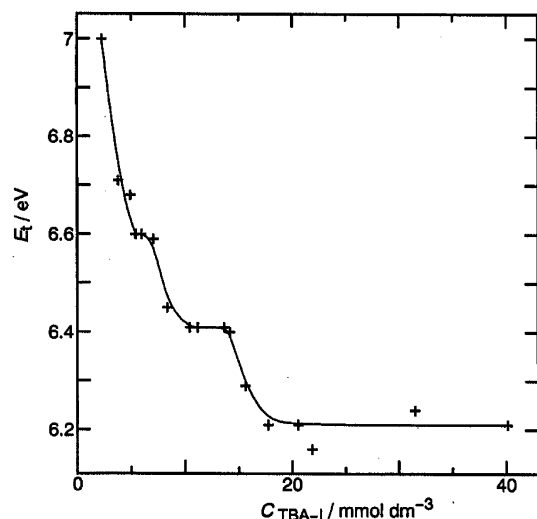


**Figure 4.** Plot of photoemission threshold energies  $E_t$  for iodide in tetrabutylammonium iodide (TBAI) aqueous solution as a function of salt concentration. The data seem to indicate dehydration of surface iodide (cf. text). Reprinted with permission from ref 129. Copyright 1998, Elsevier.

X-ray photoemission spectroscopy (XPS) study from high-concentration 7 *m* LiCl aqueous solutions<sup>121</sup> and a HeI study of the salt depletion on highly concentrated aqueous solutions of CsF.<sup>133</sup> At the time of this review, we had begun measurements of the H<sub>2</sub>O oxygen 1s spectrum from water and aqueous solutions, by extending to ~1500 eV photon energy. Liquid (time-resolved) PE studies with laser pulses, which complement transient absorption measurements on the structure and dynamics of the solvated electron,<sup>41,42,134–153</sup> have not yet been reported.

## 2. Current Knowledge of Aqueous Solutions and the Liquid–Vapor Interface

A detailed quantitative picture of the microscopic surface and bulk structure of liquid water and of aqueous solutions is about to emerge as a result of progress in theory and experiment over the past few years. Yet, this emerging microscopic picture of liquid water leaves quite some room for controversial interpretation of the new spectroscopic data.

### 2.1. Liquid Water

The importance of liquid water in almost all aspects of life, and the many peculiar anomalies of water have fascinated researchers in all fields of natural science. Despite the apparent structural simplicity of the H<sub>2</sub>O molecule, the corresponding liquid is very complex, and the amazing intermolecular hydrogen-bonding network continuously offers new and fascinating facets. This network undergoes complex structural changes on ultrafast time scales,<sup>61,65,66,76,77,81,95,145</sup> allowing for the complexity in structures and properties. The fascination with liquid water still strongly exists and has led to a number of recent reviews on the subject. Head-Gordon et al.,<sup>50</sup> for instance, reviewed the progress in structural characterization of liquid water based on scattering (diffraction) experiments and theory, including the simulation of water structure and the performance of simulations for various properties of liquid water. Their article also thoroughly accounts for early research activities on a broad range of water topics. Results of water structure from neutron diffraction (ND) and X-ray diffraction (XD) studies were

also discussed by Soper et al.,<sup>54–57</sup> Head-Gordon,<sup>47,49</sup> and Parrinello.<sup>48</sup> X-ray absorption (XAS), X-ray Raman scattering (XRS), and X-ray emission (XE) data for liquid water have been reported by Nilsson et al.,<sup>84,87,88,92,154,155</sup> Siegbahn et al.,<sup>91,156</sup> and Saykally et al.<sup>84,90,157</sup> Ultrafast (time-resolved) studies in the infrared region have been presented, for example, by Bakker et al.,<sup>66,158</sup> Elsässer et al.,<sup>62,76,77</sup> Fecko et al.,<sup>61</sup> and Skinner et al.<sup>65</sup> Recent theoretical progress in the description of water can be found, for example, in refs 61, 71, 82, and 95. Finally, in 2004, water highlights were selected for “breakthrough of the year” publications,<sup>159</sup> which emphasized the many unresolved and controversial issues. Probably the most debated issue is the recently proposed strong prevalence of water molecules with broken hydrogen bonds. Primarily on the basis of XAS studies complemented by DFT calculations, as many as 80% of water molecules in liquid water were concluded to have only two strong hydrogen bridge bonds, one donor and one acceptor.<sup>92</sup> This would suggest that liquid water is made of chains and rings<sup>92,160</sup> as opposed to the tetrahedral (ice-like) configuration commonly assumed in textbooks. The results are also inconsistent with all MD simulations.<sup>160</sup> As shown in Figure 5, the strongest experimental evidence for the conclusions drawn in ref 92 is the striking resemblance of the XA spectra for bulk liquid water and surface ice, whereas the bulk liquid spectrum is very different from the bulk ice spectrum. Most crucial in this comparison is the preedge absorption feature near 535 eV, which was assigned to water molecules with one donor hydrogen bond broken.<sup>90,92</sup> The preedge structure is present in both ice and liquid water, but it is stronger for the latter, which is indicative of the partial rupture of the hydrogen-bonding network. However, the determination of a quantitative value, to derive the actual fraction of broken hydrogen bonds, is complicated. Smith et al.<sup>161</sup> have pointed out the importance of the correct choice of an energetic hydrogen-bond criterion<sup>90</sup> and argued that the preedge intensity is very sensitive to small distortions of hydrogen bonding in the tetrahedral network. In addition, smaller changes in the preedge can be attributed to the breaking of an acceptor hydrogen bond.<sup>162</sup> Recent calculations of the complete NEXAFS data for bulk water simulated by first-principles MD have, in fact, revealed that the breaking of donor bonds increases the preedge and decreases the main-edge feature. However, a much smaller fraction, 19%, of broken hydrogen bonds was found compared to ice.<sup>162</sup>

Interestingly, the perfect tetrahedral structure model of liquid water could not quite explain such phenomena as flowing liquid water. Neutron and X-ray scattering experiments show that the rigid tetrahedral structure, as seen in ice, is partially broken for liquid water, giving rise to an open tetrahedral structure of the first coordination shell.<sup>56,92</sup> Experimental coordination numbers vary between three and four;<sup>163</sup> X-ray scattering data, e.g., give 3.7.<sup>47</sup> Simulated coordination numbers depend on the theory employed, as well as on the procedure of accounting for the average number of hydrogen bonds that are synchronously formed by any water molecule.<sup>95</sup> Local structure is directly correlated with the local charge distribution and, hence, with the interaction potentials of water. Consequently, when assuming an imbalance of charge density between oxygen and protons, as proposed from XAS studies,<sup>92</sup> simulations must use an asymmetric model for the water structure. However, to date, an asymmetric charge distribution in liquid water has not been indicated by ab initio MD simulations. Most recently,



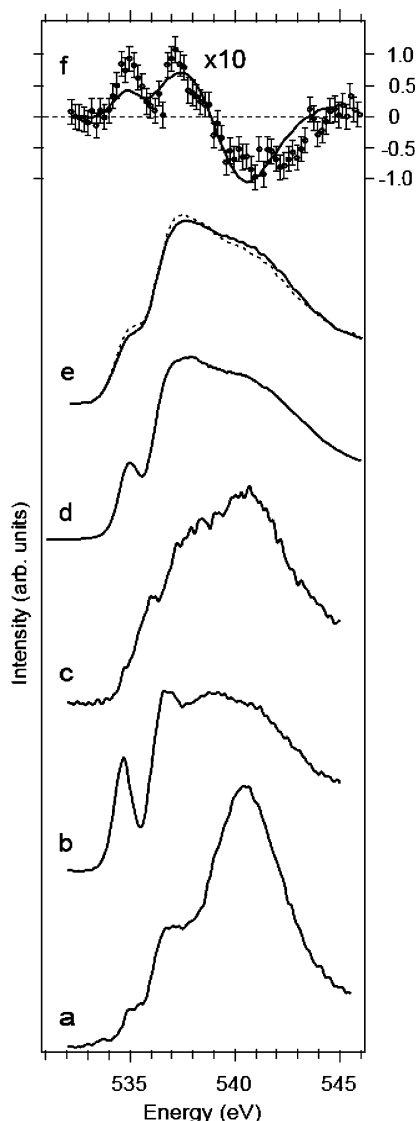


**Figure 5.** X-ray absorption spectra for water molecules in different hydrogen-bonding configurations, where ice Ih bulk and surface spectra are compared with spectra of liquid water (at two temperatures). Most importantly, the liquid-water XA spectrum (d) resembles that for surface ice (b), both exhibiting a peak in the preedge region (around 535 eV), a dominant main edge, and less intensity in the postedge region as compared to bulk ice (a). Hence, the preedge region is assigned to water molecules with a broken or distorted hydrogen bond on the donor side, whereas the postedge feature is assigned to water molecules in the tetrahedral configuration. Other spectra: (c)  $\text{NH}_3$ -terminated ice surface, (e) bulk liquid at 25 °C (solid line) and 90 °C (dashed line), (f) Difference spectra of 25 °C water minus bulk ice (solid curve) and 90 °C water minus 25 °C water (circles with error bars). Reprinted with permission from *Science* (<http://www.aaas.org>), ref 92. Copyright 2004, American Association for the Advancement of Science.

Soper<sup>78</sup> interpreted existing neutron and X-ray diffraction data using an asymmetric water potential and found that quite accurate representations of the diffraction data were possible (as is also the case for the symmetric model). The hydrogen-bond lifetime in liquid water is approximately 0.5 ps,<sup>164</sup> and the mean residence time of a water molecule in the first hydration shell is about 1.5 ps.<sup>65,74,76,95,158</sup> For a temperature rise from 10 to 90 °C the fraction of non-hydrogen-bonding hydroxyl bonds increases by a factor of 2.<sup>71,92</sup> The hydrogen-bond length, which is the result of a collective (and heterogeneous) superposition of contributions from the first

and the second coordination shell of liquid water,<sup>95</sup> is reported to range between 1.8 and 1.9 Å,<sup>53,92,95,165</sup> and again, the value is strongly model-dependent.<sup>95</sup>

The water network dynamics at shorter times, involving ultrafast intermolecular vibrational energy transfer (over many water molecules) and relaxation, has been most directly probed by the infrared spectrum of the OH stretching and bending vibrations at various  $\text{H}_2\text{O}/\text{D}_2\text{O}$  ratios in liquid water. Using nonlinear-infrared spectroscopy, as outlined above, different stretch vibrational relaxation times, of 0.7–1.0 and 2 ps, respectively, were observed for OH<sup>68,81,166</sup> and OD.<sup>65</sup> Measurements of the frequency fluctuations in the hydroxyl stretch,<sup>61</sup> on the <200 fs time scale, were assigned to the underdamped displacement of the hydrogen-bond coordinate. The dynamics at the longer time scale of 0.7–1.2 ps correlates with the collective structural reorganization<sup>61</sup> involved in the breaking and making of hydrogen bonds. In a MD study of the hydrogen-bond dynamics,<sup>82</sup> this longer-time response was concluded to be due to thermal motion<sup>82</sup> rather than IR-induced vibrational predissociation.<sup>167</sup> Under fully resonant conditions, for the dynamics of the OH stretch in pure liquid  $\text{H}_2\text{O}$ , energy redistribution within the hydrogen-bonding network is even faster. Liquid water loses the memory of persistent correlations in its structure in only 50 fs.<sup>77</sup> The lifetime of the OH *bending* vibration is 170 fs in pure  $\text{H}_2\text{O}$ ,<sup>76</sup> which is about a factor of 2 shorter than for  $\text{H}_2\text{O}$  diluted in  $\text{D}_2\text{O}$ . This lifetime is determined by couplings to the fluctuating liquid environment, likely involving librations.<sup>76</sup>

There is also supportive evidence for the existence of distinct water species from femtosecond IR pump–probe experiments.<sup>64</sup> The slow and fast components of the orientational relaxation of HDO molecules in liquid water were assigned to strongly and weakly hydrogen-bonded water molecules, respectively. In a similar study,<sup>63</sup> three dominant water species were identified by their rotational time constants. This interpretation has been questioned, however, because strong negative feedback (thermal) effects in the hydroxyl OH stretch vibration excitation in liquid water tend to increase the observed relaxation times by as much as a factor of 4, from 0.3 to 1.1 ps.<sup>61,66</sup> Interestingly, the existence of distinct water species in liquid water was already considered more than 100 years ago by Röntgen.<sup>168</sup> In his work “On the Constitution of Liquid Water”, with a focus on water’s anomalies, two different water species were postulated, one being ice-like and another not specified.

The *surface* of liquid water contains a considerable amount (probably about 20%) of water molecules with one free OH bond (non-hydrogen-bonded) pointing out of the liquid, and the other, hydrogen-bonding OH pointing into the bulk liquid.<sup>83</sup> In this configuration, initially inferred from surface sum frequency generation (SFG) studies, the permanent water dipoles are nearly in the surface plane, consistent with the very small surface potential of water.<sup>169</sup> More recent XAS studies<sup>84</sup> have indicated the existence of another surface water species, the acceptor-only configuration, in which both OH bonds of the water molecule are directed toward the vacuum. This conclusion was based on the change of the O 1s preedge structure in a comparison of the surfaces of ice and liquid water.<sup>84</sup> The results are in agreement with *ab initio* MD studies by Kuo and Mundy.<sup>85</sup>

Judging from the above discussion, there remains an obvious need for new experiments and more advanced theory. To the experimental end, photoemission studies,



which are the topic of this article, are expected to shed light on many of the above questions. So far, the use of PE spectroscopy for studying the structure of liquid water has been barely mentioned, despite the fact that PE can provide complementary information when compared to related techniques, such as XAS or XES. A particularly advantageous feature of PE is the variable probing depth. For instance, when combining the probing depth variation with the local bonding information accessible by inner-shell PE, it would seem feasible to measure the H<sub>2</sub>O oxygen 1s orbital energy for a specific local environment (e.g., surface water, bulk water, or water in a solvation shell). However, all of the presently available PE data have been obtained for photon energies lower than 120 eV, too low to address such an issue.

## 2.2. Aqueous Salt Solutions

A currently debated aspect of aqueous solutions is the distribution of ions in the near-surface region. Whether simple ions can exist right at the solution surface is important for the physics and chemistry of electrolytes and has recently been realized to also be crucial for the surface chemistry at the solution liquid–vapor interfaces. For example, halide ions at the surface of atmospheric aerosol particles can control oxidant levels in the marine boundary layer of the atmosphere, and they play a crucial role in the chemistry of ocean surfaces.<sup>14–17,20,21,170</sup> For instance, the reactive uptake of Cl<sub>2</sub>(g) and Br<sub>2</sub>(g) by aqueous halide solutions, studied in the context of chlorine and bromine in the stratospheric ozone destruction process, has revealed the importance of gas–liquid interface chemical reactions.<sup>19</sup> Hence, the solution interface was realized to serve as a, previously unknown, halogen source that can help to improve modeling of the global halogen cycle. This new insight from the atmospheric community has challenged the commonly accepted thermodynamic description of ions (anions and cations) as being entirely repelled from the solution surface by dielectric electrostatic image forces. Early theoretical treatments by Onsager and Samaras,<sup>1</sup> largely developed to explain the experimental change of surface tension upon the addition of salt, did not require microscopic details. Although the initial Onsager model for electrolyte solutions and subsequent modifications taking into account specific ion–solvent interactions are incapable of correctly reproducing experimental surface tension measurements, the concept of an ion-depleted surface layer has still become the standard textbook picture.<sup>7,171</sup> More recent state-of-the-art continuum models, as well as earlier MD simulations, could, in fact, predict ion adsorption at the solution surface for some specific cases.<sup>172</sup> The newly emerging theoretical picture of the aqueous solution interface is based on molecular dynamics simulations that explicitly incorporate water–ion interactions and surface structure.<sup>17,30–34,173–183</sup> These simulations are very sensitive to the potentials employed; when polarizable potentials are used, larger and more polarizable anions, such as iodide and bromide, are found to be enhanced at the surface. Snapshots from such MD simulations of sodium halide solutions are shown in Figure 6 (from ref 30). The larger, more polarizable halide anions are present at the surface, and iodide and bromide even have higher concentrations in the interfacial region than in the bulk. The smaller nonpolarizable fluoride is repelled from the surface. Notice that such differential segregation implies the formation of an electric double layer, separating the anions and cations by ca. 3 Å. This distance is about the Debye length expected from Gouy–Chapman

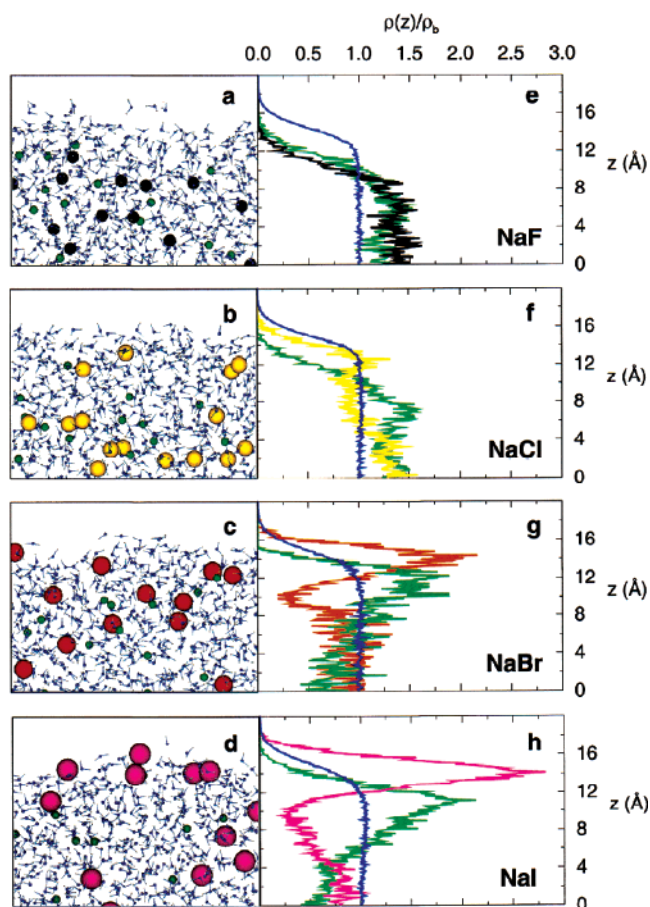


**Figure 6.** (Left) Snapshots from molecular dynamics simulations showing the interfacial distribution of sodium cations and halide anions for the alkali halide aqueous solutions. (Right) Plot of the respective number densities  $\rho(z)$  of water oxygen atoms and ions vs distance  $z$  from the center of the slabs in the direction normal to the interface, normalized by the bulk water density,  $\rho_b$ . The colors of the curves correspond to the coloring of the atoms in the snapshots. Important to notice is that the small sodium cations are always depleted from the surface, as is also true for the small fluoride anions. However, for increasing anion size and hence polarizability, the propensity of anions to exist at the solution surface increases. For NaI solution, the two ion distributions are separated by ca. 3 Å. Reprinted with permission from ref 30. Copyright 2001, American Chemical Society.

theory, detailed in section 2.3. Finally, these MD simulations, using polarizable potentials, appear to be consistent with the observed changes in surface tension as a function of salt concentration. Note that the existence of surface ions would not necessarily contradict the classical Onsager-type theory as long as the subsurface region were sufficiently depleted of ions, so that the net effect would still be that of a lower ion concentration in the overall interfacial region. This new picture is now subject to experimental verification, having spawned a series of sophisticated investigations that provide the necessary surface sensitivity and that can be readily performed at high vapor pressure. Nonlinear optical methods, such as vibrational sum frequency generation (VSFG) and second-harmonic generation (SHG), with their ultimate surface sensitivity, are thus ideal techniques for this purpose. Complementary PE spectroscopic techniques are usually more difficult to apply, as they require the coupling of high vapor pressure and ultrahigh vacuum.

VSFS<sup>24,26</sup> studies of aqueous salt solutions (NaF, NaCl, NaBr, NaI), using isotopic mixtures of water, were the first to reveal the presence of anions in the interfacial region. Sum

frequency spectra of NaF, NaCl, NaBr, and NaI, with neat water spectra overlaid, from Raymond et al.<sup>26</sup> are shown in Figure 7. Most noticeable are the changes in the  $\sim 3200$  and

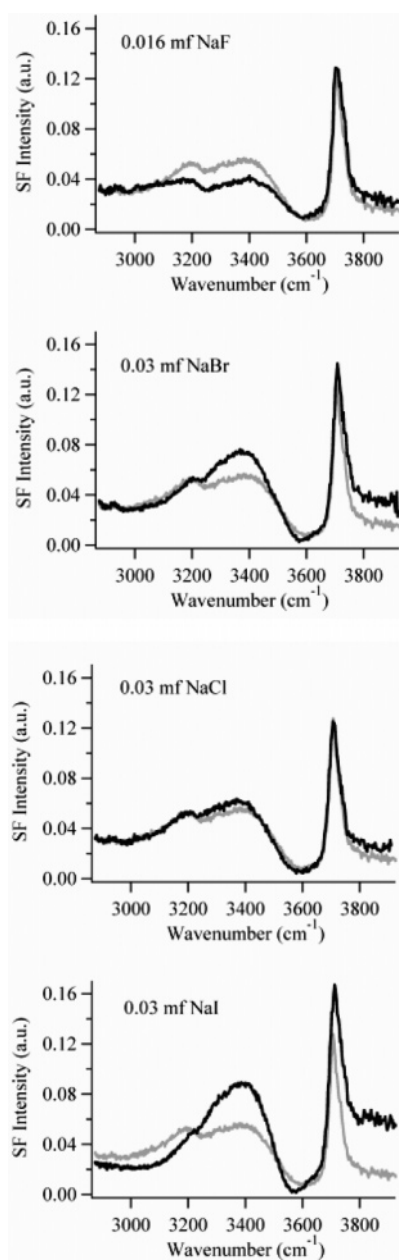


**Figure 7.** Vibrational sum frequency spectra of NaF, NaCl, NaBr, and NaI aqueous solutions; concentrations in mf (molar fraction) are indicated. The neat water spectrum (gray) is shown for comparison in each panel. Peaks at  $3705$  and  $3454\text{ cm}^{-1}$  are assigned to the free and donor OH vibrations, respectively. Peaks at  $\sim 3200$  and  $3325\text{ cm}^{-1}$  are assigned to vibrations of tetrahedrally coordinated interfacial water. Reprinted with permission from ref 26. Copyright 2004, American Chemical Society.

$3325\text{ cm}^{-1}$  regions, which can be assigned to vibrations of the tetrahedrally coordinated interfacial water molecules. The intensity decrease in this region for NaF solution, and the increase for the other solutions have been attributed to the enhancement and weakening of the water bonding network in the surface region, respectively.<sup>26</sup> Unlike the tetrahedrally coordinated features, the uncoupled free OH residing in the top surface layer does not exhibit significant spectral changes of any of the salt solutions. This minimal perturbation of water molecules in the topmost layer thus suggests a

significantly diminished population of anions at the uppermost layer of the surface, but not at enhanced concentration. This does not necessarily imply that there is a top surface layer of pure water, but only that the surface concentration of ions is small enough not to have any significant effect on the bonding character.<sup>26</sup> In a similar VSFS experiment, combined with Raman and infrared spectroscopy measurements, the interfacial hydrogen-bonding network of aqueous solutions of halide salts<sup>25</sup> was observed to be distorted, but only for bromide and iodide, not for fluoride and chloride. Furthermore, the interfacial depth, contributing to the VSFS signal, was observed to increase in NaBr and NaI aqueous solutions with respect to that of pure liquid water. The larger interfacial depth is consistent with the MD simulations in Figure 6, showing that bromide and iodide segregate near the surface with a subsequent enhancement of sodium below the anion top surface layer. More certain confirmation of the enhancement of anion concentration was provided in a subsequent resonance-enhanced SHG experiment from alkali iodide aqueous solutions in the  $1\text{ mM}$  concentration range.<sup>27</sup> The experimental surface concentration, inferred from the measured SHG signal, can be well fitted to Langmuir adsorption isotherms (eq 2.7 with eq 2.8 in section 2.3), despite the crude assumptions made in this model. Results for low-concentration NaI solutions, using different laser wavelengths of  $425\text{--}550\text{ nm}$ , are shown in Figure 8. The large negative

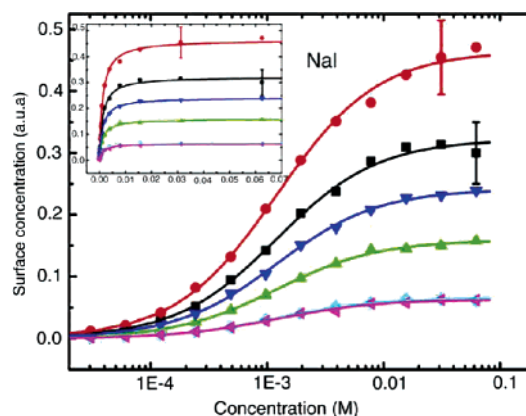


**Figure 8.** Iodide surface concentration (main figure), as determined from second-harmonic signal (inset), of dilute NaI aqueous solutions at different bulk concentrations, measured at several laser wavelengths in the range  $425\text{--}550\text{ nm}$ . The curves result from a simultaneous fit to the SHG response of a constant water background and an iodide response that follow the Langmuir adsorption isotherm. The fits result in a Gibbs excess free energy of adsorption of  $6.1 \pm 0.2\text{ kcal/mol}$ . Reprinted with permission from ref 27. Copyright 2004, Elsevier.

value for the surface excess free energy,  $-6.1\text{ eV}$ , obtained from the fit is supportive of the formation of an anion surface monolayer. In a subsequent work investigating aqueous solutions of NaSCN,<sup>34</sup> the experimental SHG data for aqueous  $\text{SCN}^-$  were presented together with a simulated interfacial density profile of the ions. This profile cannot be extracted from the experiment, even though exactly the interface is being probed. Only a minimum of the Gibbs free energy within the interfacial region can be established, because the SHG signal is a (weighted) average over the entire range of broken symmetry. Consequently, in addition to the problems that can arise from the simplified assumptions contained in the Langmuir model, the analysis is meaningful only to the point that this weight factor can be

reproduced. The issue is further discussed in section 5.2.1, where the SHG and PES results are compared. In contrast to the SHG case, PES tends to probe a larger interfacial region, and hence the PE signal, in the case of NaI aqueous solution, is more difficult to evaluate quantitatively.

Probably the clearest confirmation of the existence of ions at the solution surface comes from a very recent PE study of *saturated* KBr and KI aqueous solutions performed in a high-pressure spectroscopy vacuum system.<sup>29</sup> Starting from a well-defined alkali halide single-crystal sample, PE spectra were then measured while the water vapor pressure was increased (function of humidity) until the solid surface had liquefied. Under the experimental conditions, the sample is at rest, and the role of radiation-induced effects is not very clear. A key feature in this experiment, which uses synchrotron radiation, is the appropriate choice of photon energies such that the photoelectrons emerging from an element-specific energy level would all have the same kinetic energy, hence allowing for identical probing depths. This enables the determination of relative atomic concentrations, because each ion species can be detected with the same probability, provided that the photoionization cross sections in aqueous solution were known. From the increase of the cation-to-anion ratio at the deliquescence point, shown in Figure 9, it

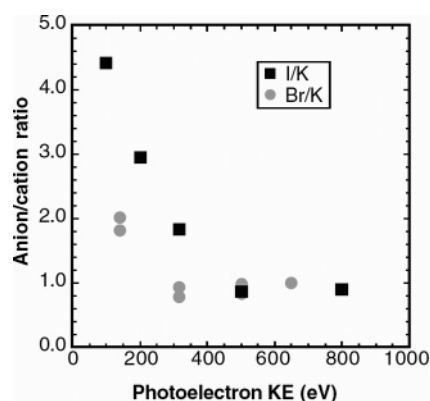


**Figure 9.** Plot of the measured anion-to-cation photoemission signal ratio as a function of the electron kinetic energy for saturated KI and KBr aqueous solutions. The larger ratio for the smaller probing depth at lower kinetic energies confirms the enhanced anion concentration at the solution interface. The leveling at ratio 1 near 500 eV might suggest that equal amounts of anions and cations are probed at sufficiently large distances from the surface. According to Figure 14, the probing depth at 500 eV is likely to be between 20 and 30 Å, at which point the technique should be considerably bulk sensitive (compare also Figure 6). Reprinted with permission from *Science* (<http://www.aaas.org>), ref 29. Copyright 2005, American Association for the Advancement of Science.

was concluded that the enhancement of the anion concentration at the solution interface is even larger than predicted by MD simulations. Assigning reliable values to this behavior is complicated, however, because the electron probing depth is not precisely known, and instead, theoretical density profiles must be used. Electron binding energy shifts that can exist between surface and bulk solvated ions were not observed in this study of saturated salt solutions, despite the considerable variation of probing range.

The geometric structure of the ion solvation shell as well as the solvation energy, associated with the electronic polarization and the rearrangement of water molecules about a charge, are often described thermodynamically in terms of the change of the Gibbs free energy. In the frequently used dielectric cavity model, an assumption on the radius of

the charge cavity is required; the meaning of such a radius is not well defined, however. Also, the distance at which a charge can affect the water structure,<sup>75,185–188</sup> in textbooks known as the structure-making or -breaking effect,<sup>2,5,185,188,189</sup> is not fully understood. It has been commonly assumed that certain ions either enhance or weaken the water network structure. This macroscopic picture has recently been challenged, though, by Bakker et al.,<sup>74,75</sup> who studied the dynamics of water molecules in solvation shells in IR vibrational femtosecond pump–probe experiments. Using aqueous salt solutions of H<sub>2</sub>O/HDO mixtures, it was possible to selectively measure the response of solvating water given that OH vibrational lifetimes are much longer for HDO molecules in the first solvation shell. Then, in measuring the orientational correlation time of water molecules, the hydrogen-bond structure was found to be negligibly affected by the presence of ions. This has consequences for the mechanism responsible for viscosity changes in aqueous salt solutions, which apparently is not caused by the hydrogen-bond structure but rather by the rigid solvation shell, making the ion appear larger.<sup>75</sup>

Classical Raman and IR spectroscopy<sup>59</sup> has revealed that the hydrated electrolyte effectively perturbs the structure of the bulk water in aqueous solution.<sup>58</sup> This perturbation was argued to be consistent with an apparent density change of water in solution associated with an increase in the hydrogen-bond strength of the bulk water. The determined structural picture is that of ions isolated as clusters of hydrated ion pairs, segregated in water. Hence, two principal water species were inferred, consistent with the existence of separate water and hydrated electrolyte subphases in solution.<sup>58,60</sup> Coordination shell numbers were typically obtained from X-ray and neutron diffraction.<sup>51,54,55,190–193</sup> Also, neutron scattering data from concentrated HCl in H/D-substituted water have revealed information on the perturbing effect of solvated ions in the characteristic water structure (which is usually assumed to be tetrahedral). In ref 52, the ion-induced change of the water structure, at high concentration, was found to be strongly correlated with the effect of applying high pressures. In fact, ionic concentrations of a few moles per liter have equivalent pressures that can exceed 100 atm. The actual degree of water disorder in aqueous salt solution, as indicated by the water–water radial distribution function, strongly depends on the pair of ions involved.<sup>52</sup> In general, though, quantitative interpretation of diffraction patterns in terms of real-space microscopic structure very much depends on the potential used in the simulations.<sup>54</sup> This aspect, which is intrinsic to any analysis of diffraction patterns from solutions, has been discussed in detail by Head-Gordon et al.<sup>50</sup>

Studies of the *electronic* structure of aqueous solutions by electron spectroscopic techniques are scarce because of the high-vapor-pressure environment. This explains why previous experiments were largely absorption measurements (see below) and why photoemission measurements other than those presented here are absent. Only two reports exist on the valence orbital energy changes associated with ion solvation. Both are X-ray absorption studies (XAS; see section 3.1), combined with density functional theory,<sup>89,194</sup> which are sensitive to the local electronic structure of water. Similarly to PE, the late start of liquid XAS is again because of the requirement of a vacuum environment when using electron detection. In ref 89, the chemical bonding of water in the first hydration shell to transition-metal ions was studied by oxygen 1s XAS. Features in the oxygen preedge region



in  $\text{Cr}^{3+}$  and  $\text{Fe}^{3+}$  in aqueous solutions were interpreted in terms of orbital mixing between water and the transition-metal ions. Reference 194 reports on the changes in the oxygen K-edge X-ray absorption spectrum when sodium halide salt is added to liquid water (up to 4 M). Again, supported by DFT calculations, the observed changes in the pre- and postedges were assigned to a significant perturbation of unoccupied molecular orbitals of water molecules in contact with an anion. No distortion beyond the first solvation shell was observed, in agreement with the above IR vibrational experiments. Quantitatively, the XA spectral changes were assigned to a red shift of the XA transitions.<sup>194</sup>

A special electronic structural feature arising from the water–ion interaction is the unique effect of solvent water in stabilizing additional electronic states characteristic of the anion–solvate complex (known as charge-transfer-to-solvent states CTTS<sup>39,40</sup>). This is currently a very active field of research,<sup>41–46,136</sup> including chemical reactions with multisolvated electrons at intense laser irradiation.<sup>195</sup> Even though the phenomenology of the CTTS process and its relationship to the production of solvated equilibrated electrons ( $e_{\text{eq}}^-$ )<sup>41,174,196</sup> has been known for some time, the general assignment of energies for CTTS transitions over the broad class of aqueous anions is not well established. Furthermore, past workers have speculated that there are Rydberg-like series of such CTTS states; however, these higher CTTS bands overlap the liquid conduction band. Consequently, an area of current activity is to map out the formation of  $e_{\text{eq}}^-$  via these direct (conduction-band) and indirect (CTTS) pathways.<sup>44,197,198</sup> Experimentally, this has usually been studied by pump–probe transient absorption, using ultrashort laser pulses. To distinguish between the two processes, it would be of great value to accurately determine the energetic position of the conduction band with respect to the ions in aqueous solution.<sup>199</sup> This is equivalent to measuring the valence photoemission spectrum, providing the *full* distribution of vertical detachment energies resulting from different (anion) solvation configurations. The importance of the solvated electron extends well beyond the aspects mentioned. In fact, the crucial role of aqueous electrons in driving chemical radical reactions in aqueous systems (often in biological systems) has recently been reviewed in great detail in the context of present and future energy technologies.<sup>200</sup> Recent and earlier discussions on the dynamics of excess electrons in water, and on the structure of the solvated electron, can be found in refs 63, 140–145, 149–153, 201, and 202. A quantity related to the valence-band structure of bulk aqueous solution is the ionization potential (IP) of an ion solvated by a well-defined number of water molecules, as measured for gas-phase clusters.<sup>35,36,97–111</sup> Clusters, in addition, have served as invaluable model systems in the investigation of the nature and dynamics of the solvated electron.<sup>134,135</sup> Experimental and theoretical cluster studies have focused on elucidating IPs, as well as structural features and energetics, related to the sequential solvation of ions by a well-defined number of water molecules. This particularly touches upon surface vs bulk solvation in water clusters, e.g.,  $\text{I}^-(\text{H}_2\text{O})_n$ .<sup>97</sup> Surface solvation in water clusters has also been the focus for complex anions such as benzene dicarboxylate dianions<sup>111</sup> or the doubly charged sulfate ( $\text{SO}_4^{2-}$ ) and oxalate ( $\text{C}_2\text{O}_4^{2-}$ ) hydrated anions.<sup>36,108,110</sup> Oxalate, for example, is an important inorganic dianion commonly found in solutions and solids; the carboxylate functional group ( $-\text{COO}^-$ ) is ubiquitous in biological systems, in many technological

important materials, and in polluted atmospheres. Cluster experiments have also served as an important tool for calibrating and verifying the applied computational approaches. Whether the ionization energies of the larger clusters and that of the bulk solution<sup>199</sup> can be directly compared is debatable for the following reasons. First, the convergence to bulk values is relatively slow because of long-range solvent polarization effects; typically, inclusion of more than 100 water molecules is necessary to reach the onset of bulk behavior.<sup>174</sup> Second, the population of solvation sites of the ions (interior vs surface) can change upon moving from clusters to extended systems, albeit with only a minor effect on ionization energies. Third, the typically considered rigid, low-temperature structure of water clusters differs significantly from that of a solution at ambient conditions.

### 2.3. Liquid Surface Structure, Roughness, and Adsorption Profiles

Properties of liquid surfaces can differ considerably from the better known surfaces of solid states.<sup>203,204</sup> Many differences arise as a consequence of the significantly greater mobility of liquid molecules, leading to the loss of the periodic crystalline features. Greater mobility also gives rise to an increased surface roughness of liquids and to a rapid thermodynamic equilibration of concentration distributions of different surface-adsorbed molecular species by diffusion between the surface and the bulk liquid.

The structure of liquid surfaces thus appears disordered in comparison with solid-state crystal surfaces. In X-ray or neutron scattering experiments from liquids, the prominent crystal diffraction interference peaks at specified Bragg angles appear reduced compared to much weaker averaged-out diffraction patterns. The scattering intensity is proportional to the structure factor  $S(k)$ , which is related in a simple way to the Fourier transform of reduced configurational distribution functions (RDFs). In the simplest form, in the spherical wave first Born approximation, the radial distribution function  $g(r)$  for the probability of finding atom pairs at the distance  $r$ , is related to the structure factor by

$$S(k) - 1 = (4\pi/k) \int dr \sin(kr) r g(r) \quad (2.1)$$

Here, the momentum transfer  $k = (4\pi/\lambda_{\text{in}}) \sin(\theta/2)$  is determined by the scattering angle  $\theta$ , and  $\lambda$  is the incident wavelength.<sup>205,206</sup> Surface density distribution functions are measured in X-ray diffraction (elastic and inelastic) and electron diffraction interference experiments, such as surface extended X-ray absorption fine structure (EXAFS) spectroscopy, whereas neutron diffraction techniques seem to remain reserved for the study of bulk solutions. For liquid water, one obtains radial distribution functions of the (averaged) intermolecular distances O–O and of the hydrogen positions. RDFs can also be directly linked to numerical simulations, and RDFs are thus important ingredients when testing theory. For more detailed discussions of structural information on liquid water inferred from scattering techniques, refer to section 2.1. The importance of scattering techniques in accessing the structure of aqueous solutions was addressed in section 2.2.

The surface motion of soft liquids and the geometrical shape of the liquid–surface interface are primarily controlled by surface tensions. The microscopic surface structure of liquids at rest is very smooth, but it is roughened by thermally excited capillary waves, which is the liquid correspondence

to solid-state transverse surface phonons. Surface capillary waves travel with a phase velocity on the order of  $10 \text{ ms}^{-1}$  for molecular liquids such as water.<sup>207,208</sup> If  $z(r)$  is the component of the interface displacement in the normal direction at a lateral position  $r$ , then the average quantity<sup>209</sup>

$$\sigma^2 = \langle [z(r) - z(0)]^2 \rangle \quad (2.2)$$

defines the surface roughness  $\sigma$ . In the theory of thermal capillary waves, the surface roughness is related to the surface tension by

$$\sigma_c \sim (k_B T / \gamma)^{1/2} \quad (2.3)$$

where  $\gamma$  is the surface tension and  $T$  is the surface temperature. The interfacial width has been represented as a combination of an intrinsic profile width  $\sigma_o$ , given by the molecular structure, and the capillary wave contribution  $\sigma_c$ . The intrinsic surface roughness  $\sigma_o$  is on the order of  $1 \text{ \AA}$  or smaller. For the capillary-wave-induced surface roughness, a value of  $3 \text{ \AA}$  was determined for liquid water at  $298 \text{ }^\circ\text{C}$  by grazing-incidence X-ray scattering spectrometry from liquid surfaces.<sup>210,211</sup> Similar measurements for nonaqueous liquids yield for the surface roughness of ethanol  $\sigma_c = 6.9 \text{ \AA}$ .<sup>209</sup> The experimentally determined roughness for liquid metals is  $\sigma_c = 1 \text{ \AA}$  for Hg.<sup>212</sup> The temperature dependence has been studied for liquid gallium samples, with a roughness value of  $\sigma_c = 0.80 \text{ \AA}$  at  $T = 30 \text{ }^\circ\text{C}$ , rising to  $\sigma_c = 0.93$  at  $T = 170 \text{ }^\circ\text{C}$ .<sup>213</sup> For liquid potassium, the capillary wave roughness is  $\sigma_c = 2$ ;<sup>212,214</sup> see Table 1. The surface roughness values for

**Table 1. Experimental Surface Roughness vs Thermal-Capillary-Wave Theory Results for Selected Liquids<sup>a</sup>**

liquid	surface tension $\gamma^a$ (mN m <sup>-1</sup> )	$(k_B T / \gamma)^{1/2}$ ( $\text{\AA}$ )	exptl surface roughness $\sigma_c$
Hg	485	0.9	1 <sup>b</sup>
Ga	750	0.75	0.80 <sup>c,d</sup> /0.95 <sup>c,e</sup>
K	~100	2.0	2 <sup>f</sup>
H <sub>2</sub> O	73	2.4	3 <sup>g-i</sup>
ethanol	23	4.2	6.9 <sup>j</sup>

<sup>a</sup> From ref 216. <sup>b</sup> From ref 212. <sup>c</sup> From ref 213. <sup>d</sup>  $T = 30 \text{ }^\circ\text{C}$ . <sup>e</sup>  $T = 170 \text{ }^\circ\text{C}$ . <sup>f</sup> From ref 214. <sup>g</sup> From ref 210. <sup>h</sup> From ref 211. <sup>i</sup> From ref 218. <sup>j</sup> From ref 209.

the molecular liquids are almost one order of magnitude larger than the roughness of the investigated liquid metal surfaces because of the significantly higher surface tension of metals. Only for potassium, which has an unusually small liquid metal surface tension of  $0.1 \text{ Nm}^{-1}$ , is the surface roughness in the  $2 \text{ \AA}$  range and, thus, comparable to that of water. Also in agreement with the capillary wave theory, the roughness of liquid surfaces increases with rising surface temperature and simultaneously decreasing surface tension. This is illustrated for gallium measurements at two different probe temperatures in Table 1. Supercooled water ( $\gamma = 77 \text{ mN/m}$  at  $-8 \text{ }^\circ\text{C}$ )<sup>215,216</sup> and “hard water” with a high salt content, therefore, have smoother surfaces. Water at more elevated temperatures becomes rougher because the surface tension is reduced to  $\gamma = 59 \text{ mN/m}$  at  $100 \text{ }^\circ\text{C}$  and eventually approaches the value  $\gamma = 0$  at the critical point.

In liquid metals, surface-induced layering has been observed (Hg, Ga, In, K) in the first two or three subsurface layers. Layering is not present in water or in ethanol.<sup>217</sup> Only recently, at very short length scales, have deviations from the macroscopic capillary-wave theory of liquid interfaces

been reported.<sup>218</sup> Near the wavelength limit set by intermolecular distance, the simple macroscopic capillarity wave theory was observed to fail for liquid-water surfaces. According to this study, the apparent short-distance surface tension at very high wavenumbers,  $\lambda_c \leq 3 \text{ \AA}$ , decreases from its bulk value by as much as a factor of 5, indicating that, at very short capillary wavelengths, the surface roughness is increasing. Tentatively, this result is attributed to a conjectured decrease of the molecular cohesion potential in angstrom-scale surface protrusions with high surface curvature.<sup>218</sup>

In addition, liquid surfaces differ appreciably from solids by the rapid exchange of surface molecules with molecules in the bulk liquid by diffusion processes. Furthermore, because of the high vapor pressure of water solutions, a rapid exchange of molecules also takes place across the liquid–vapor surface boundary by evaporation and condensation. The high mobility of liquid molecules is quantitatively related to the fact that liquid-state diffusion coefficients,  $D$ , are 5–7 orders of magnitude larger than for solids. For liquid water, the (bulk) diffusion constant is  $D = 0.6 \times 10^{-5} \text{ cm}^2 \text{ s}^{-1}$  at  $T = 298 \text{ }^\circ\text{C}$ .<sup>215,216</sup> Surface tangential diffusion rates can be even higher. The solution of the planar diffusion equation for the change of the concentration  $c_A$  of a component A

$$dc_A/dt = -Dd^2c_A/dx^2 \quad (2.4)$$

shows that the diffusion time,  $t_d$ , increases quadratically with spatial distance  $d$

$$t_d = d^2/4\pi D \quad (2.5)$$

The numerical values for the time for diffusion through one monolayer of water ( $d \approx 0.3 \text{ nm}$ ) is on the order  $t_d = 1.2 \text{ ps}$  in the absence of strong potential barriers. This is comparable to the rotational molecular reorientation time. For diffusion over a distance of  $30 \text{ nm}$ , the equivalent of 100 monolayers of liquid water, the diffusion time increases to  $t_d = 12 \text{ ns}$ . Thus, in contrast to essentially stable surface adsorbates on solids, the adsorbate layer on a liquid surface is highly mobile and immediately (picosecond time scale) begins to dilute into the bulk liquid.

The equilibrium accumulation (or depletion) of a solute component at the surface of a solution is determined by the Gibbs adsorption free energy,  $\Delta G^\circ_{\text{ads}}$ , between solvent molecules in the bulk and solvent molecules in the surface adsorption layer, yielding the equilibrium constant

$$c_s/c = \exp(-\Delta G^\circ_{\text{ads}}/RT) \quad (2.6)$$

for the ratio between surface concentration  $c_s$  and the bulk concentration  $c$  of the solute, measured in moles per liter. Negative Gibbs adsorption free energies lead to an enrichment of solute at the interface surface, and positive adsorption values  $\Delta G^\circ_{\text{ads}}$  result in a relative depletion of the solute at the surface.

A frequently applicable model for simple surface adsorption processes is the Langmuir adsorption isotherm for the solute surface coverage,  $\theta$ , as a function of the solute bulk concentration  $c$

$$\theta = bc/(1 + bc) \quad (2.7)$$

where  $\theta$  can range from 0 to 1 surface monolayer. The surface coverage  $\theta$  in the Langmuir isotherm model is

equivalent to the surface molar fraction of the solute. The adsorption coefficient  $b$  is related to the equilibrium constant by<sup>7</sup>

$$b = (1/c_{\text{solvent}}) \exp(-\Delta G_{\text{ads}}^{\circ}/RT) \quad (2.8)$$

For dilute liquid aqueous solutions, the solvent concentration is  $c_{\text{solvent}} = 55.5$  M/L. By measurements of the liquid surface coverage as a function of the bulk solute concentration, the Gibbs surface adsorption free energy can be determined for individual solute components in the liquid.

Note that the diffusion equations 2.4 and 2.5 imply that the time to establish chemical equilibrium between surface-adsorbed molecules and the bulk liquid concentration  $c$  increases rapidly with decreasing bulk concentration of the solute. For unidirectional diffusion kinetics, the equilibration time constant is proportional to

$$\tau \sim (\theta/c)^2/D \quad (2.9)$$

where  $\theta/c$  is the ratio between the surface coverage and the bulk solute concentration and  $D$  is the diffusion constant.<sup>219,220</sup> For small surface concentration enhancement ratios of  $\theta/c \leq 10$ , this time constant is in the lower nanosecond range. For enhancement by a factor of  $\theta/c \approx 100$ , approximately 100 subsurface bulk solution layers have to contribute to build up the Langmuir adsorption layer, which requires diffusion times on the order of several 10 ns to 100 ns according to the estimate for the diffusion time given by eqs 2.5 and 2.9. For many examples of aqueous solutions, which are discussed in section 5, this rapid diffusion time scale is the typical case for surface adsorption layer equilibration. Nevertheless, exceptionally long surface equilibration times in the range of up to 30 ms have been found in time-resolved surface second-harmonic generation (SHG) experiments for the solute *p*-nitrophenol at bulk aqueous concentrations in the range from 5 to 100 mM.<sup>184,219</sup> These surface formation times are 2–3 orders of magnitude longer than the free diffusion kinetics time constant; they are attributed to the presence of a large reaction barrier for surface layer formation in this particular case. The diffusion equation and the statistical thermochemical theory of Gibbs surface adsorption chemical potential and of Langmuir adsorption isotherms, as discussed here, cannot provide information on the depth distribution profiles of solutes near interface surfaces. This information, however, can be readily obtained by advanced molecular dynamic simulations such as the example shown in Figure 6 for individual electrolyte ions.

A qualitative model of the (weak partial) separation profile of anion and cation charges near an interface is available in the Debye–Hückel approximation only for electrolytic solutions. Within this model system the Gouy–Chapman theory for electrolyte solutions predicts the existence of electrostatic “ $\zeta$  potentials” and ion separation of positive and negative charges within a concentration-dependent “Debye length” at boundaries. This length is proportional to  $c^{-1/2}$ ; it extends over a liquid layer of 0.23 nm for  $c = 1$  M aqueous salt solutions and increases to 30.4 nm for  $c = 10^{-4}$  M solutions of monovalent salt ions.<sup>189,221</sup> Similarly, electrostatic image forces near dielectric surfaces are invoked in models explaining the partial depletion of the solution surface from both anions and cations. This depletion gives rise to “negative surface adsorption” and leads to the well-known increase of the surface tension of aqueous salt solutions (see, e.g., ref

171). For more detailed investigations of near-surface distribution profiles of individual atom species in a solution, photoelectron spectroscopy with tunable synchrotron radiation has a unique experimental advantage because the electron probing depth depends on the photoelectron energy and can be varied in the range of interest (e.g., in Figure 6, approximately from less than two monolayers to several tens of monolayers) in a controlled fashion. This option is further considered in section 3.2.

### 3. Photoemission from Highly Volatile Liquids

Photoemission (PE), or photoelectron spectroscopy (PES), the emission of electrons by photons, is one of the most versatile techniques in accessing the electronic structure (occupied states) of matter. When discussing PE from liquids, which, in a way, combines certain aspects from solid-state and gas-phase PE, it is useful to briefly recall the characteristic features of each system. PE spectra of atoms and molecules usually exhibit rather narrow lines, which in condensed matter, are broadened as a result of electron–phonon coupling, chemical bonding, and other interactions.<sup>113,114</sup> Also, electronic valence states of all elements are concentrated in a comparatively small energy range, whereas inner shell energies are usually well separated from neighboring emission lines. In the valence-band region of a solid, symmetry selection rules, when paired with the suitable choice of experimental parameters (such as light polarization, detection angle, etc.), can provide a wealth of structural information. This especially applies for highly ordered systems, single-crystal surfaces or oriented molecules on surfaces<sup>113,114,203,204,222–225</sup> and can be suitably accessed by *angle-resolved PE* (detecting the emission intensities at a given angle<sup>113,224,225</sup>). The surface of liquid water is also ordered to some degree, with the molecular dipole of surface molecules being found within the surface plane. Then, a considerable fraction of the molecules have a configuration with one OH pointing out of the surface;<sup>26,83,85,226</sup> hence, the existence of a boundary surface might well dictate a certain degree of orientation, even for molecular liquids. For randomly oriented gas-phase molecules, however, angular effects average out for a single parameter, the anisotropy parameter  $\beta$ . Such ordering effects should be observable in PE to some extent, even though the surface molecules are mobile and continuously undergo exchanges with molecules in the bulk.

#### 3.1. Principles of Photoemission

A comprehensive treatment of the theory of photoemission can be found, e.g., in refs 93, 113, and 114, and only a short introduction to the topic is presented here, sufficient to let readers become familiar with the most relevant phenomena in the current study. Even though only very few PE experiments with X-rays have been conducted with aqueous solutions (see section 1.1) and none have been reported for pure liquid water, it is useful to discuss PE from valence and inner shells. In a simple picture, PE refers to the ionization of an energy level (energy  $E_b$ ), which requires absorption of a photon energy with  $h\nu > E_b$ . The kinetic energy distribution of photoelectrons,  $E_{\text{kin}}(h\nu)$ , ejected from all possible occupied states is the PE spectrum, which one measures in experiments using a suitable electron energy analyzer.<sup>113,204</sup> Synchrotron radiation provides the necessary high photon flux at high energy resolution over a wide range



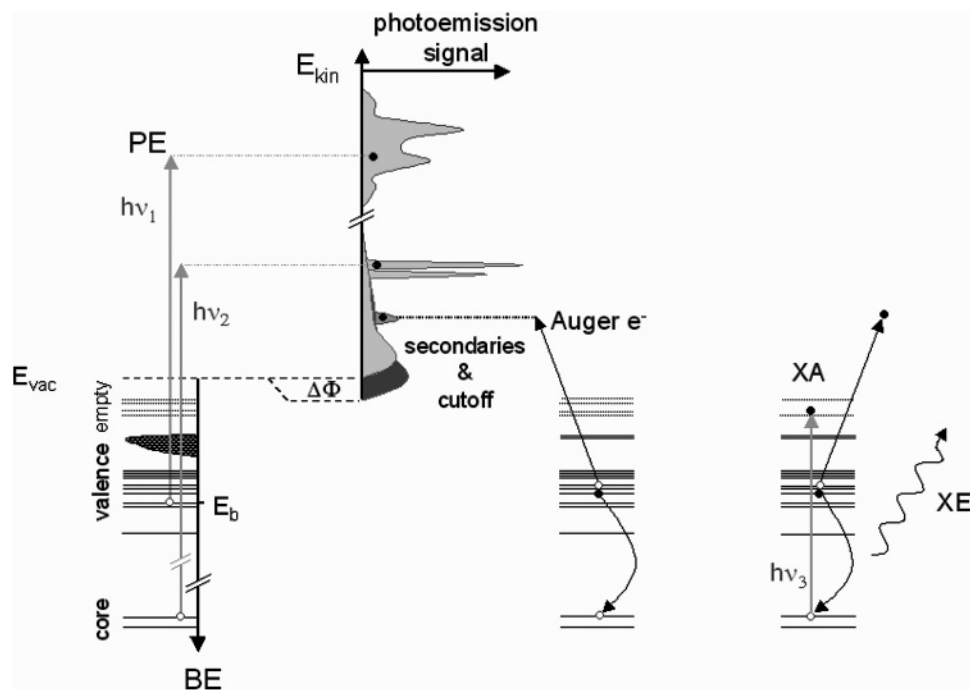


**Figure 10.** (Left) Schematic of the energy levels involved in photoemission. If the photon energy  $h\nu$  exceeds the electron binding energy  $E_b$  of a given valence or core level, an electron is ejected from the molecule (ionization), and its kinetic energy  $E_{kin}$  is measured. The distribution of  $E_{kin}(h\nu)$  is the photoemission spectrum. In the diagram, electron binding energies, BE, are drawn with respect to the vacuum level,  $E_{vac}$ , beyond which the ejected electron is free. The degree to which the measured photoemission spectrum reflects the actual density of occupied states varies for different systems and, in addition, depends on the experimental conditions. Adsorbed molecular surface dipoles with a component perpendicular to the surface cause a change of the surface potential  $\Delta\Phi$ , which results in an energy shift of the low-energy cutoff, as indicated in the figure. For the example shown, the surface dipole is assumed to be located in the top surface, the positive charge is up, and the negative charge is down. (Center) Auger electron contribution to the photoemission spectrum that can occur for core-level photoemission. (Right) Illustration of core electron promotion (by  $h\nu_3$ ) into an unoccupied valence state (X-ray absorption; XA). The absorption is probed by (Auger) electron detection or by measurement of emitted X-rays (XE).

of photon energies. Energy conservation then yields

$$E_{b,i}(N) + \hbar\omega = E_{b,f}(N-1, k) + E_{kin} \quad (3.1)$$

$E_{b,i}(N)$  denotes the energy of the initial state of the  $N$ -electron system.  $E_{b,f}(N-1, k)$  is the energy of the final state, i.e., of an ion plus a photoelectron with kinetic energy  $E_{kin}$ ;  $k$  is the initial level from which the electron was removed. This relationship between binding energy, excitation energy, and electron kinetic energy is schematically illustrated in Figure 10. For relatively low photon energies, the lower binding energy levels (valence states) can be ionized, whereas both valence and core states can be ionized when higher photon energies are used. In addition, in the case of inner-shell excitation, Auger electrons appear in the photoelectron spectrum. They result from nonradiative decay of the initial core hole, involving the filling of the core hole by an outer-shell electron, with the released energy being imparted to another valence electron, which then escapes into vacuum with a kinetic energy characteristic of the system (Figure 10, left). When excitation photon energies below the ionization threshold that fulfill the relation  $\hbar\omega = E_f - E_i$  are used, an electron from an inner shell can be lifted to an unoccupied (bound) valence state (Figure 10, right); the excitation process obeys the dipole selection rules.<sup>93</sup> The absorption cross section, obtained by variation of the photon energy, is the X-ray absorption spectrum (XAS). This is the basis for X-ray emission spectroscopy (XES), where one measures either the ejected electrons or the emitted X-rays. [In the former case, there are various possibilities for electron detection: Auger electron yield (AEY) and partial electron yield (PEY), total

electron yield (TEY), and secondary electron yield (SEY). The different techniques can be used to access different probing depths and are thus useful in distinguishing bulk from surface contributions.] One special aspect is resonant Auger spectroscopy by which the delocalization time of a core-excited electron can be probed on the few femtosecond time scale; see, for example, Nordlund et al.<sup>227</sup> for an estimate of the delocalization rate of the core-excited electron in ice.

Valence electrons are delocalized, with their wave functions extending to neighboring atoms. This, for instance, leads to the formation of the bands in solids. Valence electrons are also responsible for chemical bonding, and hence, valence PE spectra contain information on the specific nature of the bond. In addition to the discrete photoemission lines, valence PE spectra from condensed matter exhibit a pronounced (often disturbing) background of secondary electrons that peaks near the low-energy cutoff. The situation is illustrated in Figures 10 and 11. Notice that PE spectroscopies of the valence and core region are often referred to as ultraviolet photoelectron spectroscopy (UPS) and X-ray photoelectron spectroscopy (XPS), respectively. The secondary electrons are formed when the initial photoelectron loses energy (upon leaving the sample) through multiple inelastic scattering events with matter. More details are given in section 3.2. The wave functions of core electrons are much smaller, being localized near the nucleus; core electrons are not involved in chemical bonding. Core-level PE spectra usually exhibit discrete element-specific peaks (because of the  $z^2$  dependence of the respective binding energies, where  $z$  is the nuclear charge), which makes X-ray PE an element-specific method. In addition, energy shifts arising from the

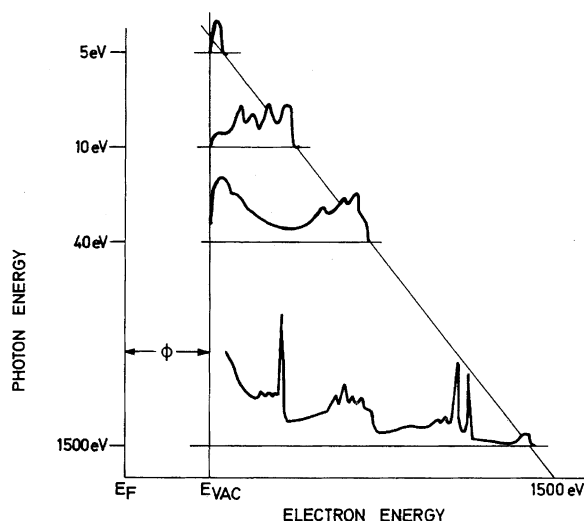


**Figure 11.** Schematic contrasting threshold, valence (UPS) and inner-shell (XPS) photoemission spectra. Threshold emission (top) is generally observed without energy analysis. The features in the band structure regime in UPS (middle traces), typically for photon energies  $< 50$  eV, are determined by selection rules. Secondary electrons arising from inelastic scattering are responsible for the signal background and the low-energy spectral cutoff (vacuum level at zero kinetic energy). Core-level photoemission spectra (bottom) are characterized by isolated atomic main photolines and, in addition, by a complex loss structure as well as by Auger electron features at constant kinetic energies. Reprinted with permission from ref 114. Copyright 1978, John Wiley & Sons Limited.

chemical environment of a given atomic species can be detected with great sensitivity. These are the chemical shifts that, in a most simplified picture, originate from the charge transfer involved in chemical bonding (and hence from the resulting change of screening behavior of the valence electrons). The method is then called electron spectroscopy for chemical analysis, ESCA.<sup>113,114,204</sup>

There are additional effects that influence the kinetic energy of the photoelectron. In particular, the sudden removal of a core electron produces a perturbation of the remaining “ionic” levels, which can relax so as to screen the core hole. Orbital changes, electronic polarization, or charge-transfer screening can hence cause spectral shifts. Obviously, an important issue in the interpretation of PE data is to investigate the extent to which the measured spectrum corresponds to the ground-state density of states. The quantum mechanical treatment of the processes is briefly sketched here: The actually observed spectral density is, in fact, the convolution of initial- and final-state wave functions, which in the most general theory is expressed by the Fermi “golden rule”<sup>113,224,228</sup>

$$R = (2\pi/\hbar) |\langle \Psi_f | H' | \Psi_i \rangle|^2 \delta(E_f - E_i - \hbar\omega) \quad (3.2)$$

which is the transition probability per unit time between two eigenfunctions;  $\Psi_i$  and  $\Psi_f$  are the initial-state and final-state electron wave functions, respectively, of the same ground-state Hamiltonian  $H_0$ .  $H'$  is the perturbation by the ionizing radiation field. In the dipole approximation, the perturbation can be expressed as  $H' = \mathbf{E} \cdot \mathbf{D}$ , where  $\mathbf{E}$  is the external electric field and  $\mathbf{D}$  is the dipole moment. The photoexcitation matrix elements in eq 3.2 can be considerably altered by selection rules, particularly when surfaces are involved, and inelastic scattering and screening processes can affect both the energies and the intensities.

For the interpretation of the PE process, the so-called “three-step”<sup>113,225,229</sup> and the “one-step” (see Martensson et al. in ref 222) models have proven useful. The latter explicitly accounts for the short mean free path of electrons in matter. In most theoretical descriptions, the PE process is assumed to be instantaneous (sudden approximation). This is indeed a fair assumption because the (photo)electron leaves the site on the subfemtosecond time scale; the exact value depends on the electron kinetic energy. Clearly, the approximation is better suited for high excitation energies. For condensed matter, however, the sudden approximation is never exact because of the effect of the mean free path.<sup>230,231</sup> For an interacting  $N$ -electron system, the sudden approximation assumes that the photoelectron is decoupled from the  $(N - 1)$ -electron state, so that the electron does not carry information on the latter configuration.<sup>232</sup> If it the remaining  $N - 1$  electrons are thought to have the same spatial distributions and energies in the final state as they had in the initial state (frozen-orbital approximation), before emission of an electron, the binding energy equals the negative of the orbital energy of the emitted electron. This is Koopman’s theorem,<sup>204</sup> neglecting relaxation of the remaining electrons and relativistic and correlation effects. A different approach in treating photoemission is the adiabatic approximation, which is generally used for low kinetic energies. Here, the electron leaves the system slowly enough that the other electrons can adjust the effective potential in a self-consistent way.<sup>233</sup>

A special situation in PE can occur for photon energies near an absorption threshold, which usually leads to the increase of a particular spectral feature in the valence band. This enhancement arises from the coherent superposition of directly photoemitted electrons and Auger electrons (resulting from the decay of the core hole following the resonant excitation). As shown in Figure 11, the PE spectra from inner shells typically exhibit some kind of satellite structure in addition to the main photolines. These are final-state effects involving multielectron excitations. Because the core hole is created on a time scale much faster than the relaxation process, the emitting atom is effectively “shaken”. It is thus no longer in its ground state during the primary photoionization. As a consequence, satellite lines occur, which correspond to the excited states of the emitting atom. Peaks at higher binding energies are the shake-up satellites. Other final-state effects (associated with the creation of a core hole) can lead to still other satellite structures, such as shake-off or shake-down satellites.<sup>113,114</sup>

Many phenomena in PE from crystalline solids are the consequence of the periodic structure, where the electrons are characterized by their momentum in addition to just the binding energy in disordered samples. A powerful method for assessing both electron binding energy and momentum is angle-resolved PE. This measures the photoelectron energy and intensity in a given emission direction as a function of the polarization vector of the incident light and with respect to a given symmetry axis. The technique, for example, is highly suitable for the investigation of the dispersion of electronic band structures, in the bulk and at the surface, which requires the determination of the electron wave vector. In surface systems, symmetry axes are usually defined by the crystalline substrate structure or by the ordered adsorbate. In some instances, for a given orbital symmetry character in combination with the symmetry selection rules, angle-resolved PE can provide clear information on the relative orientation of an adsorbed surface species,<sup>234</sup> based on

whether certain transition are allowed or forbidden for a given experimental geometry.

For randomly oriented molecules, as in the gas phase, angular effects are averaged out, and the only relevant axes in terms of symmetries are the polarization vector of the incident light and the photoelectron detection angle, expressed by the differential cross section  $d\sigma_i/d\Omega$ . Within the dipole approximation, the photoemission cross section is given by<sup>228,235,236</sup>

$$d\sigma_i/d\Omega = (\sigma_i/4\pi)[1 + (\beta_i/4)(1 + 3P_1 \cos 2\Theta)] \quad (3.3)$$

which describes the angular emission distribution in terms of the polar emission angle  $\Theta$  with respect to the polarization vector of the light.  $\beta_i$  is the energy-dependent anisotropy (asymmetry) parameter ( $2 \geq \beta \geq -1$ ), and  $P_1$  is the degree of linear polarization (Stokes parameter) of the incident light. At the magic angle  $\Theta = 54.7^\circ$ ,<sup>235</sup> the differential cross section becomes proportional to the total cross section, making this a preferential geometry when determining the cross section of a given orbital. Yet, with eq 3.3, the relative partial photoionization cross section  $\sigma_i$  can be calculated from the differential cross section, measured at any angle. For the present experiment,  $P_1 = 1$  (synchrotron light is 100% horizontally polarized), and  $\Theta = 90^\circ$ , so eq 3.3 reduces to

$$\sigma_i = 4\pi(d\sigma_i/d\Omega)(1 - \beta_i/2)^{-1} \quad (3.4)$$

Explicit cross-section plots, eq 3.3, for selected values of  $\beta$ , namely,  $-1, 0, 1, 1.5$ , and  $2$ , are shown in Figure 12. The  $\beta_i$

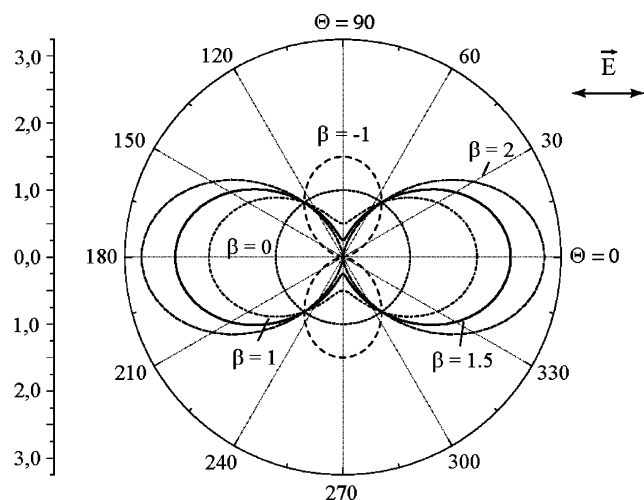


**Figure 12.** Angular distribution of photoelectrons for specific values of the anisotropy parameter  $\beta$  when linear polarized light is used. The polarization axis of the light is shown.

values for gas-phase water valence orbitals are between 1 and 2.<sup>237</sup> For  $\beta = 2$ , the maximum photoemission intensity occurs in the direction of the light polarization vector, whereas the angular distribution for  $\beta = 0$  is fully isotropic. In terms of maximizing signal, this would make the detection in the direction of the polarization vector the more favorable geometry for the liquid-jet experiment. The present design of the apparatus did not allow for this setup, however. Nevertheless, as can be seen from Figure 12, normal emission is equally suited for the detection of relative changes of  $\beta$ . Changes in  $\beta$  occur if the orbital structure changes, as is expected for hydrogen bonding in liquid water (section 5.1.3).

Aqueous liquid systems represent a sort of intermediate situation, consisting of a disordered, isotropic bulk, with the possibility of surface structural order, although it can fluctuate. In any case,  $\text{H}_2\text{O}$  orbital energies and molecular structures are different for the bulk and the surface, and these differences should be detectable in PE. Likewise, energy shifts associated with water–ion intermolecular interactions can be expected. Even the study of molecular orientational effects (although not very pronounced in aqueous systems) by angle-resolved photoemission seems feasible. As mentioned above, the water dipole moment is preferentially aligned parallel to the water surface, but with a random distribution in the surface plane. With PE, it is possible to identify the changes of the total surface dipole of an aqueous solution, for instance, as a function of salt concentration. From the magnitude of this change, information on the microscopic interfacial solution structure can be inferred, e.g., the relative location of anions vs cations with respect to the interface, which is important when studying electric double-layer formation at the solution interface. In condensed-matter photoemission studies, the orientation of dipolar adsorbed molecules has been revealed through the measured change of the sample's surface potential,  $\Delta\Phi$ .  $\Delta\Phi$  correlates with the change of the normal dipole moment and can be estimated using the Helmholtz equation<sup>238</sup>

$$\Delta\Phi = qn\Delta\mu_{\perp}/\epsilon_r\epsilon_0 \quad (3.5)$$

The elementary charge is denoted by  $q$ ,  $n$  is the number of surface dipoles per unit area,  $\Delta\mu_{\perp}$  is the change of the dipole component perpendicular to the surface,  $\epsilon_r$  is the relative dielectric constant, and  $\epsilon_0$  is the vacuum permittivity. Equation 3.5 can thus be used to calculate the preferred orientation of adsorbed molecules, provided that the molecule's dipole moment and the surface coverage are known, or vice versa. Note that the molecular dipole moment changes considerably between the gas and liquid phase. For gas-phase water,  $\mu = 1.83$  D, but for liquid water,  $\mu = 2.45$  D (see Hasted in ref 239). In the PE experiment,  $\Delta\Phi$  can be directly measured as the change of the position of the low-energy cutoff energy (secondary electron emission), as sketched in Figure 10. Depending on whether the dipole is located below or above the layer from which the electrons are ejected, the high-kinetic-energy peak or the secondary electron cutoff, respectively, will shift in energy. This leads to a change of the total width of the PE spectrum by  $\Delta\Phi$ . A decrease of the surface potential (negative  $\Delta\Phi$  as shown in Figure 10) prevails when the outermost surface layer has a positive charge.

### 3.2. Photoemission Probing Depth: Low-Energy Electron Ranges in Liquid Matter

An important aspect of surface photoelectron spectroscopy is the ability to vary the probing depth of the experiment by tuning the kinetic energy of emitted electrons. Electrons can penetrate deeper into solids at high kinetic energies. However, also at very low kinetic energies, lower than the plasma or exciton energy, electrons can travel longer distances.<sup>113,115</sup> As a result, the probing depth changes between a minimum of a few angstroms to several tens of nanometers, both at very small and at high photoelectron kinetic energies. The photoelectron signal attenuation process proceeds through a complex sequence of elastic and inelastic scattering events.<sup>240</sup> A precise theoretical description is



available only through Monte Carlo numerical simulations. In photoelectron energy-analysis spectroscopy experiments, the probing depth is limited by the occurrence of the first inelastic collision. Only direct photoelectrons or elastically scattered photoelectrons contribute to the structured part of the photoemission spectra. Their total intensity is reduced by elastic scattering. The extinction of the direct photoelectron signal can be approximated by an exponential attenuation function of the depth of the contributing subsurface layer, analogous to Beer's law. The inelastic scattering events are accompanied by large energy losses in the kinetic electron energy, and lead to a broad energy distribution of background electrons. The inelastic mean free path (IMFP) is largely determined by the material-specific dielectric permittivity function  $\epsilon(k, \omega)$ , which is the reason for the IMFP dependence on the material. An example for the experimentally determined dielectric energy loss function  $\text{Im}(-1/\epsilon)$  for water, measured for the energy loss range between 1 and 50 eV by inelastic X-ray scattering, is shown in Figure 13 (from ref 241).

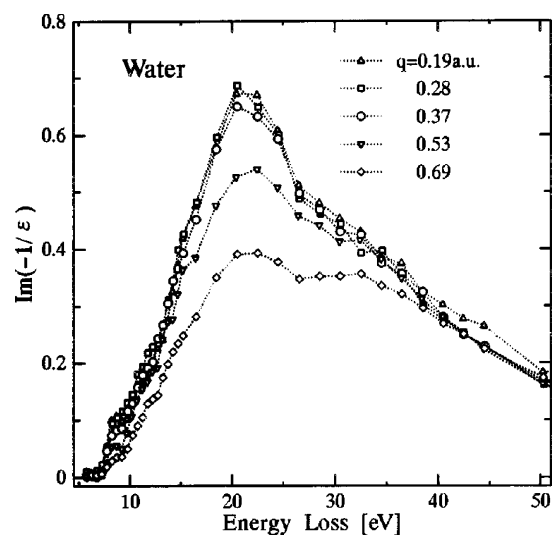


**Figure 13.** Loss function,  $\text{Im}[-1/\epsilon(q, E)]$ , of liquid water for momentum  $q$  between 0.19 and 0.69. Reprinted with permission from ref 241. Copyright 1998, American Institute of Physics.

For typical low-Z materials, the elastic scattering attenuation length (EAL) is 20–30% shorter than the IMFP. The IMFP, calculated from the material's dielectric function, is frequently used as a yardstick for the probing depth of photoelectron spectroscopy. The inelastic electron mean free paths for several well-investigated solid materials are presented in Figure 14. They show a minimum in the electron free path at kinetic energies between 50 and 100 eV, with average escape depths varying from 0.4 nm for the metals Na, Al, and Ag and for Si to the appreciably larger value of 0.8 nm for hydrogen-containing soft-matter compounds. The latter is exemplified for polymethacrylate, a well studied and extensively used lithographic photoresist, where electron penetration determines the attainable structure resolution.<sup>115,116</sup> The probing depth range can extend up to a few hundred angstroms in total-electron-yield surface EXAFS measurements.

In addition to the possibility of tuning the electron kinetic energy, the surface sensitivity can be further increased by suitable choice of the experimental geometry. One might, in general, choose the angle of incident photons or the angle of detection so as to take advantage of the selection rules

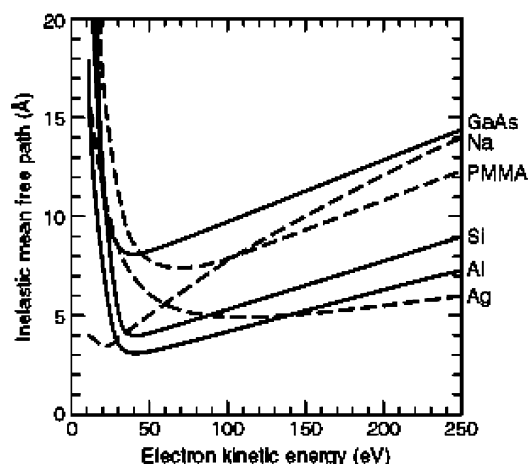


**Figure 14.** Calculated inelastic mean free paths (IMFPs) in the electron kinetic energy range below 250 eV for a number of cases representative of a wide variety of materials. From Pianetta.<sup>115</sup>

favoring surface processes.<sup>113,114,224</sup> A simpler approach is observing photoelectrons at nonnormal exit angles. Then, the mean escape depth (MED) appears shortened with respect to the electron mean free path, by a geometrical factor  $\cos(\Theta)$ , giving

$$\text{MED} = \text{IMFP} \cos(\Theta) \quad (3.7)$$

When electrons are observed at 90° with respect to the synchrotron light for a cylindrical (liquid-jet) target, electrons with surface emission angles ranging from 0° to 90° enter the energy analyzer. According to eq 3.6, for this cylindrical target geometry, the MED probing depth ranges change with the emission angle, as indicated by the second contour below the surface contour line in Figure 15. Integration of the MED

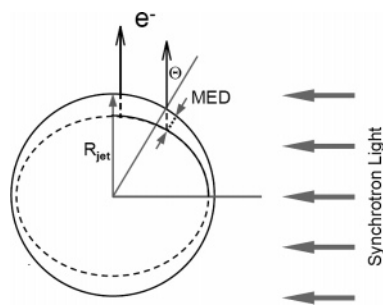


**Figure 15.** Schematic of the liquid-jet cross section showing the variation of the photoelectron mean escape depth (MED) with respect to the electron exit angle. The MED is the projection of the electron inelastic mean free path, IMFP, onto the local surface normal vector:  $\text{MED} = \text{IMFP} \cos(\Theta)$ . In reality, the MED is much smaller than the liquid-jet diameter (6  $\mu\text{m}$ ), and the angle-averaged mean escape depth is  $\langle \text{MED} \rangle = 0.63 \text{IMFP}$ .

over the whole contributing surface range, from  $\Theta = 0$  to  $\pi/2$ , yields the effective cylinder surface probe volume

$$\Delta V_{\text{probe}} = \text{IMPF} \times R_{\text{jet}} \quad (3.7)$$

This is equivalent to an effective average probe depth of

$$\langle \text{MED} \rangle_{\text{av}}^{\text{cyl probe}} = (2/\pi) \text{IMFP} \quad (3.8)$$

As a result, the average subsurface probing depth in the cylindrical liquid-jet PE study is reduced to 63% compared to the case of a planar target at normal emission.

Unfortunately, for liquid water, the quantitative electron range is still highly controversial because it is poorly known, despite its tremendous importance in electron energy deposition in radiological research and application. At present, minimum electron range values for liquid water are accessible by calculation only. These show a scattering range for the escape depth data from 0.5 to 2.0 nm in the minimum IMPF when different theoretical models are applied.<sup>242–244</sup> Current theoretical results for the inverse IMPF values for liquid water, from ref 242, are shown in Figure 16, together

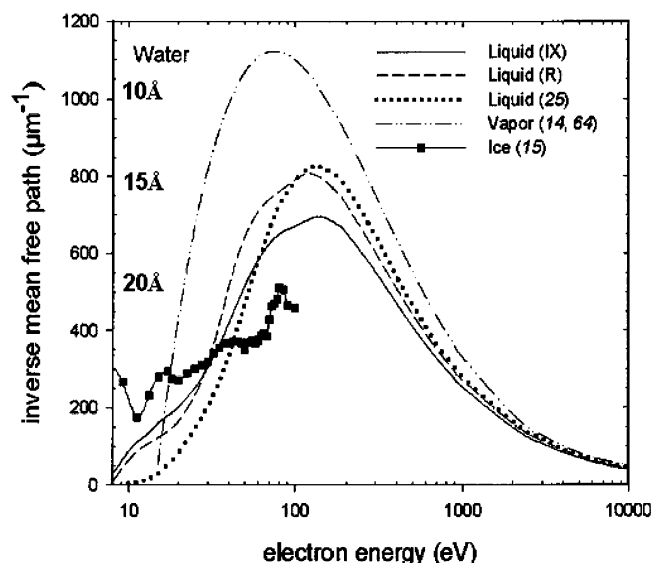


**Figure 16.** Inelastic *inverse* mean free path of electrons in water in different phases calculated using different theoretical models. The squares are experimental data for amorphous ice. Reprinted with permission from ref 242. Copyright 2005, Radiation Research Society.

with the scarcely available experimental data for water vapor and ice. The generally acknowledged minimum IMPF value of 2–3 monolayers at 100–200 eV, reported by Jablonski and Powell,<sup>117,240</sup> is a lower bound of the present scattering range of IMFP data for liquid water. Michaud et al.<sup>243</sup> reported, for  $E_{\text{kin}} = 67$  eV, an experimental IMFP of 2.3 nm for amorphous ice layers at 15 K. Kurtz et al.<sup>246</sup> observed an attenuation length  $AL = 1.6$  nm for 68 eV electrons for ice at 90 K. In part, these large experimental discrepancies might originate from porosity effects or from clustering in the nanometer-range ice films.<sup>247</sup> They might also be caused by electron interference phenomena in condensed matter. Similarly, the calculated IMFPs for electrons in liquid water also depend on measurements of optical constants of liquid water in the important photon energy range between 30 and 100 eV, where vapor absorption is a problem. For the analysis of aqueous solution surface concentration profiles from PE data, this is the largest source of error, at present. It appears highly desirable that narrower error intervals should be established for the energy dependence of the electron IMPF range in liquid water.

Photoelectrons can also excite the water molecules by inelastic collisions in a manner similar to photoexcitation.<sup>248,249</sup> In the high-energy limit, the excitation probability is proportional to the optical dipole oscillator strength, which, in turn, is closely related to the energy loss function,  $\text{Im}[-1/\epsilon(k, \omega)]$ .<sup>241,249</sup> Hence, fast electrons have a tendency to excite essentially the same states as white light and lose

the corresponding amount of kinetic energy, as is further discussed in section 5.1.1.

#### 4. Liquid Water in a Vacuum: The Liquid Microjet Technique

Methods for the preparation of a suitable liquid-water surface for photoelectron spectroscopy in a vacuum are very different from the established procedures for handling solid-state surfaces and were not fully developed until the late 1980s.<sup>119,250–252</sup> The newly emerging experimental techniques for preparing stationary free vacuum surfaces of volatile liquids have also immediately found several applications in related disciplines of physics and physical chemistry. It was recognized, for instance, that ions could be evaporated directly from liquids using moderately intense laser pulses.<sup>130,202,253</sup> In particular, solvated proteins or nucleic acids, which are present in aqueous solutions in partially ionized form, can be laser-desorbed very efficiently from the vacuum liquid surface in their natural liquid protonated or deprotonated states. This requires only moderate-power near-infrared radiation pulses in the 2.5–3  $\mu\text{m}$  wavelength range. By subsequent mass-analysis isolated biomolecules and noncovalently bound aggregates, complexes and chelates could thus be studied without any fractionization effects by artificial ionization sources. The mass range covered thus far extends from simple amino acids through medium-size proteins such as insulin (5 kDa) and up into the 100 kDa range for larger bioproteins, such as cytochrome *c* and hemoglobin.<sup>254–257</sup> In another new application, Saykally and co-workers<sup>84,90</sup> have employed the surface of a 20  $\mu\text{m}$  liquid jet of water in a vacuum by NEXAFS. In NEXAFS experiments, emitted photoelectrons are reflected from neighboring atoms in the coordination shell. This leads to photon-energy-dependent interferences in the photon absorption cross section and to complementary interference structures in the emission cross sections of photoelectrons originating from the photon absorption process. In this study, one detects either the radiation-induced negative photoelectron current from the liquid-jet surface or the positive current signal that results from the ejection of protons produced by photodissociation of water molecules. The proton NEXAFS signal is different from the corresponding electron signal because the slowed down electrons can diffuse over large distances and, thus, are proportional to the bulk water coordination structure factor. In contrast, the positive proton current can penetrate less than one molecular layer at the water liquid surface and, therefore, can be used as an extremely short-range, exclusively surface sensitive detection tool for the coordination shell structure of the outermost layer at the water surface.

Vacuum surfaces of volatile liquids have also found important technical applications for the generation of laser-plasma-produced extreme ultraviolet radiation for use in the next generation of semiconductor lithography at 13.4 nm photon wavelength.<sup>258,259</sup>

##### 4.1. Environmental Chamber or in Situ Approach

To overcome the vacuum problems caused by the millibar-range vapor pressure of liquid water, in early ESCA studies on liquids, Siegbahn and Siegbahn<sup>118,260</sup> used liquid solvents of low vapor pressure, such as formamide ( $\sim 10^{-2}$  mbar at 298 °C), ethylene glycol, cooled ethanol, and very concentrated (14 M) aqueous solutions of LiCl. With this high salt content, the freezing point could be lowered to –20 °C, and

a vapor pressure of approximately 0.5 mbar was attained in this first XPS study of liquid-water solutions (compare section 1.1). The liquid is usually a steadily refreshed flowing jet or a flowing film on a metal substrate needle of about 1-mm diameter. This is contained in a probe chamber under its own vapor pressure,  $p_{\text{gas}}$ , and it is separated by differentially pumped, narrow collimation slits from the actual high-vacuum part of the photoelectron energy analyzer equipment. The crucial experimental parameter for such high-gas-pressure (sometimes also called “environmental” or “in situ”) target chambers is the electron free penetration length. It is on the order of magnitude of the electron mean free path

$$l = (n_{\text{vap}} \sigma_{\text{el}})^{-1}, \quad (4.1)$$

which is determined by the electron total scattering cross section,  $\sigma_{\text{el}}$ , at the given kinetic energy and by the density,  $n_{\text{vap}}$ , of gas molecules. In the early literature, von Ardenne<sup>261</sup> quantified, for the maximum allowable vacuum pressure, a value of

$$p_{\text{max,air}} (\text{mbar}) = 1.5 \times 10^{-6} U_{\text{el}} (\text{eV}) / l_{\text{transit}} (\text{cm}) \quad (4.2)$$

for electron beams with an acceleration voltage  $U_{\text{el}}$  and a length  $l_{\text{transit}}$  of the beam transit path in the region with elevated pressure  $p_{\text{gas}}$ . Equation 4.2 has been verified for electron energies between 10 keV and 1 MeV.<sup>261</sup> Accordingly, in Siegbahn’s first liquid XPS experiment, the probe chamber beam path was restricted to the order of  $l = 1$  mm, and liquids with vapor pressures lower than 0.1–0.5 mbar were used. Comparable  $pl$  values are used in modern environmental electron scanning microscopes (EESMs), allowing the study of wet clay or wet biological samples.<sup>262</sup> The jet development is being further advanced as recently described for an in situ synchrotron light photoelectron apparatus, used for observations of melting ice samples and salt brines.<sup>29,263</sup>

A direct illustration of the deterioration effects of the photoelectron spectra in a gas layer of CO was recently published by Steinrück et al.,<sup>264</sup> who reported precision measurements of the attenuation of photoelectrons emitted from a palladium single-crystal surface that subsequently passed through an in situ probe cell at elevated gas pressure. The effective cell transit path was  $l_{\text{eff}} = 0.17$  cm. A series of attenuated photoelectron spectra is shown in Figure 17

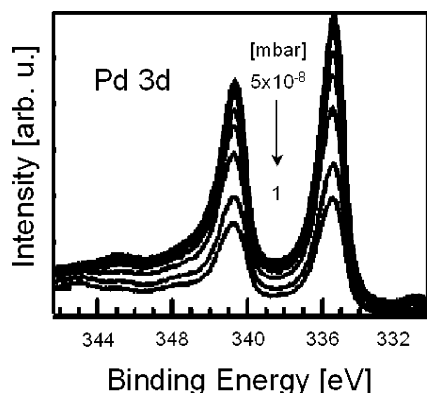


**Figure 17.** Pd 3d<sub>5/2</sub> photoemission spectra from Pd(111) single crystal as a function of CO pressure, measured in a 0.17-cm-long in situ probe cell. CO pressures are  $5 \times 10^{-8}$ , 0.1, 0.2, 0.4, 0.7, and 1 mbar. Signal attenuation due to inelastic scattering is not accompanied by energy shifts. Reprinted with permission from ref 264. Copyright 2005, American Institute of Physics.

for X-ray-emitted Pd 3d photoelectrons with kinetic energy  $E_{\text{kin}} = 1150$  eV at different cell pressures  $p_{\text{gas}}$  up to 1 mbar. The observed peak intensity attenuation,  $I/I_0$ , is found to follow the exponential attenuation law

$$\ln I/I_0 = -\sigma_{\text{el}} l_{\text{eff}} p_{\text{gas}} / kT \quad (4.3)$$

where  $\sigma_{\text{el}}$  designates the electron cross section,  $k$  is the Boltzmann constant, and  $T$  is the gas temperature.<sup>264</sup> Furthermore, the attenuated spectra in Figure 17 show negligible energy broadening of the approximately 1 eV wide Pd 3d photoelectron peak, even at the intensity reduction to 40% ( $\sim 1/e$ ) at 1 mbar gas pressure. This shows in a direct, reversible experiment that the photoelectron spectrum essentially remains unaltered in structure as the probing depth is changed; signal from deeper regions is attenuated by elastic electron scattering, but it essentially remains unaltered in structure. The total signal can be approximated as an exponentially weighted integral of the subsurface depth distribution density function  $n_A(z)$  for the photoelectron emitting atoms

$$I_A = \int n_A(z) \exp(-z/\text{IMFP}) dz \quad (4.4)$$

weighted by the electron attenuation factor analogous to eq 4.3, where  $z$  is the depth at constant attenuation atom density.

Also, from this measurement,<sup>264</sup> one can obtain the IMFP value of  $nl = 4.6 \times 10^{15}$  molecules  $\text{cm}^{-2}$  for 1.15 keV electrons in gaseous nitrogen, which is in good agreement with the literature.<sup>116,117</sup> For environmental chambers operating with water vapor, the gas cross section is approximately 25% smaller than for  $\text{N}_2$ , with a corresponding increase of the IMFP electron range. For photoelectrons with 100 eV kinetic energy, which have the shortest probing range in the liquid surface, the vapor-phase cross sections,  $\sigma_{\text{el}}$ , increase also by 300–500%. This would require a reduction of the total transfer path in an environmental chamber to less than 200  $\mu\text{m}$ . Such a reduction is impractical because the effective electron scattering path length in the outgoing, diverging vapor stream on the high-vacuum side of the exit aperture of the environmental pressure chamber does not decrease when the chamber is shortened.

## 4.2. Free Vacuum Surface of Micron-Sized Water Jets

### 4.2.1. Area-Limited Free Liquid Surface

In an alternative, complementary approach to differentially pumped transfer vacuum chambers, the free vacuum surface of a liquid in a high-vacuum environment can also be produced by shrinking the exposed liquid surface area cross section,  $D_0$ , to the Knudsen limit. Then,  $D_0$  becomes smaller than the electron mean free path length at the equilibrium vapor pressure,  $p_{\text{vap}}$ , of the surface. The expanding vapor from the limited-area surface then follows a diverging path with vapor density  $n = p/k_B T$ , decreasing with increasing distance  $x$  from the liquid surface. The effective electron path at large distance  $x$  from the liquid surface is then given approximately by the integral

$$l_{\text{eff}}(x) = (k_B T / p_{\text{vap}}) r_0 \int dx' n(x') \quad (4.5)$$

For a spherical-vapor-expansion geometry with a source area radius  $r_0 = D_0/2$  and  $n(x) = x^2 p_{\text{vap}} / k_B T$ , the effective path length is



$$l_{\text{eff}}^{\text{sph}}(x) = 2/D_0 - 1/x \quad (4.6)$$

Similarly, for a cylindrical expansion geometry from a round liquid jet, the effective absorption length is

$$l_{\text{eff}}^{\text{cyl}}(x) = \ln(2/D_0) - \ln(1/x) \quad (4.7)$$

Accordingly, a narrow liquid jet with a continuously evaporating water surface can be used directly as a free surface in a high vacuum when the jet diameter  $D_0$  is smaller than the electron mean free path at the surface-temperature-specific vapor pressure,  $\lambda_{\text{el}} \leq 10 \text{ mbar cm}/p_{\text{vap}}$ . Here,  $\lambda_{\text{el}}$  and the equilibrium vapor pressure  $p_{\text{vap}}$  refer to the vapor pressure at the instantaneous surface temperature of the liquid jet.

The use of fast flowing jets, with flow velocities between 30 and 120 m/s, as a free liquid surface in a vacuum also solves the serious problem of very efficient evaporative cooling of high-vapor-pressure liquids in a vacuum by the continuous rapid replacement of liquid. Moreover, in PES experiments from electrically nonconducting or poorly conducting aqueous liquid surfaces, electrostatic charging problems are considerably reduced through rapid liquid exchange.

#### 4.2.2. Local Equilibrium at the Jet Surface

For a liquid surface in equilibrium with its gas phase, molecules condense and evaporate at the liquid surface at a rate per unit area of

$$j = \langle v_{\text{gas}} \rangle n_{\text{gas}} = 1/4 (8kT/m_{\text{gas}})^{1/2} (p_{\text{gas}}/kT) \quad (4.8)$$

We can conveniently approximate the surface coverage in units of langmuirs (L). One langmuir is defined as the product  $1.3 \times 10^{-6} \text{ mbar s}$ . This means that, at  $10^{-6} \text{ mbar}$  pressure, the number of molecules necessary for the accumulation of a monolayer is provided within 1 s. For liquid water, with 8 mbar vapor pressure at 0 °C, the time for evaporation of a monolayer is about 100 ns. Hence, after an evaporation or condensation event, it takes 100 ns before a second molecule evaporates or impacts from the gas phase at the same surface site. In contrast, collisions with adjacent liquid molecules occur on the 1 ps time scale and lead to thermodynamic equilibrium within tens of picoseconds. Given the very large difference in time scales, i.e., 4 orders of magnitude, for fast liquid–liquid collisional relaxation vs gas-phase impact collision events at the liquid surface, this flowing-jet system is close to local thermodynamic equilibrium. Still, existing deviations from equilibrium conditions can, in principle, be easily investigated in molecular dynamics simulations for the molecular systems in question.

The formation of an adsorbate layer on a fresh surface is determined by the diffusion kinetics of the solute. In the absence of an energy barrier and in the absence of convection, the rate of arrival of molecules at the surface is given by

$$dc/dt = (D/\pi)^{1/2} ct^{-1/2} \quad (4.9)$$

At room temperature, the bulk diffusion coefficient  $D$  for water in liquid water is  $6 \times 10^{-6} \text{ cm}^2 \text{ s}^{-1}$ .<sup>265</sup> Integration of eq 4.9 yields

$$c_s = 2(D/\pi)^{1/2} ct^{1/2} \quad (4.10)$$

for the accumulation of the surface concentration,  $c_s$ , as a function of elapsed time  $t$ . This simplified theory has been improved by consideration of the desorption of molecules from the surface film, leading to slightly more complex formulas with formation of the equilibrium adsorbate for longer times.<sup>265</sup> The time for formation of a surface adsorbate density of  $n = 2 \times 10^{14} \text{ cm}^{-2}$  in water ( $D = 2 \times 10^{-5} \text{ cm}^2 \text{ s}^{-1}$ ) from a bulk concentration of  $c = 1 \text{ mol/L}$  is approximately  $t \approx 4 \times 10^{-9} \text{ s}$  in the bulk liquid, and it increases to  $t \approx 4 \times 10^{-5} \text{ s}$  for  $c = 0.01$ ! Because the typical liquid jet moves to the observation region at 1 mm distance from the nozzle exit in 10  $\mu\text{s}$ , the surface formation time should be less than  $10^{-4} \text{ s}$ . With the presently investigated concentration limits for aqueous solutions, we have not yet been able to observe an increase or decrease of surface concentrations as a function of distance on the 10  $\mu\text{s}$  time scale of the present liquid-jet experiment. Other liquids with higher viscosities and smaller diffusion coefficients, such as, perhaps, deeply supercooled water solutions or solutions with glycerol additives, can attain significantly larger diffusion times and should show significantly larger surface equilibration time delays.

#### 4.2.3. Liquid-Jet Surface Potential

Because neat liquid water is an insulator, low-electrolyte-concentration aqueous solutions can become charged when being illuminated with high-brilliance synchrotron light, although the charge is removed rapidly and efficiently with the flowing jet.<sup>119,131</sup> The electrical capacity of the thin liquid-jet filament is approximately  $10^{-14} \text{ F}$ . An estimated maximum synchrotron radiation flux of  $10^{12} \text{ photons/s}$ , focused on the 6–10  $\mu\text{m}$  diameter liquid jet, is expected to produce  $10^{12}$  photoelectrons, which is equivalent to an  $I_{\text{PE}} = 0.17 \mu\text{A}$  current. In a completely insulating, fast-streaming liquid jet, this current  $I_{\text{PE}}$  is transported with the jet streaming velocity  $v_{\text{jet}}$ . The linear charge density on the liquid beam filament is therefore given by  $\rho_{\text{PE}} = I_{\text{PE}}/v_{\text{jet}}$ , and the photoemission charge-induced electrostatic potential  $U_0$  at the surface of a jet with radius  $r_{\text{jet}}$  is<sup>266</sup>

$$U_c = 1/(4\pi\epsilon_0\epsilon)(2/D_0)(I_{\text{PE}}/v_{\text{jet}}) \quad (4.11)$$

This potential is on the order of one to several volts for typical experimental values. A jet with a 3  $\mu\text{m}$  radius traveling at a velocity of 120 m/s and carrying a streaming current of  $I = 1 \text{ nA}$  has a surface potential of 1.8 V.

In addition, in poorly conducting fast-streaming liquids with a low degree of ionic dissociation, electrokinetic effects can lead to significant streaming currents and associated streaming electrical potentials, for which a correction might also have to be applied. Their magnitude and sign can be influenced dramatically by small impurities. For neat water, impurities as low as 1 ppb already change the pH value<sup>252</sup> and thus the charge flow kinetics. Buffered solutions with higher salt concentrations are more insensitive to electrokinetic charging. When the radiation source and the jet are completely stabilized, this offset voltage  $U_0$  is constant, and the PE spectrum of neat water can be measured. In routine experiments, a more efficient way to remove charge is to increase the electrical conductivity by adding a small amount of salt.

The conductivity of an aqueous electrolyte solution for fully dissociated monovalent electrolytes (e.g., NaCl) is given to first order by  $\sigma = L_0 c_{\text{salt}} \approx (110 \Omega^{-1} \text{ mol}^{-1} \text{ cm}^2) c_{\text{salt}}$ . For

example, a 0.01 mol/L aqueous solution of NaCl has a conductivity of  $\sigma = 1.1 \times 10^{-2} \Omega^{-1} \text{ cm}^{-1}$ .<sup>120,130</sup> The resistance of an aqueous-solution 6  $\mu\text{m}$  diameter jet filament of  $l = 1 \text{ mm}$  length with a cross section  $A = 0.5 \times 10^{-6} \text{ cm}^2$  is thus  $R = l/A\sigma = 4.5 \text{ M } \Omega$ . For the considered case of a 6  $\mu\text{m}$  jet irradiated by  $10^{12}$  extreme ultraviolet (EUV) photons per second, this will cause an increase of the liquid-jet surface potential of  $U = IR = 0.76 \text{ V}$  by the photoelectron emission. The onset of surface charging can be observed easily in the photoelectron spectra as a shift of the liquid-water valence photoelectron peaks with respect to the simultaneously present vapor-phase water photoelectron peaks. Then, three different strategies are available for controlling the influence of charging during experiments: (1) keeping the synchrotron radiation flux stable and measuring the photoelectron spectra at a constant, charging-induced, but known energy offset; (2) adding salt to the aqueous solution to increase the electrical conductivity of the liquid jet; and (3) reducing the radiation intensity until the radiation-induced electrical charging of the liquid jet is reduced to an insignificant level.

In the literature, the magnitude of the intrinsic surface potential of the water–air interface has been discussed extensively.<sup>7,239,265</sup> Nevertheless, its accurate value has remained controversial. Davies and Rideal recommended a most likely value of  $\Psi_{\text{es}} \approx -0.1$  to  $-0.2 \text{ V}$  for the free surface potential of neat liquid water. With the streaming-jet method employed here, in the PE experiments, the presence of a water surface potential  $\psi_{\text{es}}$  is equivalent to a nonvanishing electrostatic linear charge on the liquid-jet axis. Using the voltage current relation of eq 4.10, the value of the surface potential can be easily obtained by the considerably simpler and accurate measurements of the current transported by the streaming liquid beam.<sup>252,266</sup> Through this alternative technique of liquid-jet current measurements, which does not require reference to electrode metal work functions and electrical contact potentials at the liquid-beam-forming nozzle walls, the external vapor–liquid and vacuum–liquid surface potential of neat water jets is ensured to be smaller than 10 meV.

## 5. Photoemission from the Liquid Microjet with Synchrotron Radiation

Photoemission from liquid water and aqueous solution is still a young emergent field of research, with only a handful of papers published to date. In the following section, we present an overview of our recent PE studies which were performed using high-brilliance synchrotron radiation. The photoemission measurements described here, using extreme ultraviolet (EUV) light, were conducted at the MBI undulator beamline (U125) at the third-generation synchrotron radiation facility BESSY, Berlin, Germany. This beamline provided photon energies up to 120 eV, with about  $4 \times 10^{12}/\text{s}$  per 0.1 A ring current photon flux, and energy resolution better 6000. Usually, lower resolution of about 100 meV was used, though, in favor of increased photoemission signal. This is fully sufficient given that the peak widths of liquid features are typically  $>0.5 \text{ eV}$ . The sampling time of a typical spectrum was about 30 min.

For all present experiments, the synchrotron light intersected the laminar liquid jet at normal incidence with respect to the liquid-jet flow direction, and electron detection was normal to both the jet direction and the light polarization vector (Figure 18). Angular dependences of photoelectron

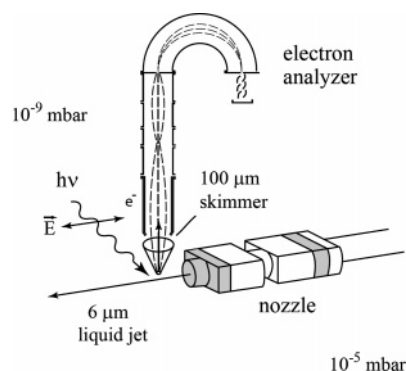


**Figure 18.** Experimental setup of the liquid microjet photoemission experiment. Polarization vector of the synchrotron light  $E$  is perpendicular to the direction of electron detection and parallel to the direction of jet propagation. Photoelectrons pass through the skimmer, acting as differential pump, at the entrance of a hemispherical electron energy analyzer. The pressure in the interaction chamber is  $\sim 10^{-5} \text{ mbar}$ , and the jet velocity is  $120 \text{ ms}^{-1}$ .

emission cross sections could not be studied in the given experimental setup. The focal size of the synchrotron light, about 250  $\mu\text{m}$  horizontal and 120  $\mu\text{m}$  vertical, was much larger than the jet diameter. Photoelectrons must pass through a 100- $\mu\text{m}$  orifice that separates the jet main chamber ( $10^{-5} \text{ mbar}$ ) from the electron detection chamber ( $10^{-9} \text{ mbar}$ ). The latter houses a hemispherical electron energy analyzer, equipped with a single electron multiplier detector (which was recently replaced by a multichannel detector). This chamber is pumped by two turbomolecular pumps. The working pressure in the jet chamber,  $10^{-5} \text{ mbar}$ , is maintained using a set of liquid-nitrogen cold traps, in addition to a 1500 L/s turbomolecular pump. A differential pumping stage connects the liquid-jet main chamber and the end chamber of the beamline ( $10^{-9} \text{ mbar}$ ), housing the refocusing mirrors. Helmholtz coils were used to compensate for the Earth's magnetic field. For the PE experiments, salt solutions were made using highly demineralized water (conductivity ca. 0.2  $\mu\text{S}/\text{cm}$ ), and the salts were of the highest purity commercially available (Aldrich).

## 5.1. Liquid Water

### 5.1.1. Reference Energy and General Considerations

Typical PE spectra of pure liquid water as a function of photon energy, 80, 100, and 120 eV, are shown in Figure 19. The spectra are vertically displaced relative to each other, with the intensities normalized to the height of the  $1b_1$  (liquid) peak. The amount of gas-phase water (subscript g) signal observed in the spectra, resulting from evaporation from the liquid surface, depends on the focal size of the synchrotron light. Importantly, the peak position and narrow width of the  $1b_{1g}$  feature are the same for sampling from different locations. Hence, gas-phase and liquid-phase signals must originate from identical potentials. Experimentally, this was confirmed by moving the liquid jet off sight from the spectrometer detection axis until all of the signal contribution from liquid water was below the detection limit. Then, the experimental energies of the liquid can be safely referenced with respect to the precisely known  $1b_{1g}$  gas-phase energy, which serves to define the absolute calibration of the binding energy axis in Figure 19. The rich structure in the 10–40 eV binding energy region arises from the four valence molecular orbitals of the water molecule that have  $C_{2v}$  symmetry:  $(1a_1)^2(2a_1)^2(1b_2)^2(3a_1)^2(1b_1)^2$  electronic ground-

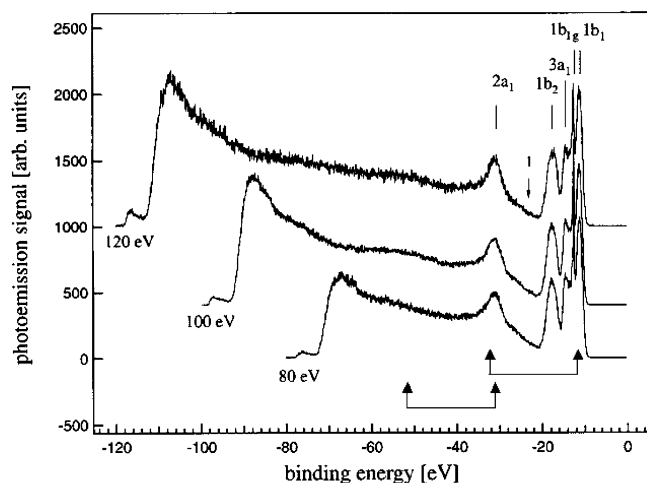


**Figure 19.** Photoemission spectra from a 6  $\mu\text{m}$  diameter liquid-water jet obtained for 80, 100, and 120 eV photon energy. The four outer orbitals of water,  $1b_1$ ,  $3a_1$ ,  $1b_2$ , and  $2a_1$ , are labeled. Emission intensities are normalized to the  $1b_1$  (liquid) feature, and electron binding energies are relative to the vacuum. The sharp feature,  $1b_{1g}$ , arises from gas-phase water. The large spectral background is due to secondary electrons, and weak features on top of the background can be assigned to electron energy losses due to quasi-optical excitation. This is exemplified by the two pairs of arrows, indicating the positions of 20 eV losses for initial  $1b_1$  and  $2a_1$  electrons. Reprinted with permission from ref 269. Copyright 2004, American Chemical Society.

state configuration.<sup>267</sup> The valence orbital energy level diagram and a presentation of the orbitals of the gas-phase  $\text{H}_2\text{O}$  molecule are shown in Figure 20. The broad emission features near 50 eV, as well as some weaker features at lower binding energy, can be assigned to specific  $\text{H}_2\text{O}$  transitions of liquid water. In addition, this higher-binding-energy range of the spectrum also contains rather unspecific contributions

from secondary electrons, giving rise to the broad background (see section 3.1).

To extract precise values for the liquid-water orbital energies, the liquid contributions must be distinguished from the gas-phase contributions. This is done by the subtraction of a pure gas-phase PE spectrum from a PE spectrum exhibiting the maximum signal from the liquid, as shown in Figure 21. The spectra presented here were obtained for a 60 eV photon energy, but identical electron binding energies and peak widths were found when other energies ( $<120$  eV) were used. The top panel displays the measured liquid spectrum, from which a Shirley-type background<sup>268</sup> was subtracted. The center panel is the pure gas-phase spectrum, measured by lowering the jet with respect to the synchrotron light path. Then, the difference PE spectrum (with properly scaled relative  $1b_{1g}$  intensities), bottom curve, is our best experimental approach to the valence photoemission spectrum from pure liquid water. Liquid orbital energies are noticeably shifted to lower values as compared to the gas phase, and in addition, liquid peaks are considerably broadened. Yet, the overall pattern of the gas-phase spectrum is maintained in the liquid spectrum. Photoemission spectra of liquid  $\text{D}_2\text{O}$ , not shown here, were indistinguishable from spectra of  $\text{H}_2\text{O}$ ;<sup>269</sup> hence, no influence of zero-point vibrations can be observed under the present experimental conditions.

As mentioned in section 3.2, for sufficiently high kinetic energy, photoelectrons passing through liquid water can excite water molecular transitions similarly to photons.<sup>248,249</sup> These specific excitation losses are responsible for the additional weakly discernible peak structures on top of the broad secondary electron background. The feature near 50 eV (Figure 19) and faint shoulders on the wings of the  $2a_1$  peak are assigned to the same excitations as are observed in the absorption spectrum of liquid water,<sup>270</sup> as well as in the

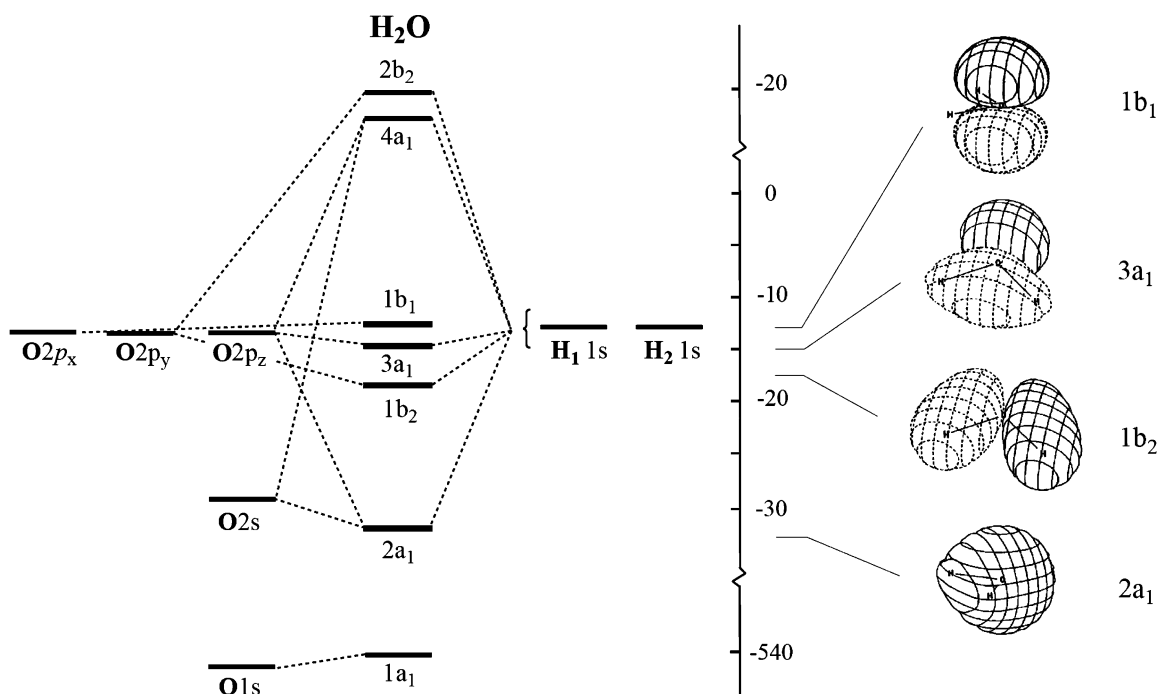


**Figure 20.** (Left) Energy level diagram of occupied molecular orbitals of gas-phase  $\text{H}_2\text{O}$ . Adapted from ref 297. (Right) Orbital pictures of the  $\text{H}_2\text{O}$  molecule. Different signs of the wave function are indicated by solid and dashed lines. Adapted from ref 298. The  $2a_1$  orbital is strongly O  $2s$ –H  $1s$  bonding and has largely O  $2s$  character. The  $1b_2$  and  $3a_1$  orbitals are oriented in the molecular plane. These orbitals mix strongly with the hydrogen orbitals to make the OH bonding orbital. The  $1b_1$  state is primarily of oxygen lone-pair character (O  $2p_x$ ) and is thus nonbonding.



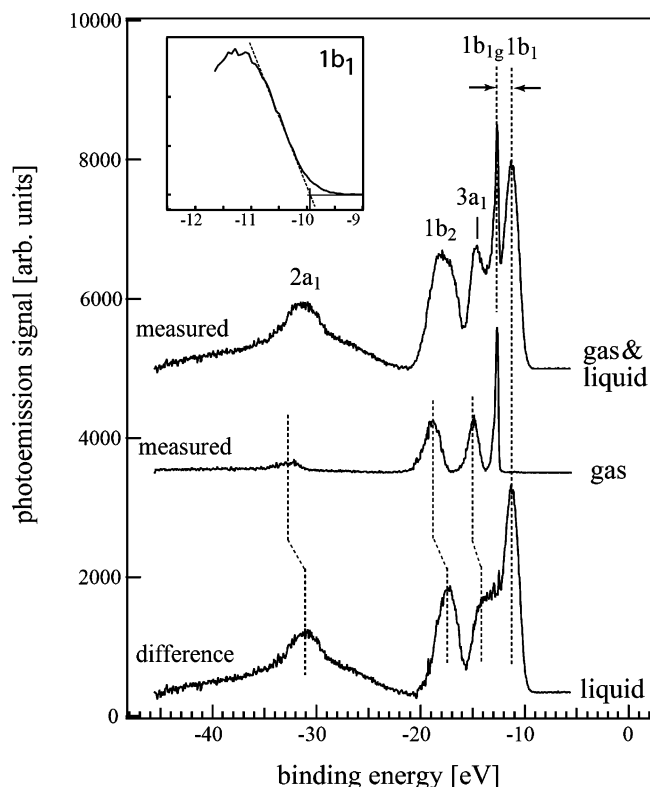


**Figure 21.** Photoemission spectra from (top) liquid water, (center) gas-phase water, measured at 60 eV photon energy, and (bottom) difference spectrum. The  $1b_{1g}$  gas-phase peak provides the energy reference because its spectral positions are identical in the two upper spectra. Comparison between the two lower spectra shows that liquid features are broadened and red-shifted by about 1.4 eV relative to gas-phase water. The gas-to-liquid orbital peak shifts are indicated in the figure by dashed lines. The onset of the photoemission signal is 9.9 eV, shown enlarged in the inset. Reprinted with permission from ref 269. Copyright 2004, American Chemical Society.

$\text{Im}[-1/\epsilon(q, E)]$  spectrum obtained from inelastic X-ray scattering experiments at small momentum transfer.<sup>241</sup> The loss function determined in ref 241 was already shown in Figure 13. A strong electron energy loss maximum can be observed at 20 eV, as well as a weaker one in the side lobe near 30 eV. Thus, for example, the broad peak near 50 eV in Figure 19, which is barely distinguishable from the secondary background, was attributed to originate from  $2a_1$  primary photoelectrons exciting the most probable 20 eV electron energy loss channel in the loss function (Figure 13). Analogous wiggles in the wings of the low- and high-binding-energy sides of the  $2a_1$  feature, in part, can be attributed to initial  $1b_1$  photoelectrons, involving the same loss channel. This is depicted by the two groups of arrows in the figure.

### 5.1.2. Orbital Energies and Peak Broadening

The experimentally observed gas-to-liquid peak shifts in the PE spectra are slightly different for the various orbitals:<sup>269</sup>  $1.45 \pm 0.05$ ,  $1.34 \pm 0.12$ ,  $1.46 \pm 0.06$ , and  $1.72 \pm 0.16$  eV for the  $1b_1$ ,  $3a_1$ ,  $1b_2$ , and  $2a_1$  orbitals, respectively. This places the center of the lowest-binding-energy peak,  $1b_1$ , of liquid water at 11.16 eV (vertical transition energy). The photoionization threshold energy of liquid water determined in the present study is 9.9 eV. In analogy to the procedure used earlier by Delahay et al.<sup>128</sup> in threshold appearance potential measurements, the threshold energy is

obtained by a linear extrapolation of the low-energy wing of the  $1b_1$  photoelectron peak (see inset of Figure 21). It is slightly lower than the reported value of 10.06 eV.<sup>128</sup> Differences between the values for liquid water reported here and the values for  $1b_1$ ,  $3a_1$ , and  $1b_2$  obtained in the earlier HeI study<sup>131</sup> can be attributed to the improved counting statistics obtained by using high-brilliance synchrotron radiation and to the reduced secondary electron background in the present experiment, which uses higher photon energies.

The observed liquid-to-gas-phase peak shifts for liquid water are the net result of at least three contributions: surface dipoles, electronic polarization, and changes in the orbital structure due to hydrogen bonding. The first effect is small because the surface dipole moment arising from oriented water molecules at the liquid surface is small, some 10 mV<sup>272</sup> (see section 2.1); according to eq 3.3, surface dipoles can cause shifts in the PE spectrum. The screening contribution to the observed shift can be quantitatively estimated from the Gibbs free energy of solvation, given by the Born equation<sup>121,187,273</sup>

$$\Delta G^{\text{thermo}} = -(e^2 q^2 / 8\pi\epsilon_0 R)(1 - 1/\epsilon) = E_g - E_{\text{aq}} \quad (5.1)$$

where  $E_{\text{aq}}$  and  $E_g$  denote the aqueous and gas-phase binding energies, respectively. Because the photoemission process occurs on the femtosecond time scale, the solvent water molecules have no time to reorientate around the charge. Thus,  $\epsilon$  can be identified with the optical macroscopic relative permittivity of water,  $\epsilon_{\text{opt}} \approx 1.8$ .<sup>274</sup>  $R$  can be identified with the first maximum of the oxygen–oxygen radial distribution function or with an effective solute cavity radius,  $R_{\text{eff}}$ . Using  $R_{\text{eff}} = 2.24 \text{ \AA}$ ,<sup>169</sup> one obtains  $-\Delta G = 1.4 \text{ eV}$ , in good agreement with experiment. Notice, however, that the value of the radius is considerably model-dependent, and one should also account for the much smaller stabilization energy of the neutral species as well. This term would correspond to the condensation of water vapor into the liquid, yielding  $\Delta G_{\text{neutral}} = -0.27 \text{ eV}$  ( $-6.3 \text{ kcal/mol}$ ).<sup>275</sup> In this simple macroscopic consideration of solvation, microscopic details are fully neglected, and hence, the more interesting question that arises is whether the quantitative effect of hydrogen bonding on the  $\text{H}_2\text{O}$  orbital structure and energies can be inferred. This information, indeed, appears to be contained in the present PE spectra, leading to the observed small differences in the gas–liquid peak shifts for the individual valence orbitals. However, at the present moment, experimental quantification of this effect is not possible.

In Figure 22, we compare the measured PE spectrum from liquid water and a theoretical density of states of liquid water, computed from state-of-the-art *ab initio* molecular dynamics trajectory calculation, and analyzed in terms of interaction between the molecular orbitals localized on single water molecules.<sup>276</sup> This comparison shows considerable inconsistency regarding the orbital energies. First, the calculated density spectrum in Figure 22 had to be blue-shifted by 3 eV to show overlap with the  $1b_1$  ( $1B_1$  in the notation of ref 276) orbital energy (which was arbitrarily chosen for reference). Second, the relative orbital energies also differ considerably. The considerable underestimation of ionization energies in density functional theory (DFT)<sup>94</sup> can be attributed to the fact that orbitals are only auxiliary tools in DFT and their energies strongly depend on the particular use of the exchange–correlation functional. Even for Hartree–Fock-based methods, it is known that the use of Koopman’s

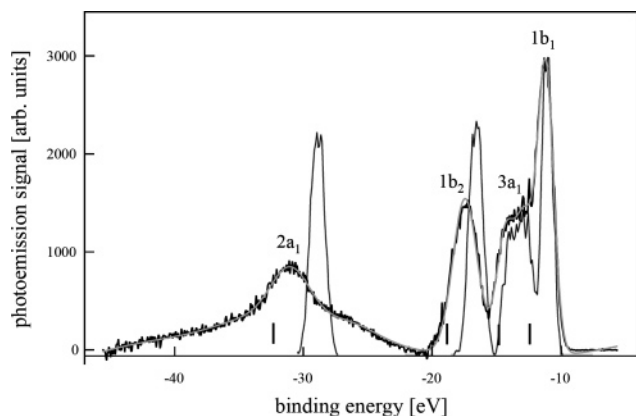


**Figure 22.** Experimental photoemission spectrum from liquid water (and fit) compared to total density of occupied one-electron states for liquid water from ab initio molecular dynamics trajectories, based on density functional theory; adapted from ref 276 with permission from Elsevier. The energies of the density distributions were shifted by 3 eV toward higher binding energies to match the experimental  $1b_1$  energy, measured in photoemission. The bars mark the center positions of the  $H_2O$  gas-phase orbital energies.

theorem leads to errors in estimates of ionization potentials on the order of 1 eV, because of imperfect cancellation of orbital relaxation and correlation effects. For DFT methods, such as those based on the BLYP functional<sup>94</sup> and typically used in ab initio molecular dynamics, the error, however, is much larger. Yet, it is perhaps still interesting to note that the  $2a_1$  orbital ( $1A_1$  in ref 276), for which the largest PE peak shift with respect to the gas-phase energy is observed, also exhibits the largest relative shift with respect to the calculated peak of the density of the  $2a_1$  orbital.

The peak broadening in the liquid phase is reasonably well reproduced in the calculations, with an underestimation of the experimental widths by 50%. It is gratifying to note, however, that the integrated calculated valence-state density and the PE total signal intensities agree to within 20%. This can be directly seen from Figure 22, and it is particularly clear for the  $1b_1$  and  $3a_1$  orbitals. The deviation of calculated orbital energies, on the order of 0.5–1 eV, was interpreted as arising from both thermal and electronic broadening, with the electronic interaction dominating, and the strong overlap of band densities of the three interacting orbitals  $1b_1$ ,  $3a_1$ , and  $2b_1$  has been pointed out to be indicative of orbital interactions in hydrogen-bonded systems.<sup>276</sup> A thorough discussion of the nature of hydrogen bonding, though in *ice*, in terms of charge transfer between the oxygen lone pair and the antibonding orbitals on neighboring water molecules, based on XAS and XES studies in combination with DFT, can be found in a recent paper by Nilsson.<sup>277</sup> Clearly, in view of the poor agreement between experiment and theory in Figure 22, theoretical models need considerable improvement. It will probably be necessary to evaluate state energies rather than orbital energies (relying on Koopman's theorem), even though this might necessitate further approximations in the treatment of the solvent.

Qualitatively, the peak broadening observed in the liquid phase, can also be related to the statistical distribution of H-bonding configurations or to the ratio of broken vs unbroken hydrogen bonds, including surface vs bulk water, as discussed by Wernet et al.<sup>92</sup> Peak broadening has been also discussed by Guo et al.,<sup>156</sup> who performed X-ray emission spectroscopy experiments (XES) on liquid water. In supporting MD simulations, considerable energy level

splitting was found resulting from the interaction with the orbitals of the surrounding molecules, and strong involvement of  $a_1$ -symmetry valence orbitals in hydrogen bonding was observed. The  $3a_1$  broadening, specifically, was attributed to an increase in the dipole moment of liquid water<sup>278,279</sup> and subsequent polarization and hybridization of the orbital. We notice that, also in the PE spectra, the  $3a_1$  feature is considerably broadened as compared to the gas phase.<sup>269</sup> Similar  $3a_1$  peak broadening was observed in the PE spectra of ice, which in the older literature, was assigned to Davydov level splitting.<sup>280</sup> In a most recent PE study from ice, combined with DFT,<sup>277</sup> the  $3a_1$  splitting could be clearly resolved when 530 eV photons were used (because of the large O 2s cross section), but could not be resolved for 100 eV photons. The origin of splitting was also concluded to arise from the symmetry of the crystal lattice where the unit cell of ice contains two water molecules, thus leading to two  $3a_1$  bands (see also ref 280). It is important to notice, however, that the same explanation would not hold to account for the similarly large  $3a_1$  width observed in the PE spectrum of liquid water, which we have, in fact, confirmed in our preliminary PE studies at extended photon energies. Early photoemission spectra of ice were reported in refs 280–283, and a comparison with the present PE data for liquid water is given in ref 269.

### 5.1.3. Relative Photoionization Cross Sections

The effect of hydrogen bonding on the electronic structure of  $H_2O$  orbitals in the liquid phase can also be revealed in the differential photoionization cross sections,  $d\sigma_i/d\Omega$ . This is possible because changes in the molecular orbitals will also change the interference structures between the respective partial waves, and hence, the  $\beta$  factor (see section 3.1) will change relative to the gas-phase value. In the present series of experiments, the electron emission signal was fixed at  $90^\circ$ , and  $\beta$  had significant influence on the observed differential cross sections. Experimental  $d\sigma_i/d\Omega_\perp$  values, at  $90^\circ$ , are presented in Figure 23 for the four outer orbitals of

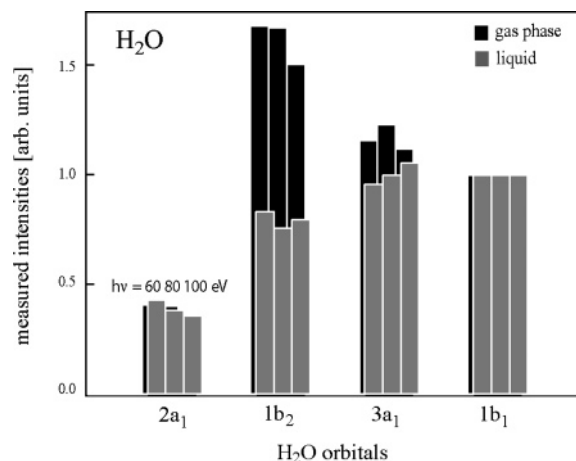


**Figure 23.** Measured differential partial photoionization cross sections,  $d\sigma_i/d\Omega$ , of the four  $H_2O$  outer orbitals in the liquid and gas phase, obtained for 60, 80, and 100 eV excitation photon energies, at normal detection. Data are normalized to the  $1b_1$  value. Reprinted with permission from ref 269. Copyright 2004, American Chemical Society.

liquid water, obtained for three different photon energies of 60, 80, and 100 eV. The data are normalized to the  $1b_1$  intensity, and for comparison, the respective gas-phase cross sections are also shown in the figure. The normalization to

the  $1b_1$  gas-phase peak is somewhat arbitrary. However, normalization with respect to the  $1b_2$  intensity (or any other) would imply changes of all other orbitals and would seem less natural. As can be seen in Figure 23, there is no significant dependence on the photon energy, which indicates that final-state effects play a small role, if any. For cross-checking, it was verified that the evaluated relative partial cross sections,  $\sigma_i$ , for the gas-phase data in Figure 23 and eq 3.4 are in excellent agreement with the respective values reported in the literature.<sup>237</sup> Unfortunately, the analogous evaluation for liquid water cannot be done because the literature  $\beta$  values for the liquid are not available and could not be measured here simultaneously.

The most noticeable observation from Figure 23 is the approximately 50% smaller differential partial cross section of the liquid water  $1b_2$  orbital as compared to the gas phase orbital. A smaller decrease, by about 10%, occurs for  $d\sigma_{3a_1}/d\Omega$  for liquid water. We must speculate, however, on whether the strong effect for the  $1b_2$  orbital can be attributed exclusively to hydrogen bonding. It could as well originate, in part, from surface molecule alignment effects. Moreover, the differences observed in Figure 23 do not necessarily arise from changes of the total photoemission cross section alone; one might also have to consider the possibility of  $\beta$  changes, which, in fact, might be more important, because the asymmetry parameter depends primarily on the phase shifts of the outgoing partial electron waves. Clarification of this issue would require accurate calculations or measurements of  $\beta_i$  values. As long as these are not available, it is perhaps illustrative to use eq 3.4 for the formal determination of  $\beta_{1b_2}$  (and using the gas-phase  $\beta$  values for the other three orbitals, with average values near 1.5 for these symmetries) such that the difference in Figure 23 between the gas phase and the liquid phase vanishes. If  $\beta_{1b_2}$  is arbitrarily corrected from its gas-phase value of 1.1<sup>237</sup> to about 1.5, identical  $\sigma$  plots are obtained for the liquid- and gas-phase relative cross sections. The  $H_2O$  gas-phase  $1b_2$  orbital is localized along the O—H bond, which is held responsible for the comparably small  $\beta_{1b_2}$  value. Hence, one might argue that the strong bonding character of the  $1b_2$  orbital is counterbalanced in the presence of hydrogen bonding, causing a more isotropic distribution of electron charge around the oxygen atom.<sup>284</sup> As already mentioned, having performed the experiment at one single detection angle, we cannot exclude the possibility that water surface orientational effects contribute to the observed relative intensity changes. A discussion of angle-resolved PE as a tool for obtaining structural information of adsorbates on solid surfaces can be found in refs 224 and 285. For the cylindrical liquid jet, however, these effects are likely to largely cancel given that the emission signal is an average over emission angles, as illustrated in Figure 15. Notice, also, that meaningful angle-resolved studies would be performed by variation of the emission angle along the jet propagation direction.

## 5.2. Aqueous Solutions: Electron Binding Energies and Structure

### 5.2.1. Simple Alkali Halide Salts

In this section, PE spectra from aqueous alkali halide solutions are presented. Salt concentrations are in the 1 molar (1 M) range. This is far above the Debye–Hückel regime (ca.  $10^{-3}$  M<sup>286</sup>), and hence, ions are no longer perfectly separated. Strong electrolytes are not yet well understood,<sup>189</sup>

and one has to rely on model simulations,<sup>30,31,172,173</sup> or on very few atomistic ND experiments on radial density functions of aqueous solutions,<sup>54</sup> and on ultrafast IR vibration relaxation studies of hydrogen-bond disruption in alkali halide salt solutions.<sup>73,287</sup>

In the quite complementary PE studies presented here, the measured electron binding energies of the aqueous ions are compared with predictions of theoretical models, and we discuss the information the PE spectra contain regarding molecular details of the solution–vacuum interface. The PE spectra in Figure 24, obtained at 100 eV, contrast aqueous

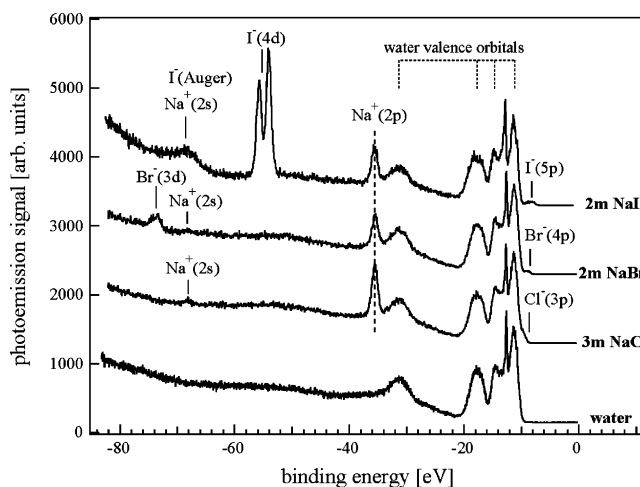


**Figure 24.** Photoemission spectra of pure liquid water and 3 *m* NaCl, 2 *m* NaBr, and 2 *m* NaI aqueous solutions, obtained for 100 eV photon energy. Electron binding energies are given with respect to the vacuum level, and the intensities are normalized to the synchrotron photon flux. Ion and water features are assigned. Reprinted with permission from ref 271. Copyright 2005, American Chemical Society.

sodium halide solutions for different anions, namely, 2 molal (*m*) NaI, 2 *m* NaBr, and 3 *m* NaCl, and of pure liquid water for comparison. The intensities were normalized to the liquid  $H_2O$   $1b_1$  emission signal, and traces are vertically displaced for clarity. Electron binding energies are presented relative to vacuum. The characteristic emission from the liquid–water valence orbitals (marked in the top panel) continues to be seen at the identical energies in the solution spectra. Emission from aqueous sodium ion is observed at 68.0 and 35.4 eV electron binding energies,  $E_{aq}^{PES}$ , for  $Na^+(2s)$  and  $Na^+(2p)$ , respectively. Some iodide Auger contribution overlaps with the  $Na^+(2s)$  feature. The Auger process is assigned to filling the  $I^-(4d)$  hole by a  $I^-(5p)$  electron and simultaneous emission of a 5p electron leading to a two-hole final state ( $4d-5p5p$ ). The large  $I^-(4d)$  signal intensity is due to a shape resonance peaking near 100 eV excitation energy. Observed sodium binding energies are found to be independent of the counteranion. Below, when presenting the concentration dependence for NaI solutions, we see that the concentration variation also has no noticeable effect on the measured peak positions of the aqueous ions. The energies of the aqueous anions in Figure 24 are 9.6 (8.7) eV [ $Cl^-(3p)$ ], 8.8 (8.1) eV [ $Br^-(4p)$ ], 73.2/74.3 eV [ $Br^-(3d)$ ], 7.7/8.8 (7.3) eV [ $I^-(5p)$ ], and 53.8/55.5 eV [ $I^-(4d)$ ], where the pairs of values correspond to different spin–orbit states. The threshold energies of the anions (given in parentheses), obtained by linear extrapolation of the low-binding-energy edge of the spectra, agree well with previous reports on threshold measurements:<sup>288</sup> 8.77, 7.95, and 7.21 eV for  $Cl^-(3p)$ ,  $Br^-(4p)$ , and  $I^-(5p)$ , respectively.



As another example, PE spectra from 2–3 *m* aqueous solutions of alkali iodide, are presented in Figure 25. For

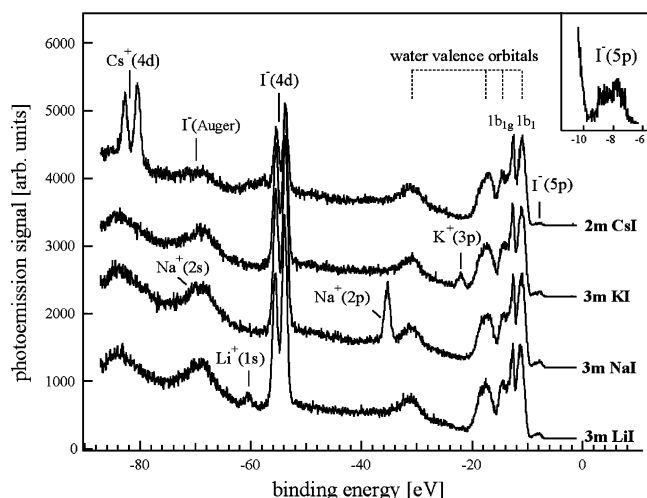


**Figure 25.** Photoemission spectra of aqueous alkali halide solutions, LiI, NaI, KI, and CsI, obtained for 100 eV photon energy. Molal concentrations are indicated, and the characteristic emission of atomic ions is labeled. Energies are with respect to vacuum. The inset is an enlargement of the emission onset. Reprinted with permission from ref 271. Copyright 2005, American Chemical Society.

aqueous  $\text{Li}^+$ , only the  $\text{Li}^+(1s)$  line at 64.4 eV is observed. Two features are seen for aqueous  $\text{K}^+$ , the  $\text{K}^+(3p)$  emission at 22.2 eV and a very weak  $\text{K}^+(3s)$  emission at 38 eV.  $\text{Cs}^+$  again exhibits only one distinct feature, an intense doublet at 80.6/82.9 eV, arising from  $\text{Cs}^+(4d)$  emission. This peak is nearly as intense as the  $\text{I}^-(4d)$  peak. In addition, cesium Auger emission,  $\text{Cs}(4d-5p5p)$ , gives rise to the small feature near 58 eV, which is barely seen underneath the  $\text{I}^-(4d)$  signal in Figure 25. No  $\text{Cs}^+(5p)$  or  $\text{Cs}^+(5s)$  signal is found in our spectra because of the expected spectral overlap with the water valence features and also because of low photoionization cross sections. In fact, the neutral gas-phase alkali atoms  $\text{Cs}(5p)$  and  $\text{Cs}(5s)$  have the lowest photoionization cross sections, lower than that of  $\text{K}(3s)$ , at 100 eV.<sup>289</sup> Also, no counteranion dependence on the electron binding energies is observed in Figure 25, within the experimental error of about 0.05 eV. Similar series of PE spectra were measured for other anion/cation combinations, all exhibiting the same notable insensitivity of the electron binding energy to the counterion and to the concentration of the solute. This applies for the entire range of concentrations measured here, i.e., from the detection limit of 0.1 *m* solutions to the highest concentrations, near the molar saturation limit.

Apparently, the perturbation of the water valence orbitals by dissolved ions is negligibly small. A similar insensitivity to the salt environment has been observed in the electron detachment dynamics from anions where the detached electron remains trapped in the liquid phase.<sup>46</sup> Contrary to expectations based on the Debye–Hückel picture, significant effects are only observed when the salt concentration approaches 5 *m*.<sup>46</sup> Tables 2 and 3 summarize the experimental electron binding energies ( $E_{\text{aq}}^{\text{PES}}$ ) and peak widths ( $\text{fwhm}_{\text{aq}}^{\text{PES}}$ ) from all of these measurements. The use of different photon energies (whenever appropriate), namely, 60, 80, and 100 eV, was found to have no effect on the values included in the tables.

A remaining issue is the sensitivity of the valence-electron binding energies of the ions to their location in the surface

**Table 2. Measured Electron Binding Energies ( $E_{\text{aq}}^{\text{PES}}$ ) and Peak Widths (fwhm) of Aqueous Cations<sup>a</sup>**

cation		$E_{\text{g}}(\text{M}^+)$ (eV)	$E_{\text{aq}}^{\text{PES}}(\text{M}^+)$ (eV)	$\text{fwhm}_{\text{aq}}$ (eV)
Li	1s	75.64 <sup>a</sup>	60.4 ± 0.07	1.4 ± 0.20
Na	2p	47.28 <sup>a</sup>	35.4 ± 0.04	1.1 ± 0.03
		47.45 <sup>a</sup>		
	2s	80.07 <sup>a</sup>	68.0 ± 0.15	3.1 ± 0.50
K	3p	31.62 <sup>a</sup>	22.2 ± 0.06	1.4 ± 0.20
		31.89 <sup>a</sup>		
	3s	47.81 <sup>a</sup>	~38	
Rb	4p	27.29 <sup>a</sup>	<i>d</i>	
Cs	5p	23.14 <sup>b</sup>	<i>d</i>	<i>d</i>
	5s	38.98 <sup>c</sup>	<i>d</i>	<i>d</i>
	4d <sub>5/2</sub>	88.55 <sup>b</sup>	80.6 ± 0.08	1.1 ± 0.05
	4d <sub>3/2</sub>		82.9 ± 0.04	1.3 ± 0.06

<sup>a</sup> For comparison, the ionization energies ( $E_{\text{g}}$ ) of the corresponding gas-phase cations are shown. From Winter et al.<sup>271</sup> <sup>a</sup> From ref 245. <sup>b</sup> From ref 299. <sup>c</sup> From sum of atomic transition line (ref 245) and gas-phase electron affinity (ref 299). <sup>d</sup> Not observed.

**Table 3. Measured Electron Binding Energies ( $E_{\text{aq}}^{\text{PES}}$ ) and Peak Widths (fwhm) of Aqueous Anions<sup>a</sup>**

anion		$E_{\text{g}}(\text{A}^-)$ (eV)	$E_{\text{aq}}^{\text{PES}}(\text{A}^-)$ (eV)	$\text{fwhm}_{\text{aq}}$ (eV)
F	2p	3.40, <sup>a</sup> 3.45 <sup>b</sup>	8.7, <sup>e</sup> 9.8 <sup>f</sup>	
	2s	24.3 <sup>b</sup>		
Cl	3p	3.61, <sup>a</sup> 3.72 <sup>b</sup>	9.6 ± 0.07 8.7 ± 0.1	0.6 ± 0.20
	3s	no atomic line	<i>g</i>	
Br	4p	3.36, <sup>a</sup> 3.82 <sup>b</sup>	8.8 ± 0.06 8.1 ± 0.1	0.9 ± 0.20
	4s	13.87 <sup>c</sup>	<i>g</i>	
	3d <sub>5/2</sub>	no atomic lines	73.2 ± 0.07	1.2 ± 0.10, 1.1 ± 0.10
	3d <sub>3/2</sub>		74.3 ± 0.09	
I	5p	3.06, <sup>a</sup> 4.00 <sup>b</sup>	7.7 ± 0.20 8.8 ± 0.20 7.3 ± 0.1	0.8 ± 0.30 1.1 ± 0.30
	5s	13.23 <sup>b</sup> (15.10 <sup>d</sup> ) (57.41 <sup>d</sup> )	<i>g</i>	
	4d <sub>5/2</sub>		53.8 ± 0.03	1.0 ± 0.02
	4d <sub>3/2</sub>		55.5 ± 0.03	1.0 ± 0.02

<sup>a</sup> For comparison, the detachment energies ( $E_{\text{g}}$ ) of the corresponding gas-phase anions are shown. From Winter et al.<sup>271</sup> <sup>a</sup> From ref 216. <sup>b</sup> From sum of atomic transition line (ref 300) and gas-phase electron affinity (ref 216). <sup>c</sup> From sum of atomic transition line (ref 245) and gas-phase electron affinity (ref 216). <sup>d</sup> From LDA calculations in ref 301. <sup>e</sup> From ref 133. <sup>f</sup> Estimated from ref 119. <sup>d</sup> Not observed.

or bulk. Can one, for instance, distinguish between bulk and surface anion solvation? The photoelectron spectroscopy apparatus, as currently configured, samples both bulk and interfacial anions. Hence, the peak in the photoelectron spectrum would likely be an average of the two. It seems, though, that the effect is very small. For the large and polarizable iodide, for instance, no PE peak differences were detected between iodide measured in NaI and *surface-active* tetrabutylammonium iodide (TBAI) aqueous solution. In the latter case, a single segregation surface layer is formed, with both anions and cations residing in the solution surface only. Thus, as opposed to simple salt solutions, the iodide signal is sampled primarily from the very interface (see section 5.2.2). Also, previous calculations combining equilibrium classical molecular dynamics simulations and *ab initio* calculations show that the vertical detachment energies (VDEs) for iodide in the aqueous bulk and at the surface differ by less than 0.1 eV.<sup>174</sup> Furthermore, given the larger propensity for the larger anions to exist at the surface, any

hypothetical differences between calculated (see below) and experimental energies would be expected to be smallest for iodide, which is not the case.<sup>271</sup> Notice that, by the same argument, the distinction between surface and bulk solvation contributions to the energies of aqueous cations would seem irrelevant.

A graphical depiction of the lowest electron binding energies,  $E_{\text{aq}}^{\text{PES}}$ , for each aqueous ion (from Tables 2 and 3) is given in Figures 26 and 27 for cations and anions,

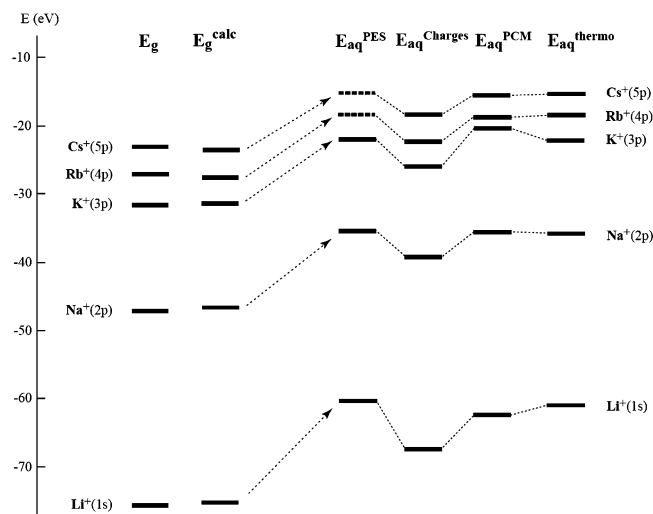


**Figure 26.** Diagram of lowest electron binding energies of aqueous cations, comparing experimental,  $E_{\text{aq}}^{\text{PES}}$ , and calculated values. For the calculations, different models were used, yielding  $E_{\text{aq}}^{\text{charges}}$ ,  $E_{\text{aq}}^{\text{PCM}}$ , and  $E_{\text{aq}}^{\text{thermo}}$ . For comparison, experimental and calculated energies of the respective gas-phase cations,  $E_{\text{g}}$  and  $E_{\text{g}}^{\text{calc}}$ , are shown as well. No accurate experimental  $E_{\text{aq}}^{\text{PES}}$  values could be obtained for Cs and Rb, as indicated by the dotted lines. The strong energy red shift for aqueous ions is indicated by arrows.  $E_{\text{aq}}^{\text{PES}}$  values are independent of the counterion and of the salt concentration. The calculated energies from adiabatic models,  $E_{\text{aq}}^{\text{PCM}}$  and  $E_{\text{aq}}^{\text{thermo}}$ , fairly accurately reproduce the experimental energies,  $E_{\text{aq}}^{\text{PES}}$ . Reprinted with permission from ref 271. Copyright 2005, American Chemical Society.

respectively. These experimental values are compared to calculated energies,  $E_{\text{aq}}^{\text{charges}}$ ,  $E_{\text{aq}}^{\text{PCM}}$ , and  $E_{\text{aq}}^{\text{thermo}}$ , using various theoretical models.<sup>271</sup> For comparison, experimental and calculated gas-phase values,  $E_{\text{g}}$  and  $E_{\text{g}}^{\text{calc}}$ , are shown as well. Energies  $E_{\text{aq}}^{\text{charges}}$  were obtained from a model that explicitly includes discrete water molecules using a set of snapshots from an equilibrium classical dynamics simulation and a fractional-charge representation of solvent molecules.  $E_{\text{aq}}^{\text{PCM}}$  values were calculated employing a polarizable dielectric continuum model (PCM). Energies for both ground-state cation and dication, or both anion and neutral, were calculated in independently, self-consistently determined spherical cavities with a dielectric constant for the continuum appropriate for water. Therefore, all states are fully relaxed within this model. Finally, use of a thermodynamic cycle treatment in combination with experimental hydration enthalpies yields  $E_{\text{aq}}^{\text{thermo}}$ . Two main observations can be made from the two figures. First,  $E_{\text{aq}}^{\text{PES}}$  for cations is smaller than the respective  $E_{\text{g}}$ , whereas the opposite is true for aqueous anions ( $\text{A}^-$ , Figure 27). That is,  $E_{\text{aq}}^{\text{PES}}(\text{M}^+) < E_{\text{g}}(\text{M}^+)$  and  $E_{\text{aq}}^{\text{PES}}(\text{A}^-) > E_{\text{g}}(\text{A}^-)$ , although the energy difference is considerably larger for cations. Second, the theoretical models nicely reproduce the experimental energies for cations,  $E_{\text{aq}}^{\text{PES}}(\text{M}^+)$ , and the situation for the anions is

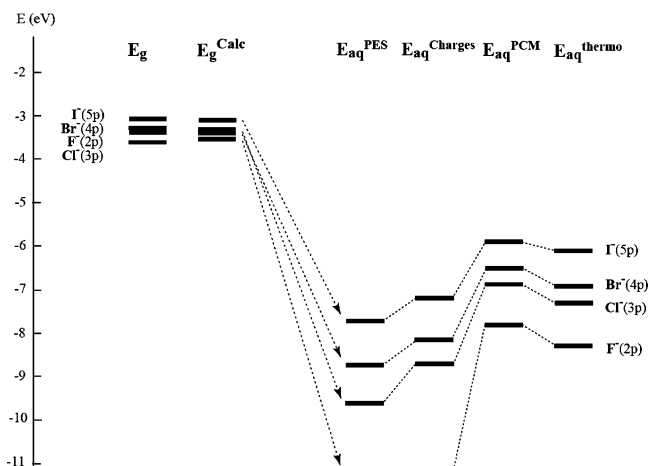


**Figure 27.** Diagram of detachment energies of gas-phase anions ( $E_{\text{g}}$  and  $E_{\text{g}}^{\text{calc}}$ ) and of the respective aqueous anions ( $E_{\text{aq}}$ ).  $E_{\text{aq}}^{\text{PES}}$  is the experimental value, and  $E_{\text{aq}}^{\text{charges}}$ ,  $E_{\text{aq}}^{\text{PCM}}$ , and  $E_{\text{aq}}^{\text{thermo}}$  are calculated energies of the aqueous anions; see text. The dotted line for  $\text{F}^-(2\text{p})$  matches with the respective  $E_{\text{aq}}^{\text{charges}}$  value; the corresponding  $E_{\text{aq}}^{\text{PES}}$  value was not measured here. Arrows indicate the energy blue shift for the aqueous ions. Contrary to the cation case in Figure 26, adiabatic models poorly reproduce experimental energies,  $E_{\text{aq}}^{\text{PES}}$ . Reprinted with permission from ref 271. Copyright 2005, American Chemical Society.

more complicated (see below). The main trend of the gas-to-liquid energy shifts, illustrated by the arrows in Figures 26 and 27, can be understood already from simple continuum model considerations. When treating the photoionization process within a thermodynamic cycle,<sup>290</sup> one can associate the measured energy shift with the difference in  $\Delta G$  for the initial and final states of the solvation complex. This adiabatic ionization estimate,  $E_{\text{aq}}^{\text{thermo}}$ , is then computed as  $E_{\text{g}} - \Delta G^\circ$  for anions and  $E_{\text{g}} + 3\Delta G^\circ$  for cations using experimental solvation free energies. Comparison of  $E_{\text{aq}}^{\text{thermo}}$ , which corresponds to fully relaxed final states, to the experimental  $E_{\text{aq}}^{\text{PES}}$  values should not be realistic given that the time scale of the (vertical) photoionization process is faster than the relaxation of the solvent dipoles (nuclear polarization), which is included in the Born formula (eq 5.1) as well as the relaxation of the electronic polarization. For cations, it turns out that this discrepancy is relatively small, which can be attributed to the favorable preorientation of water molecules around a monocation on vertical transformation to the final states, and the nuclear part of the polarization response is proportionately smaller. This is not true for anionic ionization, however, where the final state is neutral, and considerable nuclear relaxation takes place, so this simple picture is more likely to fail.

As can be seen in Figure 26, both adiabatic models give good results for energies of aqueous cations; the best match with the experiment (within 0.5 eV) is, in fact, always obtained for the simple thermodynamic cycle model. The situation is reversed for aqueous anions; here, the ab initio treatment with explicit charges for the structured solvent shells,  $E_{\text{aq}}^{\text{charges}}$ , agrees best with the experimental energy, but it still underestimates experiment by 0.5–1.0 eV. Results are better for the larger anions. For anions, the  $E_{\text{aq}}^{\text{PCM}}$  and  $E_{\text{aq}}^{\text{thermo}}$  values systematically underestimate the experimental binding energies by 1.5–2.5 eV. Recently, calculations of microsolvated  $\text{Li}^+$  in water, up to  $(\text{H}_2\text{O})_5\text{Li}^+$ , were reported by Cederbaum et al.<sup>112</sup> using ab initio Green's function methods. For five water molecules, the  $\text{Li}(1\text{s})$  ionization energy was found to be 66 eV. This value is about 5.5 eV

higher than for aqueous  $\text{Li}^+$ , measured here (Table 2), and it is almost the same as  $E_{\text{aq}}^{\text{charges}}$ .<sup>271</sup>

Why do the simple Born and PCM models work so well for cations but poorly for anions? Both models provide adiabatic rather than vertical ionization energies. In contrast, the explicit solvent model is vertical with respect to nuclear polarization (the orientation of the waters), so why does it fail for the cation binding energies? Our results indicate that the change from monocation to equilibrium dication is accompanied by only a minor change of water geometry, at least at short range, because the solvent is already favorably preoriented around the cation, and any additional longer-range ordering of the water dipoles in response to the change in charge does not significantly contribute to the energy. On the other hand, the explicit charge model overestimates the electron binding energy, and although relaxation of the water dipoles is properly prohibited, mirroring the instantaneous ionization event, the approach is missing the change in electronic polarization of the water. Water molecules represented as point charges cannot be polarized, and electron-cloud polarization interactions are always stabilizing. The polarization effects are present already for monovalent ions; however, they become particularly strong in the case of multivalent ions. Indeed, the strong electric field of the dication polarizes the surrounding water molecules more than that of the monocation. As a result, the explicit-charge model, which cannot reproduce the differential electronic polarization, tends to overestimate the electron VDE from the alkali cation.

On the contrary, for halide anions, electron detachment results in a significant reorientation of the solvation shell; water molecules prefer to point with hydrogen atoms toward the anion but with oxygen atoms toward neutral halogen atoms. In addition, there is a smaller change in the electronic polarization of the surrounding water by the formation of the neutral halogen atom. Therefore, for the anions, it is more important to have a vertical treatment of the nuclear polarization, which also rationalizes the poor performance of adiabatic continuum models. A more detailed discussion of how the energies and peak widths were extracted is presented in refs 271 and 290.

Finally, it is interesting to compare the vertical energies reported here to the energy diagram for liquid water when its electronic structure is treated within the formalism of solid-state physics.<sup>199,291</sup> The magnitude of the band gap for liquid water has long been controversial,<sup>45,291</sup> but the value for the vertical ionization energy from liquid water from the liquid photoelectron spectrum<sup>131,269</sup> has helped to clarify the different energetic contributions to the adiabatic band gap.<sup>199</sup> One can regard the anions and cations in solution as defects in a liquid insulator. The anions provide for midgap states, whereas the highest occupied orbital of each cation lies deeper than the valence band of water. The position of the aqueous halide anions on the band diagram for water has been discussed in detail in refs 199 and 292. The current work provides accurate vertical detachment energies (VDEs) in that endeavor. Further, comparison of the vertical energy required to detach a valence electron to vacuum with the energy required to promote the same electron to the polarization-bound CTTS state is highly valuable, as the two are expected to be correlated. We expect that knowledge of the VDE for anions where CTTS assignments (e.g.,  $\text{F}^-$ ,  $\text{NO}_3^-$ ) have not been hitherto made will be particularly useful.

The PE spectral evolution as a function of solution concentration for 0.5–12 *m* NaI aqueous solutions (saturation is 13 *m*) is shown in Figure 28. The intensities are scaled to

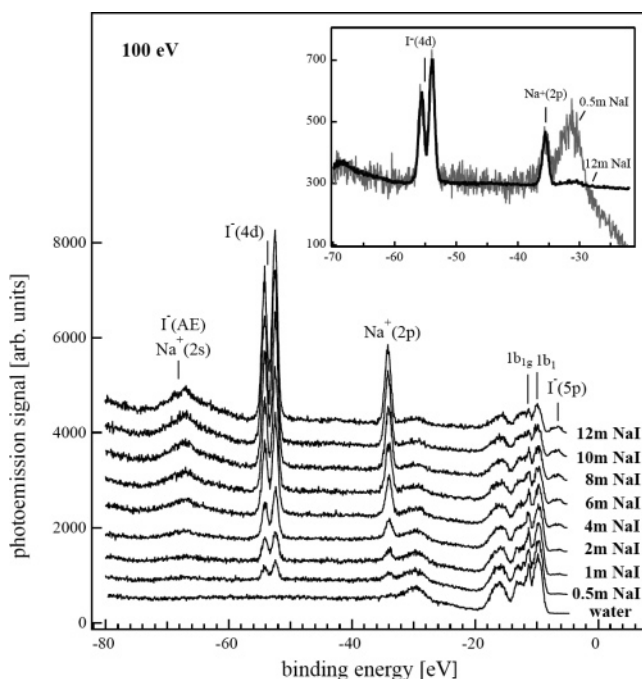


**Figure 28.** Photoemission spectra of NaI aqueous solutions having different concentrations, 0.5–12 *m*, obtained for 100 eV excitation photon energy. Intensities are normalized to the synchrotron photon flux. Electron binding energies of both anions and cations are independent of salt concentration as seen from the comparison of the PE spectra of the solutions of lowest and highest salt concentration, shown in the inset. Reprinted with permission from ref 290. Copyright 2004, American Chemical Society.

the synchrotron ring current, and the spectra thus reveal the actual relative intensity changes upon concentration variation. In using 100 eV photons, we have taken advantage of the enhanced photoionization cross section of  $\text{I}^-(4d)$  due to a shape resonance, as well as the fact that, at this photon energy the iodide can be probed at maximum surface sensitivity (see section 3.2).

As can be seen in Figure 28, the ion signal steadily increases with concentration. At the same time, the water (absolute) signal decreases as water molecules are being replaced by ions. The spectra do not exhibit energy shifts (within  $\pm 30$  meV) of any ion or water feature over the entire concentration range, covering two orders of magnitude. In view of the considerable structural changes of the solvation structure that must occur when approaching saturation (where the water-to-salt ratio is only 5:1), constant energies seem surprising. Similarly, surface and bulk solvated iodide cannot be distinguished by the measured energies, as discussed above. To illustrate the signal evolution quantitatively, of measured photoemission intensities of  $\text{I}^-(4d)$  and the  $\text{Na}^+(2p)$  are presented in Figure 29, as a function of the salt concentration. The signal rises linearly up to 2 *m* and increases sublinearly for higher concentrations. This behavior, which is identical for anions and cations, can be interpreted in terms of a slower increase of the ion concentration in the interfacial region than in the bulk (which is actually the classical picture of the interface being depleted of ions). However, whether the expected anion surface enhancement occurs can be neither confirmed nor excluded from these PE data. The main obstacle in analyzing the present PE data



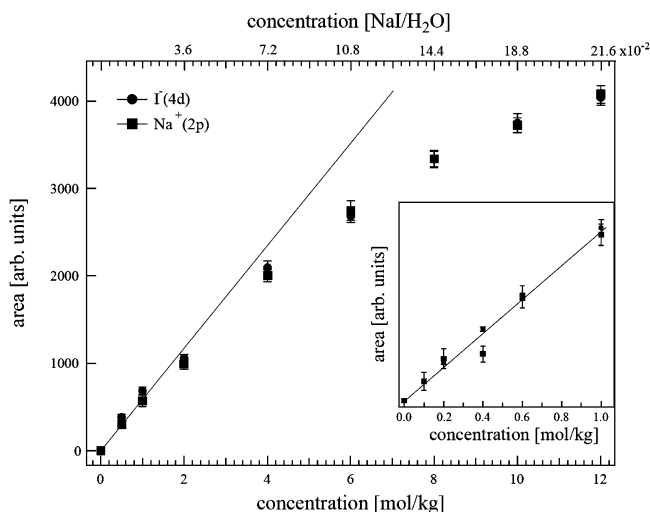


**Figure 29.**  $\text{I}^{-}(4d)$  and  $\text{Na}^{+}(2p)$  photoemission signal intensity vs concentration of aqueous NaI solution. Results for the higher concentrations, up to 12 *m*, are shown in the main plot, and lower concentration data, 0.1–1.0 *m*, are shown in the inset. Anions and cations exhibit identical signal behaviors. Reprinted with permission from ref 290. Copyright 2004, American Chemical Society.

is the uncertainty of the experimental probing depth as was mentioned in section 3.2. We would expect about 30% surface contribution to our spectra for the photon energy used. In addition, for the present case, the kinetic energies of electrons emerging from  $\text{Na}^{+}(2p)$  and  $\text{I}^{-}(4d)$  are both within the minimum of the electron IMFP curve (Figure 14), and hence, either species is being probed within nearly the same depth. Even though this depth is small, it is apparently not small enough that relative intensity changes between anions and cations would be resolved, ca. 3–4 Å (see Figure 6). It might be possible in future experiments to resolve small chemical shifts between surface and bulk solvated ions. Using a wide range of photon energies, approximately 1000–1500 eV, the probing depth can be systematically varied.

With the above-mentioned VSFS and SHG experiments, a different problem is encountered in extracting convincing evidence for the enrichment of anions at the aqueous surface. Despite the exclusive surface sensitivity of these techniques, the nonlinear optical signal is sampled from a region within which the symmetry is broken, but the ion distribution within this layer cannot be localized exactly. Currently, this missing information has to be provided by theory. For a qualitative discussion, though, it might be instructive to compare the Langmuir analysis, as applied by Saykally et al.,<sup>27</sup> for the two sets of data (SHG and PES) from aqueous NaI solution. Figure 30 shows the resulting plot of the  $\text{I}^{-}(4d)$  signal measured in the photoemission experiment; the data were taken from Figure 28. Contrary to the corresponding plot for the iodide SHG signal dependence on concentration,<sup>27</sup> already shown in Figure 8, Figure 30 displays the reciprocal of eq 2.7, with substitution of  $y = 1/\Theta$  and  $x = 1/c$ , yielding a linear expression in  $y$

$$y = K^{-1} + (55.5 \text{ M}) \exp(\Delta G_{\text{ads}}/RT) K^{-1} x \quad (5.2)$$

From Figure 29, one derives  $\Delta G_{\text{ads}} = -1.7 \pm 0.2$  kcal/mol, which is more than a factor of 3 smaller than the  $-6.1$  eV value obtained from the SHG analysis,<sup>27</sup> but it is quite close to the  $\Delta G_{\text{ads}} = -0.8$  kcal/mol value found in MD simulations.<sup>31</sup> Qualitatively, the larger negative  $\Delta G_{\text{ads}}$  value in the PE experiment can be attributed to the larger probing range,

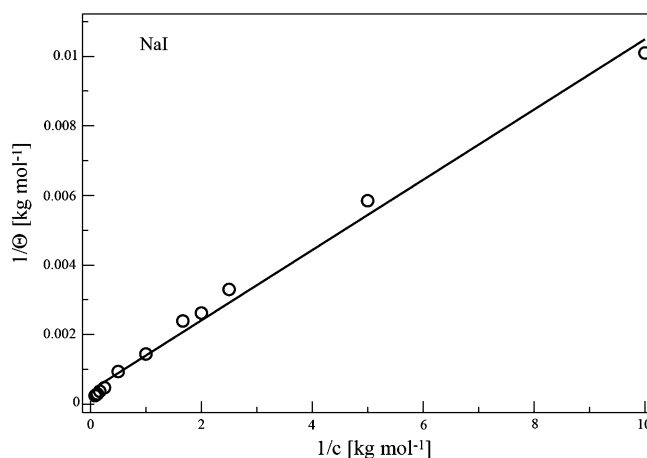


**Figure 30.** NaI aqueous solution:  $\text{I}^{-}(4d)$  intensities vs concentration data (from Figure 29) fitted to eq 5.2, which is the reciprocal of the usual expression of the Langmuir isotherm model. From the slope, one obtains  $\Delta G_{\text{ads}} = -1.7 \pm 0.2$  kcal/mol for iodide in NaI aqueous solution. The identical fit is obtained for the  $\text{Na}^{+}(2p)$  signal. The regression equation is  $y = (4 \pm 1) \times 10^{-4} + x(101 \pm 3) \times 10^{-5}$ .

so that bulk signal contributions are contained in the PE case. An interesting observation from the PE experiment is that both anions and cations exhibit the exact same concentration dependence (Figure 29); notice that the  $\text{Na}^{+}$  cation signal is not accessible in the resonant SHG study. This behavior can be explained by the very small spatial separation of anions and cations, about 3 Å (as shown in Figure 6), which is less than the photoemission probing depth. Hence, the same value for the adsorption free energy must be obtained in the PE analysis of the two ions, which is the case. This shows that there is indeed some qualitative value in examining the Langmuir isotherm analysis on the basis measured ion intensities. However, the fact that the weighting of the measured intensities with respect to the true location of the maximum ion distribution is not experimentally determined leads to quite different values of  $\Delta G_{\text{ads}}$ . One way to obtain PE signal specifically from the surface is to study iodide in the presence of a surfactant, which is the topic of the next section.

### 5.2.2. Surfactants

In contrast to the mechanism that drives polarizable halide anions to the surface, the adsorption of surfactants at aqueous interfaces is due to hydrophobic interactions. Hence, surface-active salts such as tetrabutylammonium iodide (TBAI; a schematic of the molecule is shown in Figure 32), containing hydrophobic hydrocarbon chains, are interesting systems for studying charge solvation at the interface. TBAI is, in fact, one of the most efficient and intensively investigated phase-transfer catalysts,<sup>125</sup> and it is important to understand, for instance, the distribution of anions and cations at the interface, as well as the structure of the hydrogen-bonding network at the interface. In formamide, TBAI salt forms a surface monolayer of about 1 nm thickness, which is roughly the size of the  $\text{TBA}^{+}$  cation. The surface profile, as inferred from angle-resolved PE measurements,<sup>124</sup> was already shown in Figure 2. The present PE studies of TBAI aqueous solutions, complemented by MD simulations,<sup>293,294</sup> are aimed at a better understanding of the structural details of the solution interface, including the segregation of iodide interacting with the surface segregation layer. Furthermore, a comparative study of TBAI vs TBABr is presented, which

provides information on the competition between the larger iodide and the smaller bromide in occupying surface sites (and on the consequences for the structure of the segregation surface layer).

Figure 31 demonstrates the surface activity of TBAI by comparing the PE spectra from a 2 *m* NaI aqueous solution

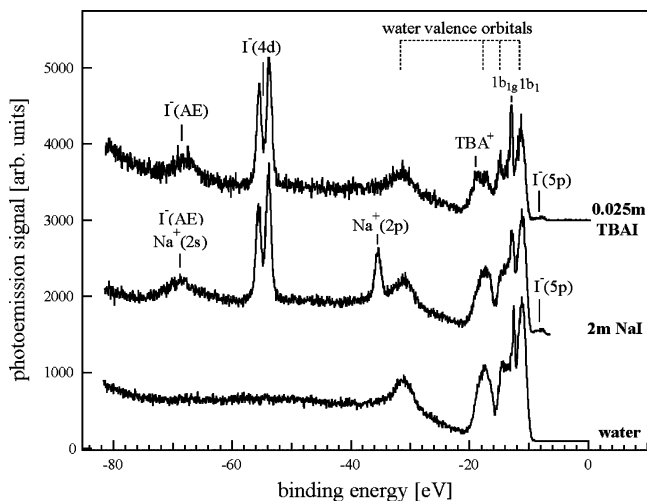


**Figure 31.** Photoemission spectra of (bottom) liquid water, and (middle) 2 *m* NaI and (top) 0.025 *m* TBAI aqueous solutions measured at 100 eV photon energy. Ion emission is labeled. Electron binding energies are relative to vacuum, and intensities are normalized to the electron ring current. Nearly identical iodide signals are observed for the two salt solutions, even though the concentration of the surfactant is a factor 80 lower. Energy differences of  $I^{-}(4d)$  peak positions for the two solutions are not observed. Reprinted with permission from ref 294. Copyright 2004, American Chemical Society.

and 0.025 *m* TBAI aqueous solution. For reference, the pure-water PE spectrum is shown as well; all spectra were measured at 100 eV photon energy. As before, intensities are scaled to the synchrotron flux, which allows for a quantitative comparison of signal. Despite the 80-times lower concentration, the TBAI spectrum yields the same iodide,  $I^{-}(4d)$ , intensity as seen in the NaI spectrum. One can also observe the intensity decrease of the water features due to the attenuation of the water signal for the solution. Signal from the  $TBA^{+}$  cation can be barely identified in the spectra because of the low photoionization cross sections of carbon and nitrogen; the only noticeable peak arising near 19 eV strongly overlaps with the water features. However, for charge neutrality, equal amounts of anions and cations must exist at the surface. Given the  $I^{-}(4d)$  iodide signal ratio of  $I^{-}(TBAI)/I^{-}(NaI) = 0.9$  (Figure 28) and the corresponding iodide concentration ratio of 1/80, we obtain a lower bound on the surface segregation factor of about 70. The actual value will probably be 2–4 times larger because the surface signal in NaI is overestimated.

Figure 32 shows PE spectra from aqueous TBAI solutions as a function of salt concentration in the range 0.005–0.04 *m* (saturation is 0.06 *m*). Intensities in the figure are also scaled to the synchrotron photon flux, and hence, relative intensities quantitatively correlate with the actual density change of ions and waters. As for NaI (see Figure 28), no peak shifts are observed when the TBAI concentration is changed (see vertical lines), and the iodide binding energy is the same (within  $\pm 30$  meV) as in NaI solution. This contrasts a previous photoionization threshold study from aqueous TBAI solutions, where energy shifts on the order

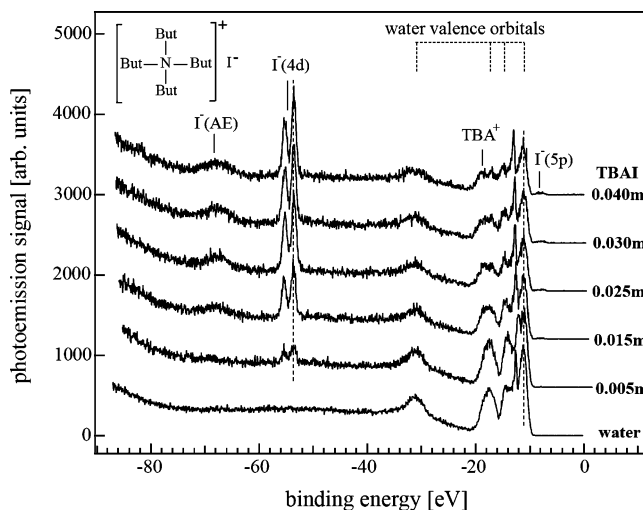


**Figure 32.** Photoemission spectra of TBAI aqueous solutions for different salt concentrations; the photon energy was 100 eV. Intensities in the spectra are normalized to the synchrotron photon flux. Iodide energy shifts as a function of concentration are not observed; the same energy is found for NaI aqueous solutions. A schematic of TBAI is shown on the top. Reprinted with permission from ref 294. Copyright 2004, American Chemical Society.

of  $>0.5$  eV were observed (see Figure 4) and were interpreted in terms of (partial) iodide dehydration at the surface. Arguably, this discrepancy between ref 129 and the present study arises from some spectral (possibly charging) shift, which is probably difficult to take into account in the absence of a well-defined reference energy in the case of threshold studies.

Figure 33 displays the integrated iodide  $I^{-}(4d)$  PE signal (from Figure 32) from aqueous TBAI solutions as a function

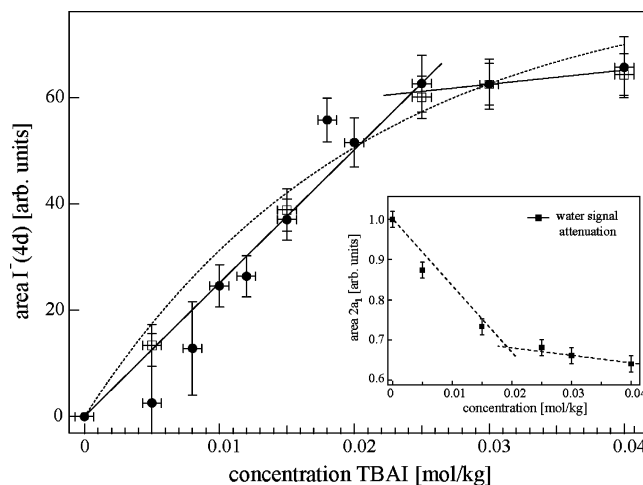


**Figure 33.**  $I^{-}(4d)$  photoemission signal from TBAI aqueous solutions as a function of salt concentration. The symbols refer to two different sets of measurements. The dotted curve is a fit proportional to  $1 - \exp(-c/c_0)$  (see text); the straight lines are guides to the eye. The accompanying change of water attenuation, expressed by the  $2a_1$  signal change, is presented in the inset. Reprinted with permission from ref 294. Copyright 2004, American Chemical Society.

of salt concentration. This plot is analogous to the NaI uptake plot in Figure 29. Qualitatively, two regimes can be distinguished in Figure 33, a linear signal increase as a function of salt concentration, up to ca. 0.02 *m*, and a nearly constant signal above 0.02 *m*. Two lines (solid) have been drawn to guide the eye. The steep increase corresponds to the steady

buildup of the segregation monolayer, whereas the slow intensity increase is attributed, to some degree, to the filling of remaining cavities within the surface layer. Probably, the main signal contribution at high concentration arises from deeper layers, largely reflecting the increase of the bulk ion concentration. Notice that the iodide signal saturation occurs at a much lower salt concentration than in NaI solutions (Figure 29), consistent with Figure 31. The dashed curve in Figure 33 is a  $(1 - e^{-c/c_0})$  fit, commonly used to model layer-by-layer film growth for well-defined adsorbate systems in ultrahigh vacuum.<sup>204,295</sup> This function actually describes the envelope of consecutive linear segments, correlating with the subsequent monolayer built up in growing multilayers. The fit parameter  $c_0 = 0.24$  corresponds to the salt concentration for saturation in the layer-by-layer model. The reason this function fails to describe the TBAI surface adsorption is the above-mentioned fact that only one single monolayer grows, which is accompanied by a small increase of bulk concentration.

A qualitative picture of the surface molecular structure of TBAI, as obtained from MD simulations,<sup>294</sup> is shown in Figure 34. The snapshot displays the surface coverage of 16

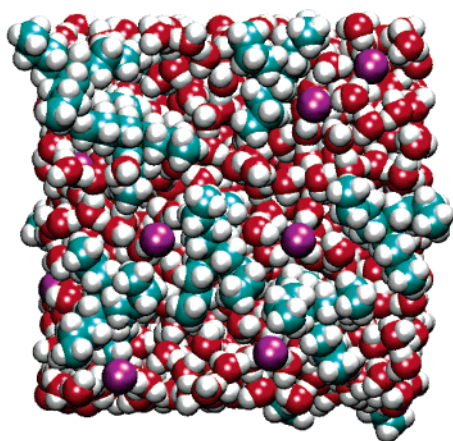


**Figure 34.** Snapshots from molecular dynamics simulations showing the TBAI surface coverage for saturated aqueous solution: 16 TBAI ion pairs. Red represents O atoms, green represents N atoms, white represents H atoms, and purple represents I atoms. Both anions and cations are found at the top surface layer. Reprinted with permission from ref 294. Copyright 2004, American Chemical Society.

TBAI ion pairs (equivalent to about 1 *m* TBAI aqueous solution), corresponding to  $0.9 \times 10^{14}$  TBAI/cm<sup>2</sup>. This is almost the density of the completed surface monolayer ( $1.0 \times 10^{14}$  molecules/cm<sup>2</sup>), as was inferred experimentally.<sup>123</sup> Note that both TBA<sup>+</sup> cations and I<sup>−</sup> anions are present at the surface. Furthermore, the simulations also indicate that any additional cation would be unlikely to fit on the surface. Instead, the remaining free space in the interfacial layer is being shared among TBA<sup>+</sup> cations and iodide anions, and hence, there is virtually no segregation perpendicular to the surface. It is also interesting to mention that the MD simulations indicate that the butyl chains are primarily orientated along the water surface at low concentration and point into the solutions at higher concentration, which requires less space.<sup>294</sup>

The strong surfactant activity of both anions and cations, which is the reason that no dipole is formed by TBA<sup>+</sup> and I<sup>−</sup> ion pairs perpendicular to the surface (no formation of a strong electric double layer), is consistent with zero cutoff

energy shifts in the PE spectra, as shown in Figure 35. This

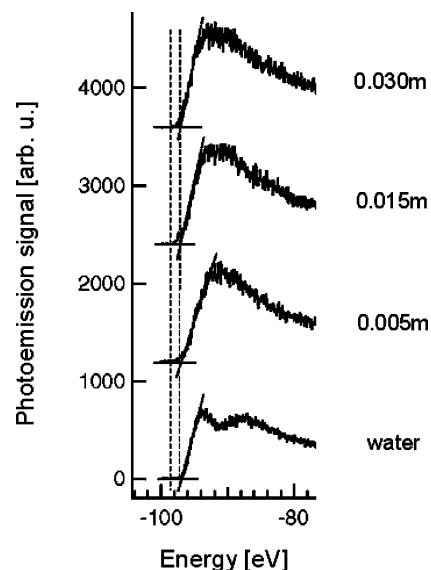


**Figure 35.** Cutoff region of TBAI photoemission spectra as a function of salt concentration, as labeled. Zero or very small cutoff energy shifts are observed, implying that no molecular dipoles perpendicular to the surface are formed by adsorbed ion pairs.

figure displays TBAI PE spectra in the cutoff region, obtained for some selected concentrations, covering the submonolayer coverage to complete segregation. According to Figure 10, the creation of a surface dipole in the top layer with an appreciable component perpendicular to the solution surface would cause a shift (eq 3.5) of the secondary electron cutoff. This is obviously not the case. From Figure 32, we have already seen that all other spectral features also remain at constant energy when the concentration is changed. Hence, we conclude that the surface potential is not changed upon formation of the TBAI segregation layer, and consequently, both anions and cations reside in the top surface layer, in agreement with the MD results.

In the previous section, we discussed the surface adsorption of iodide in aqueous NaI solution in terms of the Gibbs adsorption free energy; the corresponding Langmuir fit of the PE data from TBAI aqueous solutions is presented in Figure 36, yielding  $\Delta G_{\text{ads}} = -3.4 \pm 0.2$  kcal/mol for iodide,

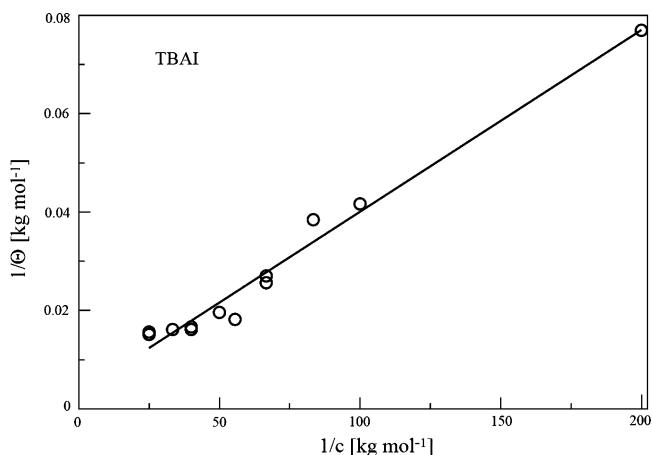


**Figure 36.** TBAI aqueous solution: I<sup>−</sup>(4d) intensities vs concentration data (from Figure 33) fitted to eq 5.2, which is the reciprocal of the usual expression of the Langmuir isotherm model. From the slope, one obtains  $\Delta G_{\text{ads}} = -3.4 \pm 0.2$  kcal/mol for iodide. The regression equation is  $y = (0.003 \pm 0.001) + x(37 \pm 2) \times 10^{-5}$ .



which is twice the value for iodide in NaI solution (from PE data). A larger negative  $\Delta G_{\text{ads}}$  value for the TBAI solution is indeed expected because higher (surface) signal is obtained for a much lower bulk concentration, which is equivalent to reaching the completed monolayer at much lower concentration. Considering the fact that, in the TBAI photoemission experiment, the iodide signal is being sampled from much a smaller region (the deeper layers probed do not contribute), the  $\Delta G_{\text{ads}}$  value derived in this case is quite possibly quantitatively accurate. This conclusion is, in fact, supported by cross-checking the surface population ratios of TBAI and NaI, i.e.,  $c_{\text{surf}}(\text{TBAI})/c_{\text{surf}}(\text{NaI}) = \exp(\Delta\Delta G/RT) \approx 80$ , which compares to 70 as inferred from Figure 31.

When comparing solutions of TBAI and TBABr, one can study the effect of ion polarizability on the structure of the segregation layer. Figure 37 displays PE spectra of 0.02 *m*

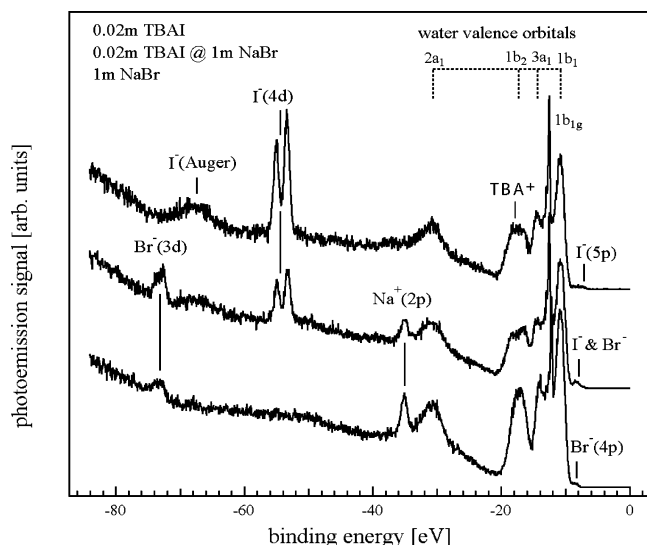


**Figure 37.** Photoemission spectrum of 0.02 *m* TBAI, compared to those of 1 *m* NaBr and a mixture of 1 *m* NaBr and 0.02 *m* TBAI aqueous solutions. The excitation energy was 100 eV. Intensities are with respect to the synchrotron photon flux. Reprinted with permission from ref 296. Copyright 2005, Elsevier.

TBAI aqueous solution (top), 0.2 *m* TBAI dissolved in 1 *m* aqueous NaBr (center), and pure 1 *m* NaBr aqueous solution. The photon energy was 100 eV. The most important observation is that the iodide signal decreases by only about 60% in the mixed solution, even though the bromide concentration is 50 times higher than the iodide concentration. This is a direct reflection of the larger propensity of iodide to exist at the surface. In addition, as suggested by MD simulations,<sup>296</sup> the TBA<sup>+</sup> concentration profile tends to shift slightly toward the bulk, in mixed solutions, which is a consequence of the Coulomb attraction between bromide anions and TBA<sup>+</sup> cations. This can explain the experimentally observed lower surface activity of TBABr as compared to TBAI.<sup>124</sup>

## 6. Concluding Remarks

Extreme ultraviolet (EUV) photoelectron spectroscopy was applied for the study of the electronic structure of liquid water and aqueous solutions. It was shown that, when a thin liquid microjet in a vacuum is used, photoelectrons from the liquid interface can be energy-resolved. The fast equilibration of the solution interface enables investigations as a function of salt concentration. The results here, which were largely

obtained for liquid water and aqueous solutions of simple salts using synchrotron radiation of no higher than 120 eV photon energy, provided orbital energies of liquid water and vertical detachment energies and electron affinities of hydrated anions and cations, respectively. In addition, structural information on the interfaces of aqueous NaI and surface-active tetrabutylammonium iodide was inferred from the photoemission signal and spectrum as a function of the salt concentration. Extending the photon energy, to ionize inner shells (e.g., oxygen 1s of water), is expected to unravel some of the open issues of the geometric and electronic structures of water and solutions. This includes the precise location of the anions and cations within the solution interface and the distribution of electron binding energies of surface, bulk, and solvent water. Of central interest is also the accurate determination of the electron probing depth in aqueous solutions, which is crucial for interpreting the experimental photoemission spectra. In future angle-resolved photoemission experiments, it will be possible to obtain detailed information on the orientation of the surface molecules.

A new aspect to be investigated is fast photon-induced processes in water and solution by pump–probe photoemission experiments with femtosecond laser pulses. The strength of such experiments, which have not yet been performed on aqueous systems, is the ability to measure absolute energies of transient valence or core states. Aqueous systems of interest here extend beyond salt solutions. In particular, solvation of biological relevant molecules by water, aqueous electron attachment, and charge-transfer processes are a major challenge. This is closely related to water pH changes, and it is thus important to determine the structures and energies of hydrated H<sup>+</sup> and OH<sup>−</sup> ions, which can be accessed by photoemission measurements of aqueous acids and bases.

## 7. Acknowledgment

We thank Prof. Ingolf V. Hertel for many discussions on the photoemission data from aqueous solutions. We are also grateful to our colleague Dr. Ramona Weber for her participation and many contributions to most aspects of this work. In addition, we are grateful to Prof. Pavel Jungwirth and Prof. Stephen E. Bradforth for stimulating discussions and meetings on various theoretical and experimental aspects of this work. We also thank Martin Mucha for discussions on the interpretation of the concentration profiles measured in photoemission.

## 8. References

- (1) Onsager, L.; Samaras, N. N. T. *J. Phys. Chem.* **1934**, 2, 528.
- (2) Franks, F., Ed. *Water: A Comprehensive Treatise*; Plenum Press: London, 1973; Vol. 3.
- (3) Stillinger, F. H. *Science* **1980**, 209, 451.
- (4) Robinson, G. W. *Water in Biology, Chemistry, and Physics: Experimental Overviews and Computational Methodologies*; World Scientific: Singapore, 1996.
- (5) Barthel, J. M. G.; Krienke, H.; Kunz, W. *Physical Chemistry of Electrolyte Solutions*; Springer, New York, 1998; Vol. 5.
- (6) Bockris, J. O. M.; Reddy, A. K. N. *Modern Electrochemistry 1, Ionics*; Kluwer Academic Publishers: Dordrecht, The Netherlands, 1998.
- (7) Adamson, A. W. *Physical Chemistry of Surfaces*, 5th ed.; Wiley: New York, 1990.
- (8) Gouy, G. *J. Phys.* **1910**, 9, 457.
- (9) Gouy, G. *Ann. Phys.* **1917**, 7, 129.
- (10) Chapman, D. L. *Philos. Mag.* **1913**, 25, 475.
- (11) Debye, P.; Hückel, E. *Z. Phys.* **1923**, 24, 185.

- (12) Debye, P. *Phys. Z.* **1924**, 25, 93.
- (13) Ball, P. *Nature* **2003**, 423, 25.
- (14) Oum, K. W.; Lakin, M. J.; DeHaan, D. O.; Brauers, T.; Finlayson-Pitts, B. J. *Science* **1998**, 279, 74.
- (15) Finlayson-Pitts, B. J. *Chemistry of the Upper and Lower Atmosphere—Theory, Experiment, and Applications*; Academic Press: San Diego, 2000.
- (16) Finlayson-Pitts, B. J. *Chem. Rev.* **2003**, 103, 4801.
- (17) Knipping, E. M.; Lakin, M. J.; Foster, K. L.; Jungwirth, P.; Tobias, D. J.; Gerber, R. B.; Dabdub, D.; Finlayson-Pitts, B. J. *Science* **2000**, 288, 301.
- (18) Garrett, B. C. *Science* **2004**, 303, 1146.
- (19) Hu, J. H.; Shi, Q.; Davidovits, P.; Worsnop, D. R.; Zahniser, M. S.; Kolb, C. E. *J. Phys. Chem.* **1995**, 99, 8768.
- (20) Laskin, A.; Gaspar, D. J.; Wang, W. H.; Hunt, S. W.; Cowin, J. P.; Colson, S. D.; Finlayson-Pitts, B. J. *Science* **2003**, 301, 340.
- (21) Hunt, S. W.; Roeselova, M.; Wang, W.; Wingen, L. M.; Knipping, E. M.; Tobias, D. J.; Dabdub, D.; Finlayson-Pitts, B. J. *J. Phys. Chem. A* **2004**, 108, 11559.
- (22) Wagner, C. *Phys. Z.* **1924**, 25, 474.
- (23) Shultz, M. J.; Baldelli, S.; Schnitzer, C.; Simonelli, D. J. *Phys. Chem. B* **2002**, 106, 5313.
- (24) Richmond, G. L. *Chem. Rev.* **2002**, 102, 2693.
- (25) Liu, D. F.; Ma, G.; Levering, L. M.; Allen, H. C. *J. Phys. Chem. B* **2004**, 108, 2252.
- (26) Raymond, E. A.; Richmond, G. L. *J. Phys. Chem. B* **2004**, 108, 5051.
- (27) Petersen, P. B.; Johnson, J. C.; Knutsen, K. P.; Saykally, R. J. *Chem. Phys. Lett.* **2004**, 397, 46.
- (28) Petersen, P. B.; Saykally, R. J. *Chem. Phys. Lett.* **2004**, 397, 51.
- (29) Ghosal, S.; Hemminger, J. C.; Bluhm, H.; Mun, B. S.; Hebenstreit, E. L. D.; Ketteler, G.; Ogletree, D. F.; Requejo, F. G.; Salmeron, M. *Science* **2005**, 307, 563.
- (30) Jungwirth, P.; Tobias, D. J. *J. Phys. Chem. B* **2001**, 105, 10468.
- (31) Jungwirth, P.; Tobias, D. J. *J. Phys. Chem. B* **2002**, 106, 6361.
- (32) Vacha, R.; Slavicek, P.; Mucha, M.; Finlayson-Pitts, B. J.; Jungwirth, P. *J. Phys. Chem. A* **2004**, 108, 11573.
- (33) Mucha, M.; Frigato, T.; Levering, L. M.; Allen, H. C.; Tobias, D. J.; Dang, L. X.; Jungwirth, P. *J. Phys. Chem. B* **2005**, 109, 7617.
- (34) Petersen, P. B.; Saykally, R. J.; Mucha, M.; Jungwirth, P. *J. Phys. Chem.* **2005**, 109, 10915.
- (35) Markovich, G.; Giniger, R.; Levin, M.; Chesnovsky, O. *J. Chem. Phys.* **1991**, 95, 9416.
- (36) Wang, X. B.; Yang, X.; Nicholas, J. B.; Wang, L. S. *Science* **2001**, 294, 1322.
- (37) Hartke, B.; Charvat, A.; Reich, M.; Abel, B. *J. Chem. Phys.* **2002**, 116, 3588.
- (38) Liu, K.; Brown, M. G.; Cruzan, J. D.; Saykally, R. J. *Science* **1996**, 271, 62.
- (39) Platzmann, R.; Franck, J. Z. *Phys.* **1954**, 138, 411.
- (40) Blandamer, M. J.; Fox, M. F. *Chem. Rev.* **1970**, 70, 59.
- (41) Kloepper, J. A.; Vilchiz, V. H.; Lenchenkov, V. A.; Chen, X. Y.; Bradforth, S. E. *J. Chem. Phys.* **2002**, 117, 766.
- (42) Vilchiz, V. H.; Kloepper, J. A.; Germaine, A. C.; Lenchenkov, V. A.; Bradforth, S. E. *J. Phys. Chem. A* **2001**, 105, 1711.
- (43) Lehr, L.; Zanni, M. T.; Frischkorn, C.; Weinkauff, R.; Neumark, D. M. *Science* **1999**, 284, 635.
- (44) Barthel, E. R.; Schwartz, B. J. *Chem. Phys. Lett.* **2003**, 375, 435.
- (45) Crowell, R. A.; Lian, R.; Shkrob, I. A.; Bartels, D. M.; Chen, X.; Bradforth, S. E. *J. Chem. Phys.* **2004**, 120, 11712.
- (46) Sauer Jr., M. C.; Shkrob, I. A.; Lian, R.; Crowell, R. A.; Bartels, D. M.; Chen, X.; Suffern, D.; Bradforth, S. E. *J. Phys. Chem. A* **2004**, 108, 10414.
- (47) Sorenson, J. M.; Hura, G.; Glaeser, R. M.; Head-Gordon, T. *J. Chem. Phys.* **2000**, 113, 9149.
- (48) Krack, M.; Gambirasio, A.; Parrinello, M. *J. Chem. Phys.* **2002**, 117, 9409.
- (49) Hura, G.; Russo, D.; Glaeser, R. M.; Head-Gordon, T.; Krack, M.; Parrinello, M. *Phys. Chem. Chem. Phys.* **2003**, 5, 1981.
- (50) Head-Gordon, T.; Hura, G. *Chem. Rev.* **2002**, 102, 2651.
- (51) Soper, A. K.; Neilson, G. W.; Enderby, J. E.; Howe, R. A. *J. Phys. C: Solid State Phys.* **1977**, 10, 17931801.
- (52) Leberman, R.; Soper, A. K. *Nature* **1995**, 378, 364.
- (53) Soper, A. K. *Chem. Phys.* **2000**, 258, 121.
- (54) Botti, A.; Bruni, F.; Imberti, S.; Ricci, M. A.; Soper, A. K. *J. Chem. Phys.* **2004**, 121, 7840.
- (55) Postorino, P.; Tromp, R. H.; Ricci, M. A.; Soper, A. K.; Neilson, G. W. *Nature* **1993**, 366, 668.
- (56) Tromp, R. H.; Postorino, P.; Neilson, G. W.; Ricci, M. A.; Soper, A. K. *J. Chem. Phys.* **1994**, 101, 6210.
- (57) Soper, A. K. *J. Phys.: Condens. Matter* **1997**, 9, 2717.
- (58) Dillon, S. R.; Dougherty, R. C. *J. Phys. Chem. A* **2002**, 106, 7647.
- (59) Marechal, Y. *J. Mol. Struct.* **2004**, 700, 217.
- (60) Dougherty, R. C.; Howard, L. N. *Biophys. Chem.* **2003**, 105, 269.
- (61) Fecko, C. J.; Eaves, J. D.; Loparo, J. J.; Tokmakoff, A.; Geissler, P. L. *Science* **2003**, 301, 1698.
- (62) Stenger, J.; Madsen, D.; Hamm, P.; Nibbering, E. T. J.; Elsaesser, T. *Phys. Rev. Lett.* **2001**, 8702.
- (63) Laenen, R.; Rauscher, C.; Laubereau, A. *J. Phys. Chem. B* **1998**, 102, 9304.
- (64) Woutersen, S.; Emmerichs, U.; Bakker, H. J. *Science* **1997**, 278, 658.
- (65) Asbury, J. B.; Steinell, T.; Kwak, K.; Corcelli, S. A.; Lawrence, C. P.; Skinner, J. L.; Fayer, M. D. *J. Chem. Phys.* **2004**, 121, 12431.
- (66) Bakker, H. J.; Lock, A. J.; Madsen, D. *Chem. Phys. Lett.* **2004**, 384, 236.
- (67) Nibbering, E. T. J.; Elsaesser, T. *Chem. Rev.* **2004**, 104, 1887.
- (68) Gale, G. M.; Gallot, G.; Hache, F.; Lascoux, N.; Bratos, S.; Leicknam, J. C. *Phys. Rev. Lett.* **1999**, 82, 1068.
- (69) Woutersen, S.; Bakker, H. J. *Phys. Rev. Lett.* **1999**, 83, 2077.
- (70) Kropman, M. F.; Nienhuys, H. K.; Woutersen, S.; Bakker, H. J. *J. Phys. Chem. A* **2001**, 105, 4622.
- (71) Corcelli, S. A.; Skinner, J. L. *J. Phys. Chem. A* **2005**, 109, 6154.
- (72) Kropman, M. F.; Bakker, H. J. *J. Chem. Phys.* **2001**, 115, 8942.
- (73) Kropman, M. F.; Bakker, H. J. *Science* **2001**, 291, 2118.
- (74) Kropman, M. F.; Bakker, H. J. *Chem. Phys. Lett.* **2003**, 370, 741.
- (75) Omta, A. W.; Kropman, M. F.; Woutersen, S.; Bakker, H. J. *Science* **2003**, 301, 347.
- (76) Huse, N.; Ashihara, S.; Nibbering, E. T. J.; Elsaesser, T. *Chem. Phys. Lett.* **2005**, 404, 389.
- (77) Cowan, M. L.; Bruner, B. D.; Huse, N.; Dwyer, J. R.; Chugh, B.; Nibbering, E. T. J.; Elsaesser, T.; Miller, R. J. D. *Nature* **2005**, 434, 199.
- (78) Soper, A. K. *J. Phys.: Condens. Matter* **2005**, 17, S3273.
- (79) Pimentel, G. C.; McClellan, A. L. *The Hydrogen Bond*; Freeman: San Francisco, 1960.
- (80) Lawrence, C. P.; Skinner, J. L. *J. Chem. Phys.* **2003**, 118, 264.
- (81) Woutersen, S.; Bakker, H. J. *Nature* **1999**, 402, 507.
- (82) Möller, K. B.; Rey, R.; Hynes, J. T. *J. Phys. Chem. A* **2004**, 108, 1275.
- (83) Du, Q.; Superfine, R.; Freysz, E.; Shen, Y. R. *Phys. Rev. Lett.* **1993**, 70, 2313.
- (84) Wilson, K. R.; Cavalleri, M.; Rude, B. S.; Schaller, R. D.; Nilsson, A.; Pettersson, L. G. M.; Goldman, N.; Catalano, T.; Bozek, J. D.; Saykally, R. J. *J. Phys.: Condens. Matter* **2002**, 14, L221.
- (85) Kuo, I.-F. W.; Mundy, C. J. *Science* **2004**, 303, 658.
- (86) Bergmann, U.; Wernet, P.; Glatzel, P.; Cavalleri, M.; Pettersson, L. G. M.; Nilsson, A.; Cramer, S. P. *Phys. Rev. B* **2002**, 66, 092107.
- (87) Myneni, S.; Luo, Y.; Naslund, L. A.; Cavalleri, M.; Ojamae, L.; Ogasawara, H.; Pelmenchikov, A.; Wernet, P.; Vaterlein, P.; Heske, C.; Hussain, Z.; Pettersson, L. G. M.; Nilsson, A. *J. Phys.: Condens. Matter* **2002**, 14, L213.
- (88) Cavalleri, M.; Ogasawara, H.; Pettersson, L. G. M.; Nilsson, A. *Chem. Phys. Lett.* **2002**, 364, 363.
- (89) Naslund, L. A.; Cavalleri, M.; Ogasawara, H.; Nilsson, A.; Pettersson, L. G. M.; Wernet, P.; Edwards, D. C.; Sandstrom, M.; Myneni, S. J. *J. Phys. Chem. A* **2003**, 107, 6869.
- (90) Smith, J. D.; Cappa, C. D.; Wilson, K. R.; Messer, B. M.; Cohen, R. C.; Saykally, R. J. *Science* **2004**, 306, 851.
- (91) Kashtanov, S.; Augustsson, A.; Luo, Y.; Guo, J. H.; Sathe, C.; Rubensson, J. E.; Siegbahn, H.; Nordgren, J.; Agren, H. *Phys. Rev. B* **2004**, 69.
- (92) Wernet, P.; Nordlund, D.; Bergmann, U.; Cavalleri, M.; Odelius, M.; Ogasawara, H.; Naslund, L. A.; Hirsch, T. K.; Ojamae, L.; Glatzel, P.; Pettersson, L. G. M.; Nilsson, A. *Science* **2004**, 304, 995.
- (93) Stöhr, J. *NEXAFS Spectroscopy*; Springer-Verlag, Berlin, 1992.
- (94) Koch, W.; Holthausen, M. C. *A Chemist's Guide to Density Functional Theory*, 2nd ed.; Wiley-VCH: New York, 2002.
- (95) Xenides, D.; Randolph, B. R.; Rode, B. M. *J. Chem. Phys.* **2005**, 122.
- (96) Vrbka, L.; Mucha, M.; Minofar, B.; Jungwirth, P.; Brown, E. C. *Curr. Opin. Colloid Interface Sci.* **2004**, 9, 67.
- (97) Markovich, G.; Pollack, S.; Giniger, R.; Chesnovsky, O. *J. Chem. Phys.* **1994**, 101, 9344.
- (98) Choi, J. H.; Kuwata, K. T.; Cao, Y. B.; Okumura, M. *J. Phys. Chem. A* **1998**, 102, 503.
- (99) Nielsen, S. B.; Masella, M.; Kebarle, P. *J. Phys. Chem. A* **1999**, 103, 9891.
- (100) Ding, C. F.; Wang, X. B.; Wang, L. S. *J. Phys. Chem. A* **1998**, 102, 8633.
- (101) Steel, E. A.; Merz, K. M.; Selinger, A.; Castleman, A. W. *J. Phys. Chem.* **1995**, 99, 7829.
- (102) Combariza, J. E.; Kestner, N. R.; Jortner, J. *Chem. Phys. Lett.* **1993**, 203, 423.
- (103) Perera, L.; Berkowitz, M. L. *J. Chem. Phys.* **1993**, 99, 4222.
- (104) Dang, L. X.; Garret, B. C. *J. Phys. Chem.* **1993**, 99, 2972.
- (105) Hertel, I. V.; Hüglin, C.; Nitsch, C.; Schulz, C. P. *Phys. Rev. Lett.* **1991**, 1767.
- (106) Barnett, R. N.; Landman, U. *Phys. Rev. Lett.* **1993**, 70, 1775.

- (107) Misaizu, F.; Tsukamoto, K.; Sanekata, M.; Fuke, K. *Chem. Phys. Lett.* **1992**, *188*, 241.
- (108) Wang, X. B.; Yang, X.; Nicholas, J. B.; Wang, L. S. *J. Chem. Phys.* **2003**, *119*, 3631.
- (109) Yang, X.; Kiran, B.; Wang, X. B.; Wang, L. S.; Mucha, M.; Jungwirth, P. *J. Phys. Chem. A* **2004**, *108*, 7820.
- (110) Minofar, B.; Mucha, M.; Jungwirth, P.; Yang, X.; Fu, Y. J.; Wang, X. B.; Wang, L. S. *J. Am. Chem. Soc.* **2004**, *126*, 11691.
- (111) Minofar, B.; Vrbka, L.; Mucha, M.; Jungwirth, P.; Yang, X.; Wang, X. B.; Fu, Y. J.; Wang, L. S. *J. Phys. Chem. A* **2005**, *109*, 5042.
- (112) Müller, I. B.; Cederbaum, L. S.; Tarantelli, F. J. *Phys. Chem. A* **2004**, *108*, 5831.
- (113) Hüfner, S. *Photoelectron Spectroscopy: Principles and Applications*; Springer-Verlag: Berlin, 1995.
- (114) Feuerbacher, B. *Photoemission and the Electronic Properties of Surfaces*; John Wiley & Sons: New York, 1978.
- (115) Pianetta, P. Low-Energy Electron Ranges in Matter, [http://xdb.lbl.gov/Section3/Sec\\_3-2.html](http://xdb.lbl.gov/Section3/Sec_3-2.html) (accessed Mar 2005).
- (116) Powell, C. J.; Jablonski, A.; Tilinin, I. S.; Tanuma, S.; Penn, D. R. *J. Electron Spectrosc.* **1999**, *98–99*, 1.
- (117) Jablonski, A.; Powell, C. J. *J. Electron Spectrosc.* **1999**, *100*, 137.
- (118) Fellnerfeldegg, H.; Siegbahn, H.; Asplund, L.; Kelfve, P.; Siegbahn, K. *J. Electron Spectrosc. Relat. Phenom.* **1975**, *7*, 421.
- (119) Faubel, M. Photoelectron spectroscopy at liquid surfaces. In *Photoionization and Photodetachment*; Ng, C. Y., Ed.; World Scientific: Singapore, 2000; Vol. 10A, Part 1, p 634.
- (120) Siegbahn, H. *J. Phys. Chem.* **1985**, *89*, 897.
- (121) Lundholm, M.; Siegbahn, H.; Holberg, S.; Arbman, M. *J. Electron Spectrosc. Relat. Phenom.* **1986**, *40*, 163.
- (122) Holmberg, S.; Moberg, R.; Zhong, C. Y.; Siegbahn, H. *J. Electron Spectrosc. Relat. Phenom.* **1986**, *41*, 337.
- (123) Holmberg, S.; Yuan, Z. C.; Moberg, R.; Siegbahn, H. *J. Electron Spectrosc. Relat. Phenom.* **1988**, *47*, 27.
- (124) Eschen, F.; Heyerhoff, M.; Morgner, H.; Vogt, J. *J. Phys.: Condens. Matter* **1995**, *7*, 1961.
- (125) Moberg, R.; Bokman, F.; Bohman, O.; Siegbahn, H. O. G. *J. Am. Chem. Soc.* **1991**, *113*, 3663.
- (126) Ballard, R. E.; Jones, J.; Sutherland, E. *Chem. Phys. Lett.* **1984**, *112*, 310.
- (127) Ballard, R. E.; Jones, J.; Sutherland, E. *Chem. Phys. Lett.* **1984**, *112*, 452.
- (128) Delahay, P.; Von Burg, K. *Chem. Phys. Lett.* **1981**, *83*, 250.
- (129) Watanabe, I.; Takahashi, N.; Tanida, H. *Chem. Phys. Lett.* **1998**, *287*, 714.
- (130) Charvat, A.; Lugovoj, E.; Faubel, M.; Abel, B. *Eur. Phys. J. D* **2002**, *20*, 573.
- (131) Faubel, M.; Steiner, B.; Toennies, J. P. *J. Chem. Phys.* **1997**, *106*, 9013.
- (132) Faubel, M.; Steiner, B.; Toennies, J. P. *Mol. Phys.* **1997**, *90*, 327.
- (133) Bohm, R.; Morgner, H.; Oberbrodthage, J.; Wulf, M. *Surf. Sci.* **1994**, *317*, 407.
- (134) Jordan, K. D. *Science* **2004**, *306*, 618.
- (135) Bragg, A. E.; Verlet, J. R. R.; Kammrath, A.; Cheshnovsky, O.; Neumark, D. M. *Science* **2004**, *306*, 669.
- (136) Vilchiz, V. H.; Chen, X. Y.; Klopfer, J. A.; Bradforth, S. E. *Radiat. Phys. Chem.* **2005**, *72*, 159.
- (137) Klopfer, J. A.; Vilchiz, V. H.; Lenchenkov, V. A.; Bradforth, S. E. *Chem. Phys. Lett.* **1998**, *298*, 120.
- (138) Klopfer, J. A.; Vilchiz, V. H.; Lenchenkov, V. A.; Bradforth, S. E. *Liq. Dyn.: Exp., Simul. Theory* **2002**, *820*, 108.
- (139) Klopfer, J. A.; Vilchiz, V. H.; Lenchenkov, V. A.; Germaine, A. C.; Bradforth, S. E. *J. Chem. Phys.* **2000**, *113*, 6288.
- (140) Zhan, C. G.; Dixon, D. A. *J. Phys. Chem. B* **2003**, *107*, 4403.
- (141) Tauber, M. J.; Mathies, R. A. *Chem. Phys. Lett.* **2002**, *354*, 518.
- (142) Laenen, R.; Roth, T. *J. Mol. Struct.* **2001**, *598*, 37.
- (143) Laenen, R.; Roth, T.; Laubereau, A. *Phys. Rev. Lett.* **2000**, *85*, 50.
- (144) Lehr, L.; Zanni, M. T.; Frischkorn, C.; Weinkauff, R.; Neumark, D. M. *Science* **1999**, *284*, 635.
- (145) Jimenez, R.; Fleming, G. R.; Kumar, P. V.; Maroncelli, M. *Nature* **1994**, *369*, 471.
- (146) Baltuska, A.; Emde, M. F.; Pshenichnikov, M. S.; Wiersma, D. A. *J. Phys. Chem. A* **1999**, *103*, 10065.
- (147) Emde, M. F.; Baltuska, A.; Kummrow, A.; Pshenichnikov, M. S.; Wiersma, D. A. *Phys. Rev. Lett.* **1998**, *80*, 4645.
- (148) Yang, C. Y.; Wong, K. F.; Skaf, M. S.; Rossky, P. J. *J. Chem. Phys.* **2001**, *114*, 3598.
- (149) Assel, M.; Laenen, R.; Laubereau, A. *Chem. Phys. Lett.* **2000**, *317*, 13.
- (150) Laenen, R.; Assel, M.; Laubereau, A. *Bull. Polish Acad. Sci.: Chem.* **1999**, *47*, 283.
- (151) Assel, M.; Laenen, R.; Laubereau, A. *Chem. Phys. Lett.* **1998**, *289*, 267.
- (152) Son, D. H.; Kambhampati, P.; Kee, T. W.; Barbara, P. F. *Chem. Phys. Lett.* **2001**, *342*, 571.
- (153) Son, D. H.; Kambhampati, P.; Kee, T. W.; Barbara, P. F. *J. Phys. Chem.* **2001**, *105*, 8269.
- (154) Naslund, L. A.; Edwards, D. C.; Wernet, P.; Bergmann, U.; Ogasawara, H.; Pettersson, L. G. M.; Myneni, S.; Nilsson, A. *J. Phys. Chem. A* **2005**, *109*, 5995.
- (155) Naslund, L. A.; Luning, J.; Ufuktepe, Y.; Ogasawara, H.; Wernet, P.; Bergmann, U.; Pettersson, L. G. M.; Nilsson, A. *J. Phys. Chem. B* **2005**, *109*, 13835.
- (156) Guo, J. H.; Luo, Y.; Augustsson, A.; Rubensson, J. E.; Sathe, C.; Agren, H.; Siegbahn, H.; Nordgren, J. *Phys. Rev. Lett.* **2002**, *89*.
- (157) Wilson, K. R.; Rude, B. S.; Catalano, T.; Schaller, R. D.; Tobin, J. G.; Co, D. T.; Saykally, R. J. *J. Phys. Chem. B* **2001**, *105*, 3346.
- (158) Bakker, H. J.; Kropman, M. F.; Omta, A. W.; Woutersen, S. *Phys. Scr.* **2004**, *69*, C14.
- (159) Science Magazine Online, <http://www.sciencemag.org/cgi/content/full/306/5704/2013#water> (subscription required).
- (160) Zubavicus, Y.; Grunze, M. *Science* **2004**, *304*, 974.
- (161) Smith, J. D.; Cappa, C. D.; Messer, B. M.; Cohen, R. C.; Saykally, R. J. *Science* **2005**, *308*, 5723.
- (162) Hetenyi, B.; De Angelis, F.; Giannozzi, P.; Car, R. *J. Chem. Phys.* **2004**, *120*, 8632.
- (163) Soper, A. K.; Bruni, F.; Ricci, M. A. *J. Chem. Phys.* **1997**, *106*, 247.
- (164) Luzar, A. *J. Chem. Phys.* **2000**, *113*, 10663.
- (165) Wilson, K. R.; Tobin, J. G.; Ankudinov, A. L.; Rehr, J. J.; Saykally, R. J. *Phys. Rev. Lett.* **2000**, *85*, 4289.
- (166) Stenger, J.; Madsen, D.; Hamm, P.; Nibbering, E. T. J.; Elsaesser, T. *J. Phys. Chem. A* **2002**, *106*, 2341.
- (167) Woutersen, S.; Emmerichs, U.; Nienhuys, H. K.; Bakker, H. J. *Phys. Rev. Lett.* **1998**, *81*, 1106.
- (168) Röntgen, W. C. *Ann. Phys. Chem.* **1892**, *45*, 91.
- (169) Bader, J. S.; Cortis, C. M.; Berne, B. J. *The J. Chem. Phys.* **1997**, *106*, 2372.
- (170) Oum, K. W.; Lakin, M. J.; Finlayson-Pitts, B. J. *Geophys. Res. Lett.* **1998**, *25*, 3923.
- (171) Landau, L. D.; Lifschitz, E. M. *Statistical Physics*; Pergamon Press: London, 1959; Vol. 5.
- (172) Wilson, M. A.; Pohorille, A. *J. Chem. Phys.* **1991**, *95*, 6005.
- (173) Dang, L. X.; Chang, T. M. *J. Phys. Chem. B* **2002**, *106*, 235.
- (174) Bradforth, S. E.; Jungwirth, P. *J. Phys. Chem. A* **2002**, *106*, 1286.
- (175) Jungwirth, P. *J. Phys. Chem. A* **2000**, *104*, 145.
- (176) Jungwirth, P.; Tobias, D. J. *J. Phys. Chem. B* **2000**, *104*, 7702.
- (177) Jungwirth, P.; Tobias, D. J. *J. Phys. Chem. A* **2002**, *106*, 379.
- (178) Mucha, M.; Jungwirth, P. *J. Phys. Chem. B* **2003**, *107*, 8271.
- (179) Roeselova, M.; Jungwirth, P.; Tobias, D. J.; Gerber, R. B. *J. Phys. Chem. B* **2003**, *107*, 12690.
- (180) Roeselova, M.; Kaidor, U.; Jungwirth, P. *J. Phys. Chem. A* **2000**, *104*, 6523.
- (181) Salvador, P.; Curtis, J. E.; Tobias, D. J.; Jungwirth, P. *Phys. Chem. Chem. Phys.* **2003**, *5*, 3752.
- (182) Tobias, D. J.; Jungwirth, P.; Parrinello, M. *J. Chem. Phys.* **2001**, *114*, 7036.
- (183) Vrbka, L.; Jungwirth, P. *Aust. J. Chem.*, manuscript submitted.
- (184) Eiselthal, K. B. *Chem. Rev.* **1996**, *96*, 1343.
- (185) Marcus, Y. *Ion Solvation*; Wiley: Chichester, U.K., 1985.
- (186) Marcus, Y. *Pure Appl. Chem.* **1987**, *59*, 1093.
- (187) Marcus, Y. *Chem. Rev.* **1988**, *88*, 1475.
- (188) Babu, C. S.; Lim, C. J. *Chem. Phys.* **2001**, *114*, 889.
- (189) Hamann, C. H.; Hamnett, A.; Vielstich, W. *Electrochemistry*; Wiley-VCH: Weinheim, Germany, 1998.
- (190) Narten, A. H. *J. Chem. Phys.* **1972**, *56*, 5681.
- (191) Narten, A. H.; Vaslow, F.; Levy, H. A. *J. Chem. Phys.* **1973**, *58*, 5017.
- (192) Bernal, J. D.; Fowler, R. H. *J. Chem. Phys.* **1933**, *1*, 515.
- (193) Soper, A. K.; Phillips, M. G. *Chem. Phys.* **1986**, *107*, 47.
- (194) Cappa, C. D.; Smith, J. D.; Wilson, K. R.; Messer, B. M.; Gilles, M. K.; Cohen, R. C.; Saykally, R. J. *J. Phys. Chem. B* **2005**, *109*, 7046.
- (195) Kohno, J.; Mafune, F.; Kondow, T. *J. Phys. Chem. A* **2001**, *105*, 5990.
- (196) Jortner, J.; Ottolenghi, M.; Stein, G. *J. Phys. Chem.* **1964**, *68*, 247.
- (197) Sheu, W.-S.; Rossky, P. J. *J. Phys. Chem.* **1996**, *100*, 1295.
- (198) Chen, X.; Klopfer, J. A.; Bradforth, S. E.; Lian, R.; Crowell, R. A.; Shkrob, I. A., manuscript in preparation.
- (199) Coe, J. V. *Int. Rev. Phys. Chem.* **2001**, *20*, 33.
- (200) Garrett, B. C.; Dixon, D. A.; Camaioni, D. M.; Chipman, D. M.; Johnson, M. A.; Jonah, C. D.; Kimmel, G. A.; Miller, J. H.; Rescigno, T. N.; Rossky, P. J.; Xantheas, S. S.; Colson, S. D.; Laufer, A. H.; Ray, D.; Barbara, P. F.; Bartels, D. M.; Becker, K. H.; Bowen, H.; Bradforth, S. E.; Carmichael, I.; Coe, J. V.; Corrales, L. R.; Cowin, J. P.; Dupuis, M.; Eiselthal, K. B.; Franz, J. A.; Gutowski, M. S.; Jordan, K. D.; Kay, B. D.; LaVerne, J. A.; Lymar, S. V.; Madey, T. E.; McCurdy, C. W.; Meisel, D.; Mukamel, S.; Nilsson, A. R.; Orlando, T. M.; Petrik, N. G.; Pimblott, S. M.; Rustad, J. R.; Schenter,



- G. K.; Singer, S. J.; Tokmakoff, A.; Wang, L. S.; Wittig, C.; Zwier, T. S. *Chem. Rev.* **2005**, *105*, 355.
- (201) Kropman, M. F.; Bakker, H. J. *Chem. Phys. Lett.* **2002**, *362*, 349.
- (202) Kondow, T.; Mafune, F. *Annu. Rev. Phys. Chem.* **2000**, *51*, 731.
- (203) Zangwill, A. *Physics at Surfaces*; Cambridge University Press, 1992.
- (204) Ertl, G.; Küppers, J. *Low energy electrons and surfaces chemistry*; VCH: Weinheim, 1985.
- (205) Chandler, D. *Introduction to Modern Statistical Mechanics*; Oxford University Press: NY 1987, 1987.
- (206) Allen, M. P.; Tildesley, D. J. *Computer Simulations of Liquids*; Clarendon Press: Oxford, 1987.
- (207) Aarts, D. G. A. L.; Schmidt, M.; Lekkerkerker, N. J. *Science* **2004**, *304*, 847.
- (208) Robstein, R. J. *Physiochemical Hydrodynamics*; Wiley: Hoboken, NJ, 2003.
- (209) Sanyal, M. K.; Sinha, S. K.; Huang, K. G.; Ocko, B. M. *Phys. Rev. Lett.* **1991**, *66*, 628.
- (210) Braslau, A.; Pershan, P. S.; Swislow, G.; Ocko, B. M.; Alsnelsen, J. *Phys. Rev. A* **1988**, *38*, 2457.
- (211) Schwartz, D. K.; Schlossman, M. L.; Kawamoto, E. H.; Kellogg, G. J.; Pershan, P. S.; Ocko, B. M. *Phys. Rev. A* **1990**, *41*, 5687.
- (212) Magnussen, O. M.; Ocko, B. M.; Regan, M. J.; Penanen, K.; Pershan, P. S.; Deutsch, M. *Phys. Rev. Lett.* **1995**, *74*, 4444.
- (213) Regan, M. J.; Pershan, P. S.; Magnussen, O. M.; Ocko, B. M.; Deutsch, M.; Berman, L. E. *Phys. Rev. B* **1996**, *54*, 9730.
- (214) Shpyrko, O.; Huber, P.; Grigoriev, A.; Pershan, P.; Ocko, B.; Tostmann, H.; Deutsch, M. *Phys. Rev. B* **2003**, *67*.
- (215) Angell, C. A. *Annu. Rev. Phys. Chem.* **1983**, *34*, 593.
- (216) Lide, D. R., Ed. *Handbook of Chemistry and Physics*, 77th ed; CRC Press: Boca Raton, FL, 1997.
- (217) Shpyrko, O.; Fukuto, M.; Pershan, P.; Ocko, B.; Kuzmenko, I.; Gog, T.; Deutsch, M. *Phys. Rev. B* **2004**, *69*.
- (218) Fradin, C.; Braslau, A.; Luzet, D.; Smilgies, D.; Alba, M.; Boudet, N.; Mecke, K.; Daillant, J. *Nature* **2000**, *403*, 871.
- (219) Castro, A.; Ong, S. W.; Eienthal, K. B. *Chem. Phys. Lett.* **1989**, *163*, 412.
- (220) Ward, A. F. H.; Tordai, L. *J. Chem. Phys.* **1946**, *14*, 453.
- (221) *Physical Chemistry*, 5th ed.; Moore, W. J., Ed.; Longman, London, 1972.
- (222) Bradshaw, A. M.; Eberhardt, W.; Freund, H.-J.; Hoffmann, F. M.; HKuhlenbeck, H.; Martensson, N.; Menzel, D.; Nilsson, A.; Williams, G. P.; Woodruff, D. P.; Wurth, W. *Application of Synchrotron Radiation: High-Resolution Studies of Molecules and Molecular Adsorbates*; Springer-Verlag: Berlin, 1995; Vol. 35.
- (223) Martensson, N.; Nilsson, A.; Eberhardt, W. *Applications of Synchrotron Radiation*; Springer-Verlag: Berlin, 1995.
- (224) Plummer, E. A.; Eberhardt, W. *Adv. Chem. Phys.* **1982**, *49*, 533.
- (225) Lüth, H. *Surfaces and Interfaces of Solid Materials*, 3rd ed.; Springer-Verlag: Berlin, 1996.
- (226) Marx, D. *Science* **2004**, *303*, 634.
- (227) Nordlund, D. Ph.D Thesis, Stockholm University, Stockholm, Sweden, 2004.
- (228) Becker, U.; Shirley, D. A. *VUV and Soft X-ray Photoionization*; Plenum Press: New York, 1996.
- (229) Berglund, C. N.; Spicer, W. E. *Phys. Rev. A: Gen. Phys.* **1964**, *136*, 1030.
- (230) Hedin, L.; Lee, J. D. *J. Electron Spectrosc. Relat. Phenom.* **2002**, *124*, 289.
- (231) Hedin, L.; Michiels, J.; Inglesfield, J. *Phys. Rev. B* **1998**, *58*, 15565.
- (232) Kevan, S. D.; Rotenberg, E. *J. Electron Spectrosc. Relat. Phenom.* **2001**, *117*, 57.
- (233) Stöhr, J.; Jaeger, R.; Rehr, J. J. *Phys. Rev. Lett.* **1983**, *51*, 821.
- (234) Heiner, C. E.; Dreyer, J.; Hertel, I. V.; Koch, N.; Ritze, H. H.; Widdra, W.; Winter, B. *Appl. Phys. Lett.* **2005**, *87*, 093501.
- (235) Schmidt, V. Electron spectroscopy of atoms using synchrotron radiation. In *Electron Spectroscopy of Atoms Using Synchrotron Radiation*; Cambridge University Press: Cambridge, U.K., 1997.
- (236) Cooper, J.; Zare, R. N. *The J. Chem. Phys.* **1968**, *48*, 942.
- (237) Banna, M. S.; McQuaide, B. H.; Malutski, R.; Schmidt, V. *J. Chem. Phys.* **1986**, *84*, 4739.
- (238) Christmann, K. *Surface Physical Chemistry*; Steinkopf: Darmstadt, Germany, 1991.
- (239) Franks, F. *Water: A Comprehensive Treatise*; Plenum Press: New York, 1972; Vol. 1.
- (240) Jablonski, A.; Powell, C. J. *Surf. Sci. Rep.* **2002**, *47*, 33.
- (241) Hayashi, H.; Watanabe, N.; Udagawa, Y.; Kao, C.-C. *J. Chem. Phys.* **1998**, *108*, 823.
- (242) Emfietzoglou, D.; Nikjoo, H. *Radiat. Res.* **2005**, *163*, 98.
- (243) Michaud, M.; Wen, A.; Sanche, L. *Radiat. Res.* **2003**, *159*, 3.
- (244) Cobut, V.; Frongillo, Y.; Patau, J. P.; Goulet, T.; Fraser, M. J.; Jay-Gerin, J. P. *Radiat. Phys. Chem.* **1998**, *51*, 229.
- (245) Martin, W. C.; Fuhr, J. R.; Kelleher, D. E.; Musgrove, A.; Podobedova, L.; Reader, J.; Saloman, E. B.; Sansonetti, C. J.; Wiese, W. L.; Mohr, P. J.; Olsen, K. *NIST Atomic Spectra Database*, version 2.0; National Institute of Standards and Technology: Gaithersburg, MD, 1999; available online at <http://physics.nist.gov/asd> (accessed Oct 15, 2004). Sansonetti, J. E.; Martin, W. C.; Young, S. L. *Handbook of Basic Atomic Spectroscopic Data*, version 1.1; National Institute of Standards and Technology: Gaithersburg, MD, 2004; available online at <http://physics.nist.gov/Handbook>.
- (246) Kurtz, R. L.; Usuki, N.; Stockbauer, R.; Madey, T. E. *J. Electron Spectrosc. Relat. Phenom.* **1986**, *40*, 35.
- (247) Tzvetkov, G.; Zubavichus, Y.; Koller, G.; Schmidt, T.; Heske, C.; Umbach, E.; Grunze, M.; Ramsey, M. G.; Netzer, F. P. *Surf. Sci.* **2003**, *543*, 131.
- (248) Sander, M. U.; Luther, K.; Troe, J. *Ber. Bunsen-Ges. Phys. Chem.* **1993**, *97*, 953.
- (249) Mozumder, A. *Phys. Chem. Chem. Phys.* **2002**, *4*, 1451.
- (250) Faubel, M.; Kisters, T. *Nature* **1989**, *339*, 527.
- (251) Faubel, M.; Schlemmer, S.; Toennies, J. P. *Z. Phys. D: Atoms Mol. Clusters* **1988**, *10*, 269.
- (252) Faubel, M.; Steiner, B. *Ber. Bunsen-Ges. Phys. Chem.* **1992**, *96*, 1167.
- (253) Kleinekofort, W.; Avdiev, J.; Brutschy, B. *Int. J. Mass Spectrom. Ion Process.* **1996**, *152*, 135.
- (254) Kleinekofort, W.; Pfenninger, A.; Plomer, T.; Griesinger, C.; Brutschy, B. *Int. J. Mass Spectrom. Ion Process.* **1996**, *156*, 195.
- (255) Wattenberg, A.; Barth, R. D.; Brutschy, B. *J. Mass Spectrom.* **1997**, *32*, 1350.
- (256) Wattenberg, A.; Sobott, F.; Barth, H. D.; Brutschy, B. *Int. J. Mass Spectrom.* **2000**, *203*, 49.
- (257) Abel, B.; Charvat, A.; Diederichsen, U.; Faubel, M.; Girmann, B.; Niemeyer, J.; Zeeck, A. *Int. J. Mass Spectrom.* **2005**, *243*, 177.
- (258) Hansson, B. A. M.; Berglund, M.; Hemberg, O.; Hertz, H. M. *J. Appl. Phys.* **2004**, *95*, 4432.
- (259) Korn, G.; Thoss, A.; Stiel, H.; Vogt, U.; Richardson, M.; Elsaesser, T.; Faubel, M. *Opt. Lett.* **2002**, *27*, 866.
- (260) Siegbahn, H.; Siegbahn, K. *J. Electron Spectrosc. Relat. Phenom.* **1973**, *2*, 319.
- (261) von Ardenne, M. *Tabellen der Elektronenphysik, Ionenphysik und Übermikroskopie*; VEB Deutscher Verlag der Wissenschaften: Berlin, 1956; Vol. 1.
- (262) Danilatos, G. D. *Adv. Electron. Electron Phys.* **1988**, *71*, 109.
- (263) Ogletree, D. F.; Bluhm, H.; Lebedev, G.; Fadley, C. S.; Hussain, Z.; Salmeron, M. *Rev. Sci. Instrum.* **2002**, *73*, 3872.
- (264) Pantford, J.; Pollmann, S.; Zhu, J. F.; Borgmann, D.; Denecke, R.; Steinruck, H. P. *Rev. Sci. Instrum.* **2005**, *76*, 014102.
- (265) Davies, J. T.; Rideal, E. K. *Interfacial Phenomena*; Academic Press: New York, 1963.
- (266) Steiner, B. Ph.D. Thesis, University of Göttingen, Göttingen, Germany, 1994.
- (267) Thiel, P. A.; Madey, T. L. *Surf. Sci. Rep.* **1987**, *7*, 211.
- (268) Shirley, D. A. *Phys. Rev. B* **1972**, *5*, 4709.
- (269) Winter, B.; Weber, R.; Widdra, W.; Dittmar, M.; Faubel, M.; Hertel, I. V. *J. Phys. Chem. A* **2004**, *108*, 2625.
- (270) Heller, J. M.; Hamm, R. N.; Birkhoff, R. D.; Painter, L. R. *J. Chem. Phys.* **1974**, *60*, 3483.
- (271) Winter, B.; Weber, R.; Hertel, I. V.; Faubel, M.; Jungwirth, P.; Brown, E. C.; Bradforth, S. E. *J. Am. Chem. Soc.* **2005**, *127*, 7203.
- (272) Farrell, J. R.; McTigue, P. J. *Electroanal. Chem.* **1982**, *139*, 37.
- (273) Born, M. *Z. Phys.* **1920**, *1*, 45.
- (274) Perry, J. H. *Chemical Engineers Handbook*; McGraw-Hill: New York, 1950.
- (275) Ben-Naim, A.; Marcus, Y. *J. Chem. Phys.* **1984**, *81*, 2016.
- (276) Hunt, P.; Sprik, M.; Vuilleumier, R. *Chem. Phys. Lett.* **2003**, *376*, 68.
- (277) Nilsson, A.; Ogasawara, H.; Cavalleri, M.; Nordlund, D.; Nyberg, M.; Pettersson, L. G. M. *J. Chem. Phys.* **2005**, *122*, 154505.
- (278) Silvestrelli, P. L.; Parrinello, M. *J. Chem. Phys.* **1999**, *111*, 3572.
- (279) Silvestrelli, P. L.; Parrinello, M. *Phys. Rev. Lett.* **1999**, *82*, 5415.
- (280) Shibaguchi, T.; Onuki, H.; Onaka, R. *J. Phys. Soc. Jpn.* **1977**, *42*, 152.
- (281) Henderson, M. A. *Surf. Sci. Rep.* **2002**, *46*, 1.
- (282) Krischok, S.; Höft, O.; Günster, J.; Stultz, J.; Goodman, D. W.; Kemper, V. *Surf. Sci.* **2001**, *495*, 8.
- (283) Campbell, M. J.; Liesegang, J.; Riley, J. D.; Leckey, R. C. G.; Jenkin, J. G.; Pool, R. T. *J. Electron Spectrosc. Relat. Phenom.* **1979**, *15*, 83.
- (284) Silvestrelli, P. L.; Parrinello, M. *Phys. Rev. Lett.* **1999**, *82*, 3308.
- (285) Plummer, E. A.; Gustafsson, T. *Science* **1977**, *198*, 165.
- (286) Frank, H. S.; Thompson, P. T. *J. Chem. Phys.* **1957**, *31*, 1086.
- (287) Kropman, M. F.; Bakker, H. J. *J. Am. Chem. Soc.* **2004**, *126*, 9135.
- (288) Von Burg, K.; Delahay, P. *Chem. Phys. Lett.* **1981**, *78*, 287.
- (289) Yeh, J.-J. *Atomic Calculations of Photoionization Cross Sections and Asymmetry Parameters*; Gordon and Breach: Langhorne, PA, 1993.

- (290) Weber, R.; Winter, B.; Schmidt, P. M.; Widdra, W.; Hertel, I. V.; Dittmar, M.; Faubel, M. *J. Phys. Chem. B* **2004**, *108*, 4729.
- (291) Bernas, A.; Grand, D. *J. Phys. Chem.* **1994**, *98*, 3440.
- (292) Coe, J.; Earhart, A. D.; Cohen, M. H.; Hoffmann, G.; Sarkas, H. W.; Bowen, K. H. *J. Chem. Phys.* **1997**, *107*, 6023.
- (293) Vrbka, L.; Jungwirth, P. *Aust. J. Chem.* **2004**, *57*, 1211.
- (294) Winter, B.; Weber, R.; Schmidt, P. M.; Hertel, I. V.; Faubel, M.; Vrbka, L.; Jungwirth, P. *J. Phys. Chem. B* **2004**, *108*, 14558.
- (295) Quast, T.; Bellmann, R.; Winter, B.; Gatzke, J.; Hertel, I. V. *J. Appl. Phys.* **1998**, *83*, 1642.
- (296) Winter, B.; Weber, R.; Hertel, I. V.; Faubel, M.; Vrbka, L.; Jungwirth, P. *Chem. Phys. Lett.* **2005**, *410*, 222.
- (297) Levine, I. N. *Quantum Chemistry*, 3rd ed.; Allyn and Bacon: Boston, MA, 1983.
- (298) Jorgensen, W. L.; Salem, L. *The Organic Chemists Book of Orbitals*; Academic Press: New York, 1973.
- (299) Benson, J. M.; Novak, I.; Potts, A. W. *J. Phys. B: Atomic Mol. Opt. Phys.* **1987**, *20*, 6257.
- (300) Moore, C. E. *Atomic Energy Levels*, 1971; Vol. INSRDS-NBS 35.
- (301) Amusia, M. Y.; Cherepkov, N. A.; Chernysheva, L. V.; Manson, S. T. *Phys. Rev. A* **2000**, *61*, 020701.

CR040381P